NASA CONTRACTOR REPORT

NASA CR-482

IONOSPHERIC SIMULATOR SURVEY

by A. E. Barrington, E. D. Schultz, A. Sharma, and J. O. Sullivan

Prepared by
GCA CORPORATION
Bedford, Mass.
for Electronic Research Center

NATIONAL AERONAUTICS AND SPACE ADMINISTRATION • WASHINGTON, D. C. • MAY 1966

IONOSPHERIC SIMULATOR SURVEY

By A. E. Barrington, E. D. Schultz,
A. Sharma, and J. O. Sullivan

Prepared under Contract No. NAS 12-11 by
GCA CORPORATION
Bedford, Mass.

for Electronic Research Center

NATIONAL AERONAUTICS AND SPACE ADMINISTRATION

For sale by the Clearinghouse for Federal Scientific and Technical Information
Springfield, Virginia 22151 – Price $4.00

TABLE OF CONTENTS

LIST OF ILLUSTRATIONS

LIST OF ILLUSTRATIONS (continued)

LIST OF ILLUSTRATIONS (continued)

IONOSPHERIC SIMULATOR SURVEY

A. E. Barrington, E. D. Schultz,
A. Sharma, J. O. Sullivan

I. INTRODUCTION

The objectives accomplished during the contractual period and reported here are as follows:

(1) Conduct a survey of the state-of-the-art with respect to simulation of the D and E regions of the ionosphere, specifically identifying those parameters capable of being simulated simultaneously. It should be borne in mind that the ultimate purpose of any facility that results in totality or in part from this study will be used primarily for research on measurement techniques associated with the ionosphere.

(2) Evaluate the techniques and/or methods for ionosphere simulation, including those used in existing facilities plus any theoretically applicable approaches and select the most promising for ionospheric simulation; particular emphasis should be given to possible tradeoffs between the feasibility of achieving a given parameter of particular importance and total ambient simulation.

(3) Identify the necessary equipment to simulate the parameters selected in Item 1 and prepare an optimum performance specification for a possible Phase II requirement. Conceptual sketches to indicate the practicality of a particular approach should be included where necessary.

A survey of existing facilities showed, not unexpectedly, that no large-scale concentrated efforts are in progress at this time to simulate simultaneously the many various pertinent parameters of the ionosphere.

Specific discussions with key personnel at Lewis Research Center, Langley Research Center, Goddard Space Flight Center and Ames Research Center indicated that an ionospheric simulation facility would be of considerable interest; however, the only active programs at this time are concerned with the production of low energy space-charge-neutral

beams to simulate the density of positive ions as viewed by a satellite [1,2]*. The status of one of these programs in which GCA has recently participated is reported in some detail.

The simulation of neutral density, temperature and thermal solar flux were not considered in detail, since there exist many facilities adequately capable of simulating these parameters. However, the survey demonstrated that many other interesting ionospheric parameters, namely charged particles (positive and negative), ultraviolet and X-ray radiation, and atomic oxygen can be simulated simultaneously with various existing methods, although with certain restrictions, over the altitude range from 50 to 160 km. It also became apparent, that certain novel approaches should be investigated theoretically. The results obtained are promising and predict the feasibility of simulating the charged particle density and atomic oxygen over parts of the D-region by photoionization and photodissociation.

Consequently, it was possible to arrive at the conceptual design of an ionospheric simulation facility and to identify the equipment necessary for the simultaneous simulation of charged particle density, solar uv and X-ray flux and the production of atomic oxygen.

*Number in [ ] throughout text indicate reference numbers.

II. CHARACTERISTICS OF THE D AND E REGION

Charged Particles

Charged particle simulation presents many problems whose solution depends primarily on the altitude region being simulated. The reason for the dependence on altitude is the fact that the production of charged particles depends on the means of ionization as well as on the density of the neutral gas to be ionized. Because of the finite physical size of any laboratory simulation chamber, the effect of chamber walls becomes predominant in simulating the E region where the mean free path is long. It plays a relatively minor part in the simulation of the D region where the mean free path is much shorter. In consequence, a dual approach to the production of charged particles becomes necessary, which far from being a disadvantage, will greatly enhance the flexibility of a simulation facility.

The physical situation can best be discussed by first considering the parameters of pressure, particle density and mean free path as a function of ionospheric altitude (Table 1).

TABLE 1

IONOSPHERIC NUMBER DENSITIES

Altitude km	Pressure torr	Temperature ^{o}K	Number Density cm^{-3}	Mean Free Path cm
50	6×10^{-1}	270	2×10^{16}	10^{-2}
90	1×10^{-3}	180	6×10^{13}	6
160	3×10^{-6}	1000	2×10^{10}	2×10^{3}

In the D region, for example, the mean free path varies from 0.1 mm to 6 cm and the effects of chamber walls can be minimized for even a moderately sized laboratory facility. In the E region, the mean free path can be as large as 20 m, prohibitively large for simulation. However, the density of charged particles increases as we move from the

D region to the E region. In the D region, an average density of 10^4 particles/cm^3 can be assumed from actual experimental data (Figure 1). For the E region (Figure 2), an approximate positive ion concentration can be obtained by assuming it to be equal to the experimentally measured electron density. As an additional basis for comparison, Figures 3(a) and 3(b) show the ion density profile for individual species at higher altitudes [3].

Because of the large differences of neutral density, the methods of producing ion densities of the order of 10^5/cc, which are essentially independent of the ambient density, must necessarily be different. Let us first consider the problem in the D region. According to current theory [4], the primary formation mechanism for portions of this region is the upper ionization of NO by solar H Lyman-α (1215.6Å) whereas at lower altitudes ionization of all constituents is produced by cosmic radiation and by solar X-rays. Although the importance of the latter processes is still subject to debate for quiet conditions, the role played by X-rays in disturbed solar flare conditions has been established beyond question [5,6]. Accordingly, solar flux simulation with respect to D-region phenomenology would necessarily include X-ray and H Lyman-α spectral regions. Theoretical estimates of the transmission characteristics of these radiations in the terrestrial atmosphere are shown in Figure 4.

Owing to its low altitude, the D region is characterized by a relatively large density so that the attachment rate of electrons especially to O_2 is appreciable. Indeed, this process precludes the buildup of relatively high electron densities which cause severe radio frequency absorption in the region during disturbed solar flare conditions.

In general, the complex interaction between solar radiation and the ambient constituents of the region as well as the various dark reactions (including electron-generating and electron-depression processes and other chemical interactions) produces the classical electron density profiles which are characterized by sharp altitude gradients and significant number density variations for night-time, day-time and disturbed conditions as illustrated in Figure 5. Caution should be exercised in the use of the data presented in this figure since it has been included to indicate the overall steady-state, static behavior in the D region. In reality, this region exhibits a more irregular dynamic behavior than higher ionospheric regions. Accordingly, D-region electron density profile simulation should reflect the dynamic range illustrated in Figure 6 where actual measured profiles are presented for the D and E regions. The caption below the figure defines the

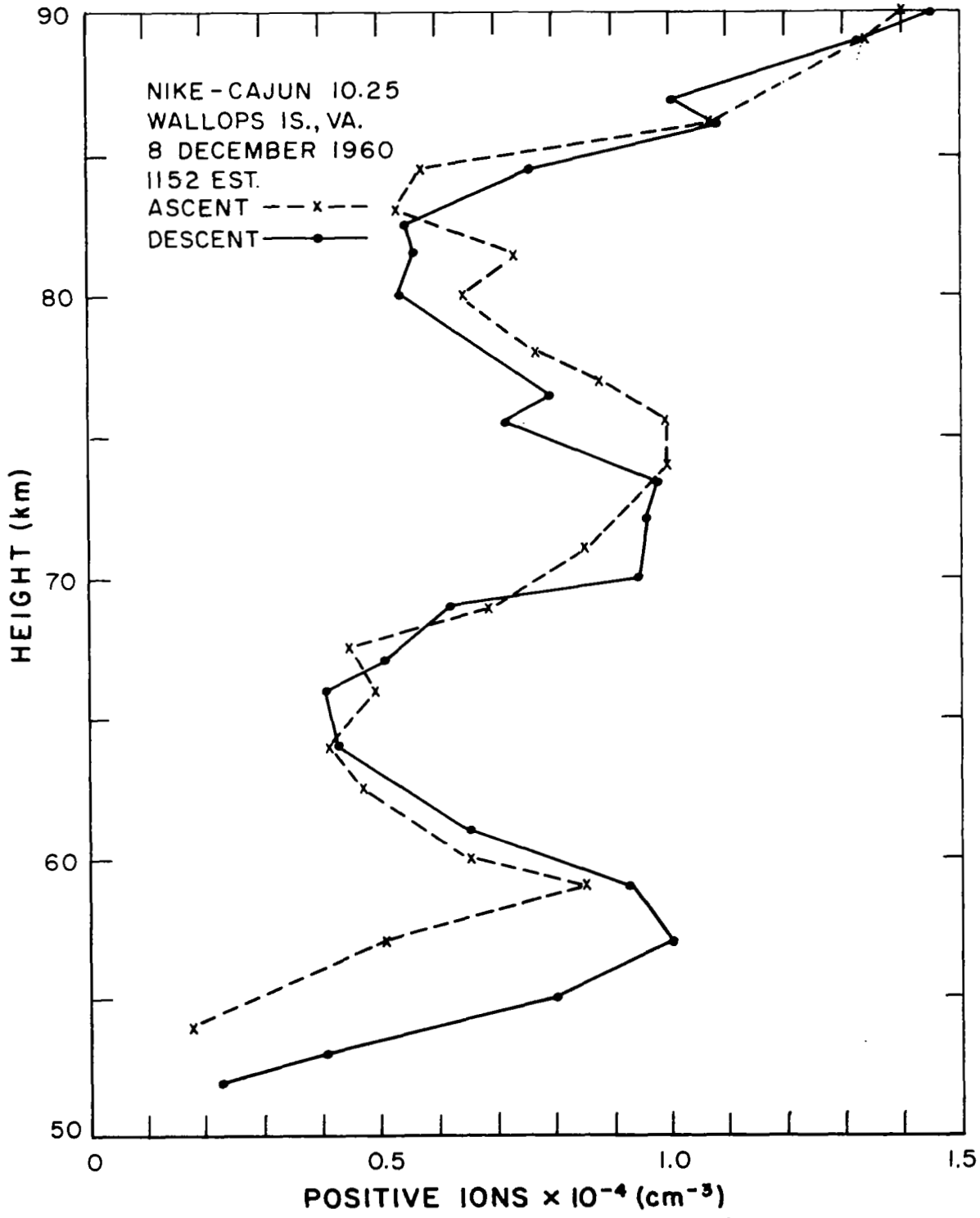

Figure 1. Positive ion density versus height.

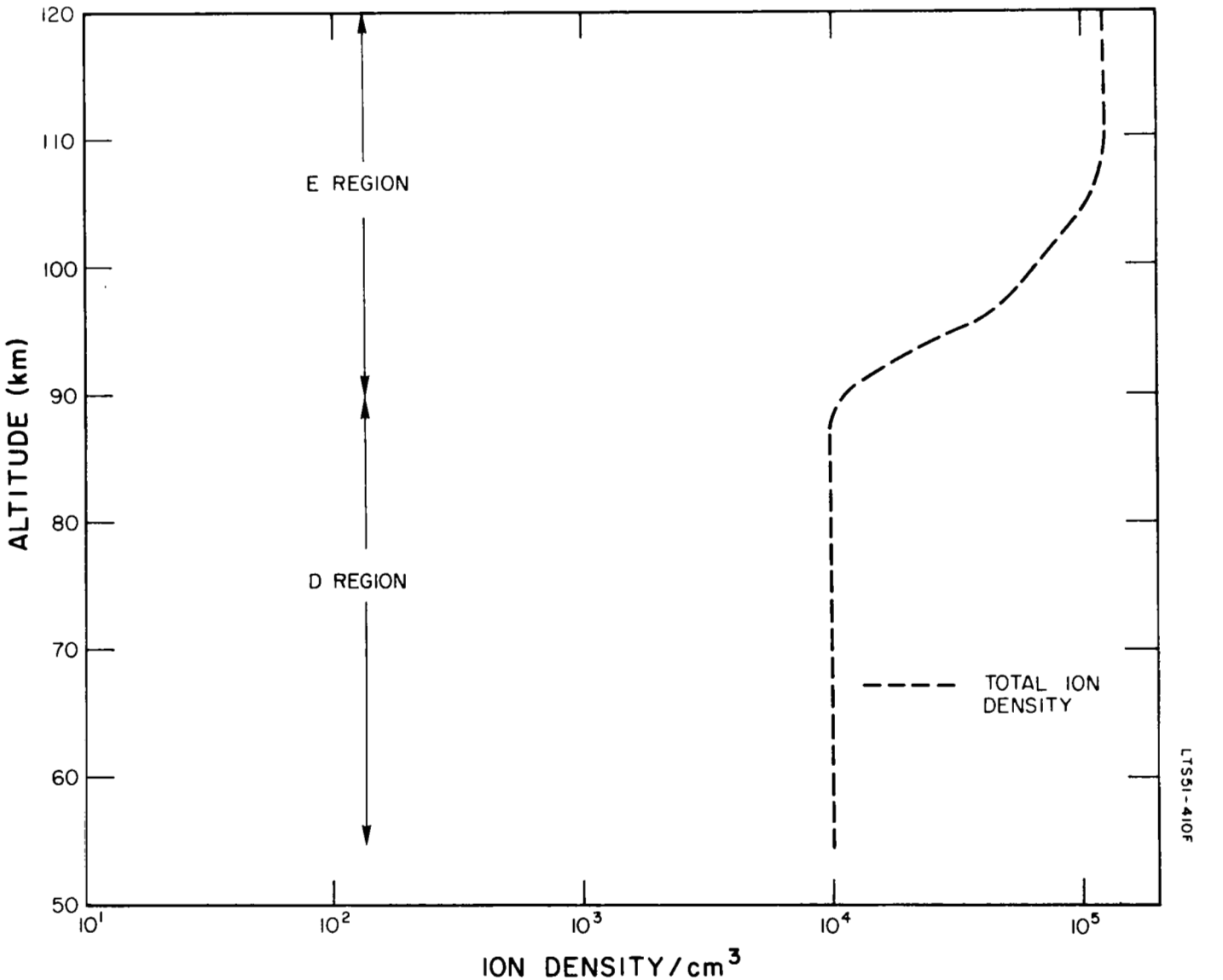

Figure 2. Ion density as a function of altitude.

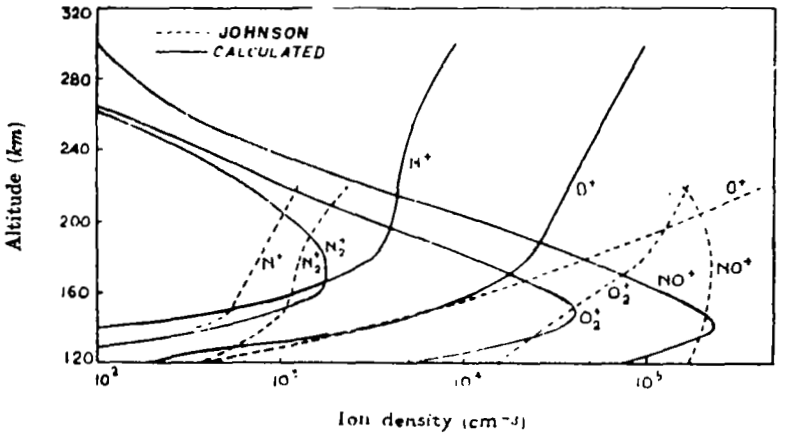

(a)

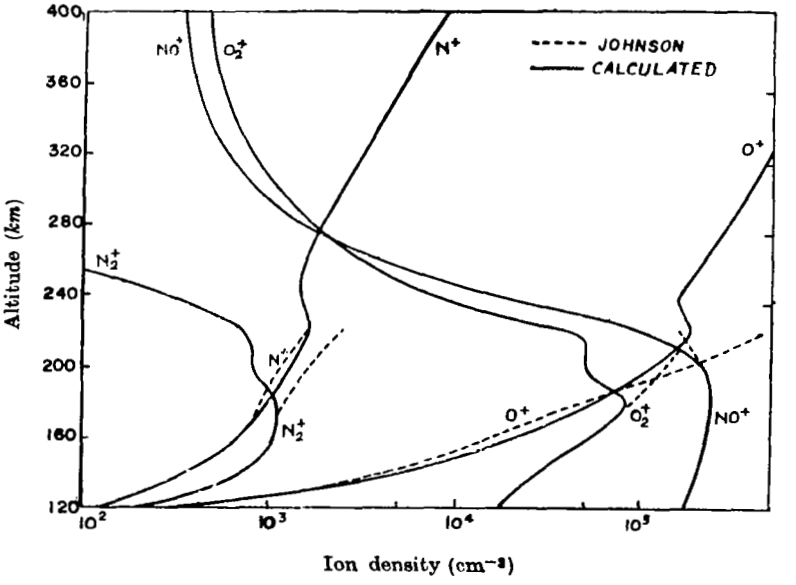

(b)

Figure 3. Ion Densities vs Altitude.[3]

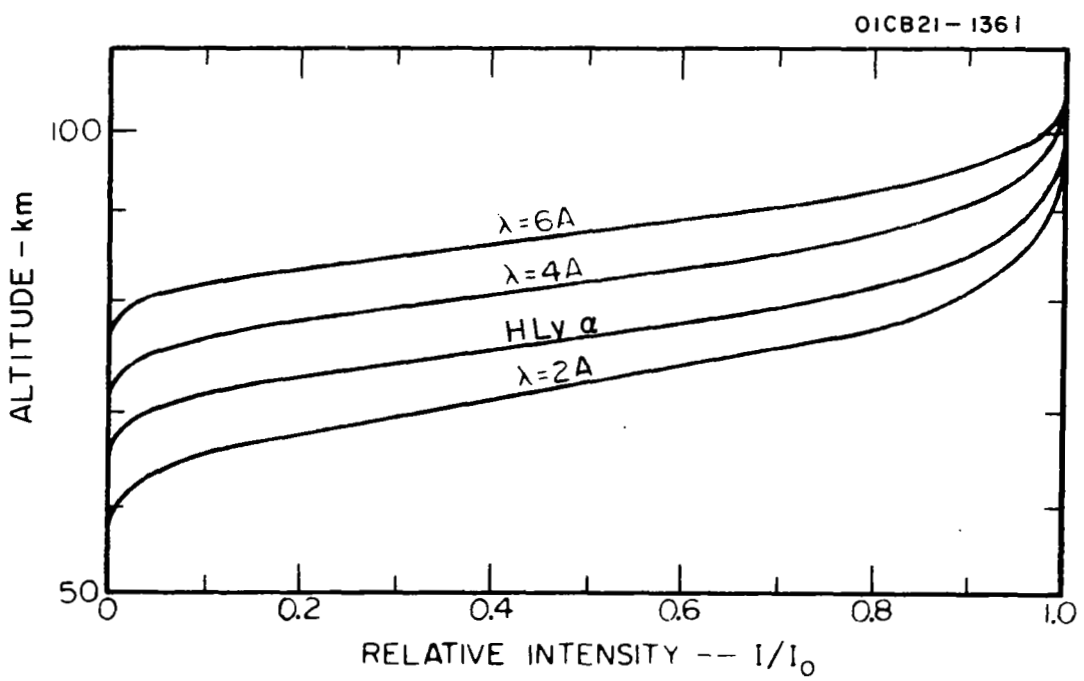

Figure 4. Transmission of x-rays through the atmosphere.

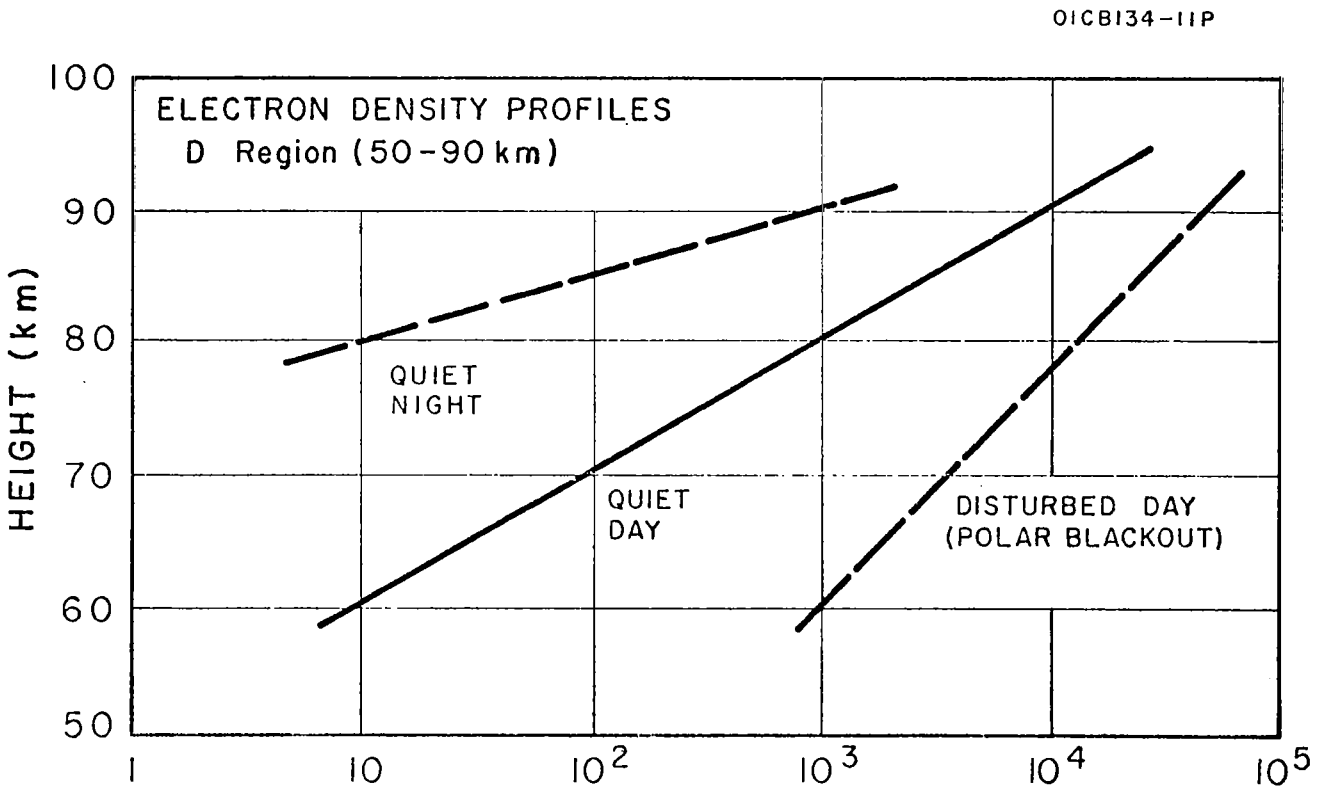

Figure 5. Electron density profiles, D-Region.

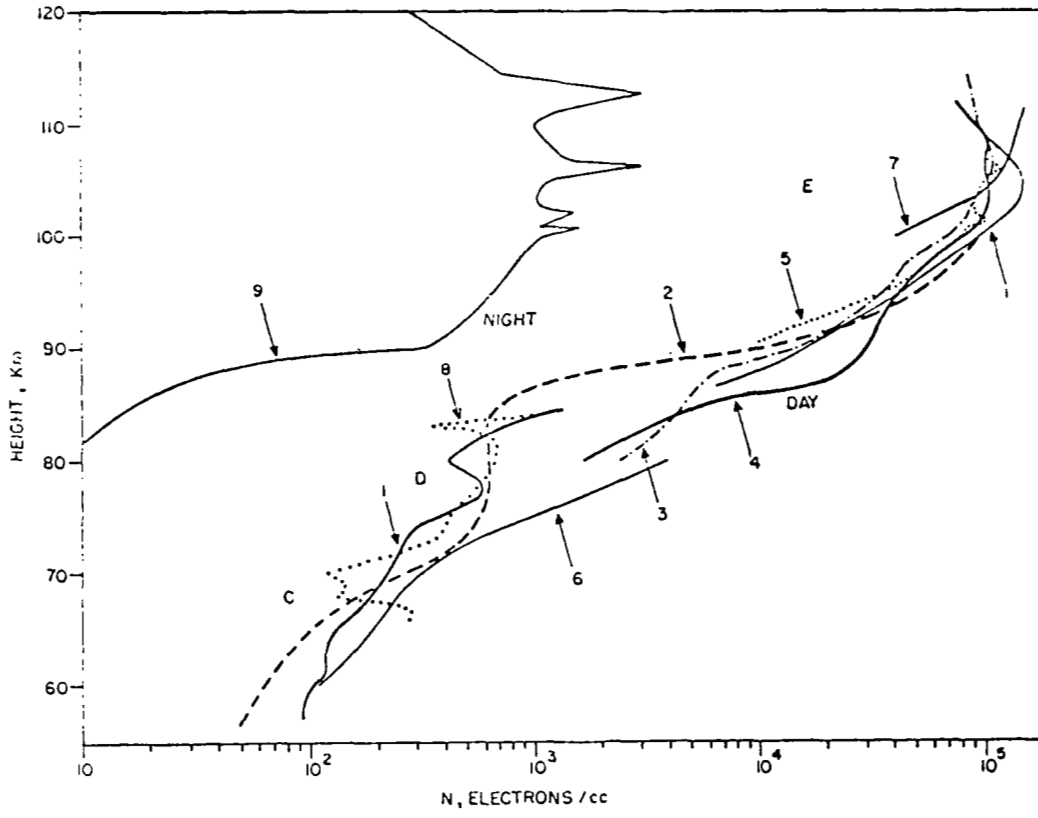

Figure 6. Electron Density height profiles for the D and E regions.

1: Belrose (1961), 1030-1130 LST, May 1, Ottawa, Canada. 2: theoretical, Aikin et al. (1963), middle latitude, midday. 3: Yonezawa (1961), 1532 LST, September 22, Michikawa, Japan. 4: Adey and Heikkila (1960), 1237 LST, September 17, 1959, Churchill, Canada. 5: Friedman (1959), 1730 LST, June 26, 1954, USSR middle latitude. 6: Barrington et al. (1960), 1000-1400 LST, March-April, Kjeller, Norway. 7: Robinson (1957), midday, March 27, Cambridge, England. 8: Aikin et al. (1963), 1430 LST, March 8, Wallops Island, U.S.A. 9: Smith (1961), 0435 LST, October 27, Wallops Island, U.S.A.

sources of information. It can be seen that only night-time D region measurements of the D region were performed by GCA Corporation [7] under a NASA contract and these show a strikingly decreased profile activity level (curve 9). One may conclude that accurate D-region simulation should incorporate the diurnal and activity range of electron densities presented in the figure.

As noted previously, the highly irregular behavior of the D region must be considered in greater detail in order to provide effective simulation of this facet of the dynamics of the region. There are several and varied factors which have been viewed as probable sources of considerable enhancement or depletion of electron density. For example, the electron density profiles of Figure 6 which are typical of day and night-time conditions exhibit a relatively wide diurnal fluctuation. It may be inferred, therefore, that the achievement of these day-time and/or night-time steady-state values requires transient periods during sunrise and sunset. The salient features associated with these transition periods are illustrated graphically in Figure 7. As the shadow of the ozone layer moves to either permit or prevent near uv radiation (2000 to 3000Å) from illuminating the D region, rapid transitions in D-layer activity and radio-wave absorption can be expected due to negative ion formation. Since it can be shown that the dominant negative ion during the sunrise-sunset period cannot be O_2^- (or any other negative ion which can be photodetached by visible light), likely candidates are either NO_2^- or O_3^- while more remote possibilities include H^- and OH^-. This screening effect has been verified recently by a GCA Corporation rocket probe experiment conducted by Smith, et al.[8], during the IQSY effort.

Another factor which sensitively affects the lower D region is solar activity as illustrated in Table 2 which presents the pertinent ionization rate coefficients at 2, 4, and 6Å. It can be seen that these rates show a factor of 10^5 enhancement during strong solar flares compared to the completely quiet sun condition. Clearly, this ionization rate increase is directly reflected in the steady-state electron density profiles corresponding to the specified solar conditions. This rate increase has been verified during severe ionospheric disturbances (SID) where strong radio-wave absorption is observed in the lower D region. It may be noted, however, that the corresponding solar H Lyman-α radiation has been observed to remain relatively constant for the various solar conditions [9], so that upper D-region variations in electron density activity levels are not quite so pronounced.

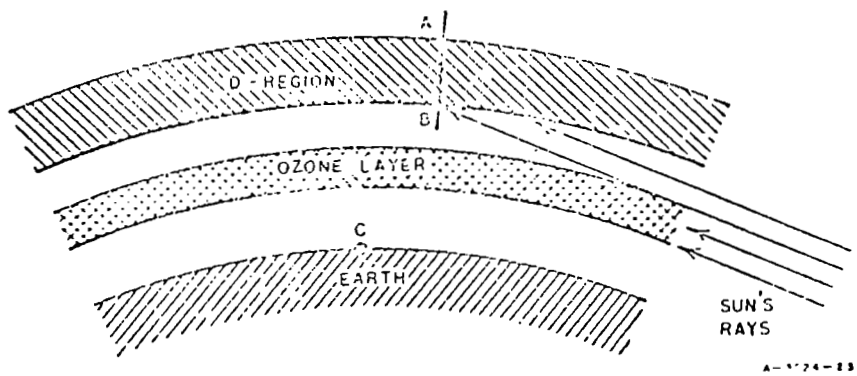

Figure 7. Sunrise-sunset effect.

At sunset the near UV solar radiation which would otherwise illuminate that part of the D-region lying to the left of line AB is absorbed by the ozone layer when the sun drops below the horizon with respect to an observer at C. Coincident with the absorption of this radiation is the rapid decrease in electron density (probably due to electron attachment) in the region to the left of line AB. The opposite effect (rapid detachment of electrons when the sun's rays pass above the ozone layer) occurs at sunrise.

TABLE 2

IONIZATION RATE COEFFICIENTS (Sec^{-1}) AT 2, 4, AND 6Å

Solar Conditions	2Å	4Å	6Å
Completely quiet	1.6×10^{-19}	9.8×10^{-18}	2.8×10^{-16}
Quiet	1.6×10^{-18}	9.8×10^{-17}	2.8×10^{-15}
Lightly disturbed	1.6×10^{-17}	9.8×10^{-16}	2.8×10^{-14}
Disturbed	1.6×10^{-16}	9.8×10^{-15}	2.8×10^{-13}
Special events	1.6×10^{-15}	9.8×10^{-14}	2.8×10^{-12}
Strong flares	1.6×10^{-14}	9.8×10^{-13}	2.8×10^{-11}

Still other D-region dynamic variations have been observed at high latitudes due to polar-cap absorption (PCA) effects and the influence of aurora. In the former, the transient effects have been observed to extend over several days whereas the extent of auroral effects persists for a matter of hours. Concerning auroral phenomena (Type II), significant correlation between this activity and the D-region phenomena was recently obtained during a GCA Corporation rocket probe experiment by Accardo, et al. [10]. This multiple instrumentation experiment performed simultaneous measurements of X-ray, electron, and solar H Lyman-α fluxes as well as the ambient electron density as functions of altitude. Performing laboratory simulation of these transient phenomena appears to be difficult but should necessarily be included in the proposed feasibility study.

Simulation of the D region requires modeling the physical parameters of the predominantly neutral gas. Between 50 and 90 km the pressure varies between 6×10^{-1} to 1.2×10^{-3} torr, the temperature range lies between 180 and 270°K, and the total number density varies from 6×10^{13} to 2×10^{16} particles cm^{-3}. The bulk of the atmosphere consists of molecular nitrogen and oxygen (except in the high D region where considerable atomic oxygen exists), and small amounts of rare gases. Some specific minor constituents which are known to exist in the lower portion of the region include CO_2, CO, CH_4, N_2O, H_2, etc., although their actual

abundances are not accurately known. Atomic oxygen and ozone, which are products of solar photolysis of molecular oxygen, have also been recognized as important neutral ionospheric constituents. Figure 8 shows the abundances of several important species based on data presented by Bates and Nicolet [11]. Several recent theories have associated specific D-region phenomena with OH, H_2O, NO, and various trace elements such as sodium so that these should be considered in the laboratory simulation feasibility study. Other species which may significantly contribute to D-region phenomenology and thereby merit feasibility study consideration include micrometeorites and their vaporization products.

Experimental information regarding the existence of positive ion species in the D region is limited to the measurements of Narcissi, et al. [12], who reported positive ions of H_2O^+ and NO^+ in the altitude range 64 to 82 km and Mg^+, Na^+, and NO^+ somewhat higher between 82 to 112 km. There is little theoretical basis for doubting that the cosmic and X-ray flux contributions form O_2^+ and N_2^+ ions in the lower D region. To date, unambiguous experimental observation of negative ions in the D region has not been performed although the existence of specific negative ions such as O_2^-, O^-, NO_2^-, O_3^-, H^- and OH^- have been postulated from theoretical considerations. Notwithstanding the questions of sources and distributions of these positively and negatively charged constituents in the D region, suitable simulation of the ambient requires their consideration.

The E region which is usually placed between 90 and 160 km is characterized by a marked electron density peak between about 100 and 130 km. Superposed on this quasi-static structure there occurs sporadic E which is both highly irregular and relatively unpredictable and therefore presents extreme difficulties in simulation.

The normal E region is probably formed by ionization of the ambient constituents by the solar X-ray flux between 40 and 100Å [13], although recent results of Watanabe and Hinteregger [14], indicate that the primary ionization source may be radiation in the 912 to 1030Å spectral region. During the solar eclipse of 20 July 1963, simultaneous rocket-probe measurements of electron density profiles and solar X-ray flux between 44 and 60Å were performed by GCA Corporation in the E region [15]. The interpretation of these results strongly supports the X-ray hypotheses since the observed electron density variation with percent solar obscuration could only be explained in this manner. Accordingly, solar flux simulation in the E region requires consideration of 40 to 100Å and 912 to 1030Å spectral regions. In the latter region, actual

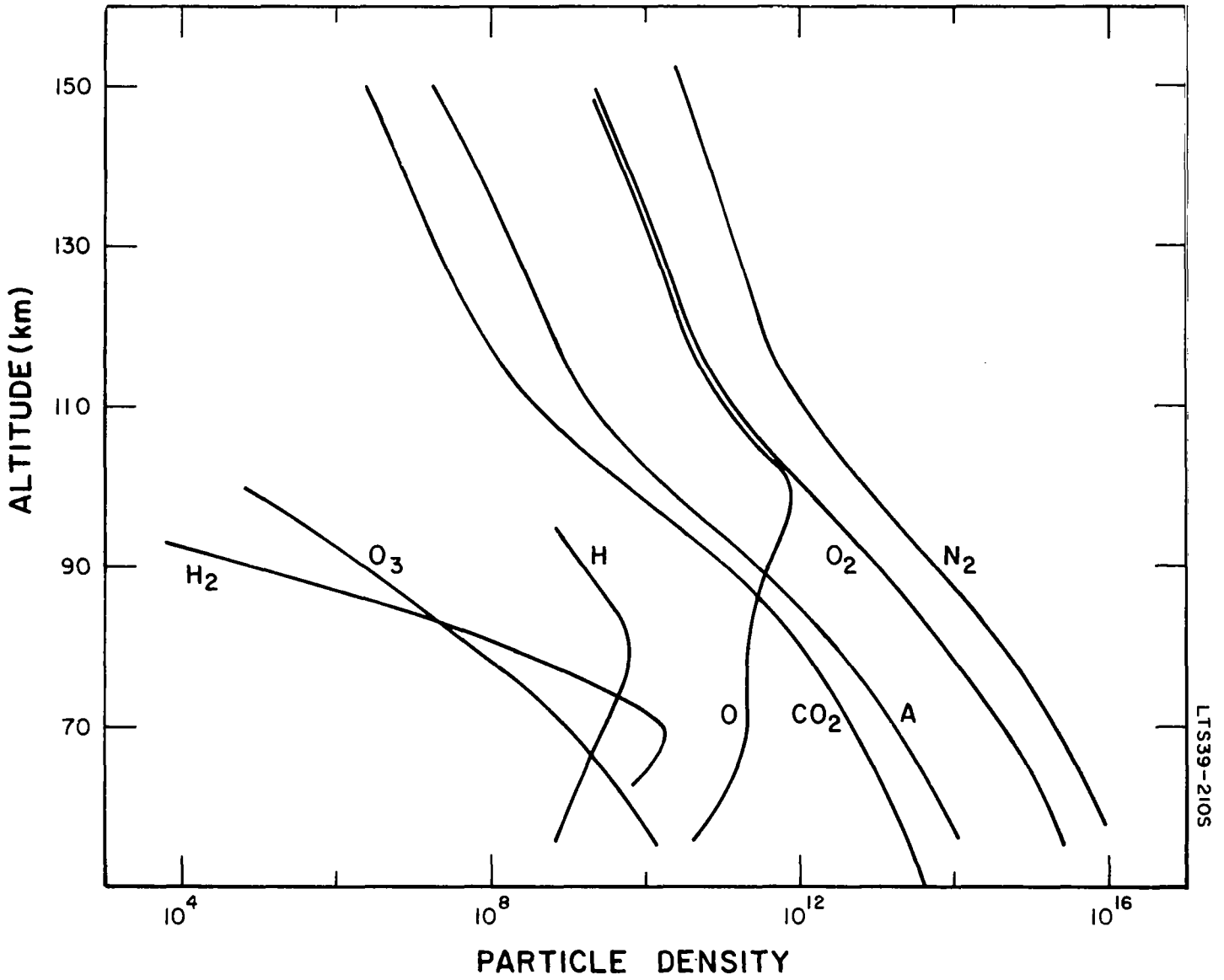

Figure 8. Number density distribution for several atmospheric constituents (after Bates and Nicolet).

duplication of solar emission lines has been accomplished in the GCA Corporation Ultraviolet Laboratory under a study concerned with obtaining the total and photoionization cross sections for atmospheric gases [16].

The major atmospheric constituents in this region are molecular nitrogen, molecular oxygen and atomic oxygen; the latter due to the solar photolysis of O_2 as shown in Figure 8. This constituency results in the generation of O_2^+, O^+ and N_2^+ ions as shown in Figure 9 which indicates the appropriate photoionization rate for these species as a function of altitude. However, mass spectrometric measurements have shown that the dominant ion in this region [17] is NO^+ as indicated in Figure 9(b) and Table 3. Accordingly, the O^+ and N_2^+ ions in this region must undergo further exchange reactions such as:

$$O^+ + N_2 \rightarrow NO^+ + N$$

and/or

$$N_2^+ + O \rightarrow NO^+ + N$$

to produce the observed predominant NO^+ fraction.

Concerning E-region electron number density, (N_e) both theory and observation suggest that its variation may be represented by the following partial differential equation:

$$\frac{\partial N_e}{\partial t} = q - \alpha_{eff} N_e^2$$

where α_{eff} is the effective recombination coefficient and q is the rate of electron generation. The loss of electrons typically proceeds via dissociative recombinations:

$$NO^+ + e \rightarrow N + O,$$

$$N_2^+ + e \rightarrow N + N \quad \text{and}$$

$$O_2^+ + e \rightarrow O + O.$$

TABLE 3

RELATIVE CONCENTRATIONS OF POSITIVE ION SPECIES

Rocket Flight	Altitude (km)	Fraction of Total Positive Ions which are: N_2^+	O_2^+	NO^+	O^+
NN 3.17 F[1]	150	< 0.03	0.4	0.5	0.1
2321 CST	120	< 0.03	0.2	0.8	< 0.03
20 Nov 56	100	< 0.03	0	1.0	~ 0
NN 3.18 F[1]	150	< 0.03	0.1	0.8	0.1
2002 CST	120	< 0.03	0.1	0.9	< 0.03
21 Feb 58	100	< 0.03	0.1	0.9	~ 0
NN 3.19 F[1]	150	< 0.03	0.3	0.6	0.1
1207 CST	120	< 0.03	0.3	0.7	< 0.03
23 Mar 58	100	< 0.03	0.4	0.6	~ 0
NASA 4.09[2]	150	~ 0.01	0.3	0.6	0.1
1047 EST	120	~ 0.01	0.1	0.9	< 0.05
20 Apr 60	100	~ 0.01	0.1	0.9	~ 0
NASA 4.14[2]	150	~ 0.01	0.4	0.4	0.2
1141 EST	120	~ 0.01	0.2	0.8	< 0.05
15 Nov 60	100	~ 0.01	~ 0	1.0	~ 0
USSR[3]	150	...	0.1	...	...
h = -6°e	120	...	...	...	...
9 Sep 57	100	...	...	...	...
USSR[3]	150	...	0.2	0.6	0.2
h = 36°m	120	...	0.3	0.7	~ 0
2 Aug 58	100	...	0.2	0.8	~ 0
USSR[3]	150	...	0.4	0.6	0.05
h = 0°m	120	...	0.2	0.8	~ 0
13 Aug 58	100	...	...	...	...
USSR[3]	150	...	0.3	0.7	0.05
h = 0°m	120	...	0.1	0.9	~ 0
22 Jul 59	100	...	...	...	...
USSR[3]	150	...	0.4	0.5	0.1
h = 15°m	120	...	0.3	0.7	~ 0
15 Jun 60	100	...	0.1	0.9	~ 0

(1) Johnson, Meadows and Holmes (1958); Meadows and Townsend (1960).
(2) Taylor and Brinton (1961).
(3) Istomin and Pokhunov (1962); h indicates altitude of sun above horizon, e and m denote evening and morning, respectively.

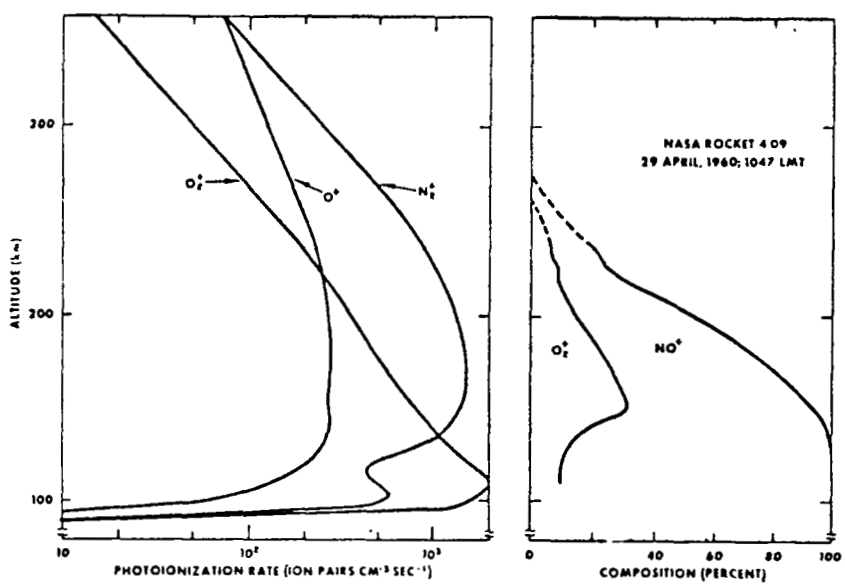

a. b.

Figure 9. Comparison of the production rate and the actual abundance of ions in the lower ionosphere.

Laboratory measurements and ionospheric observations based on the above loss processes suggest that α_{eff} is of the order of 10^{-7} - 10^{-8} cm^3 sec^{-1} in this region. Experimentally, the measured steady-state electron densities in the E-layer range from about 10^5 to 1.5 x 10^5 electrons cm^{-3} depending on such gross indicators of solar activity as the 11-year sun-spot cycle. Accordingly, suitable E-region simulation should consider the problems associated with the generation of a slightly ionized plasma at the indicated pressure level in a chamber of appropriate dimensions to accommodate the prescribed electron rate and simultaneously minimize the effects of wall collisions. The E region may be characterized uniquely by specific features not found in the other ionospheric regions. For example, most micrometeoric debris is vaporized and deposited at E-region altitudes which probably results in atmospheric contamination by minor debris constituents and by photoionization of the residence of such positive species as Mg^+, Ca^+, Na^+, etc. In fact, the continuous addition of micrometeoric debris has been associated with the maintenance and presence of significant irregularities of the night-time E region and has also been associated with sporadic E. In the lower E region observations have confirmed the existence and persistence of strong wind shear and turbulence as indicated by sodium vapor experiments [18]. On a theoretical basis this phenomenon has been associated with the formation of sporadic E and experimentally checked by GCA Corporation rocket probes with the multiple capability of simultaneously measuring both the electron density and wind profiles over the altitude region of interest. In contrast to lower altitudes, the E region is classically considered as the beginning of the "low pressure regime" in the upper atmosphere. As a consequence, above this region the formation of significant amounts of negative ions can be precluded so that E-region simulation need not consider this aspect of the problem. An additional consequence of the low pressure is that diffusive equilibrium prevails above about 100 km so that composition simulation must consider this factor. Finally, the low collision probability at these low pressures enables electron temperature to depart from the ion and neutral species temperature; however, this effect becomes significant only in the upper E-region altitudes [19].

Thus, it appears that the state of knowledge concerning the E region is more complete than that of its lower counterpart, at least with respect to parameters necessary and amenable to laboratory simulation. On the other hand, preliminary considerations indicate that practical E-region simulation is extremely complex due to the characteristic low pressures associated with mean free paths which are difficult, if not impossible, to accommodate in present-day vacuum chambers.

Solar Ultraviolet and X-Ray Spectrum

The radiation in the ultraviolet region is only a small fraction of the total emitted by the sun. However, the ultraviolet radiation is of primary aeronomic importance in the discussion of the simulation of the D and E regions since most atmospheric gases absorb strongly at wavelengths below 3000Å, and the absorption processes significantly affect the chemical, thermal, and electrical properties of the upper atmosphere. As a result of the cutoff at about 3000Å of ground-based spectral observations, most of our knowledge of solar ultraviolet radiation has been obtained only during the past decade from rockets and satellites.

Radiation in the 2000 to 2900Å region is absorbed in the Hartley bands and continuum of ozone between 25 and 75 km. Molecular oxygen above 100 km is the primary absorber of radiation in the 1300 to 2000Å region. Between 1000 and 1300Å, some radiation penetrates to lower altitudes through narrow windows in the O_2. An important feature in respect to ionospheric formation is the penetration to 75 km at one such window of Hydrogen Lyman-α (1216Å). The intensity of Lyman-α at the top of the atmosphere is about 6 ergs cm^{-2} sec^{-1} $Å^{-1}$, or nearly one-half the total below 1300Å. Several solar emission lines below 1000Å are cut off by molecular nitrogen above 120 km. Photoionization continua of O_2, O, N_2, and N absorb radiation at wavelengths below 800Å at about 160 km. At wavelengths shorter than 400Å, the depth of penetration into the atmosphere increases. Soft X-rays at wavelengths below 100Å are predominantly responsible for the ionospheric E-region electron density. Hard X-rays below 10Å wavelength and radiation at wavelengths 1000 to 1300Å contribute to the formation of the D region.

In Figure 10, the altitude of unit optical depth, i.e. when the solar radiation becomes equal to 1/e of its value at the top of the atmosphere, is plotted for the ultraviolet spectral region. In Figures 11 through 13, atmospheric transmission curves are shown for several important emission lines and wavelengths. The ultraviolet spectrum has been observed in detail to about 100Å, and the main outline is known to about 6Å. Beyond this limit our knowledge is sketchy; however, during large solar flares, the detectable spectrum has been extended to 1Å. The visible and near ultraviolet spectral regions contain a continuous emission background on which are superimposed tens of thousands of Fraunhofer absorption lines of various intensities and with increasing density toward shorter wavelengths. The continuum emanates from the base of the photosphere and corresponds approximately

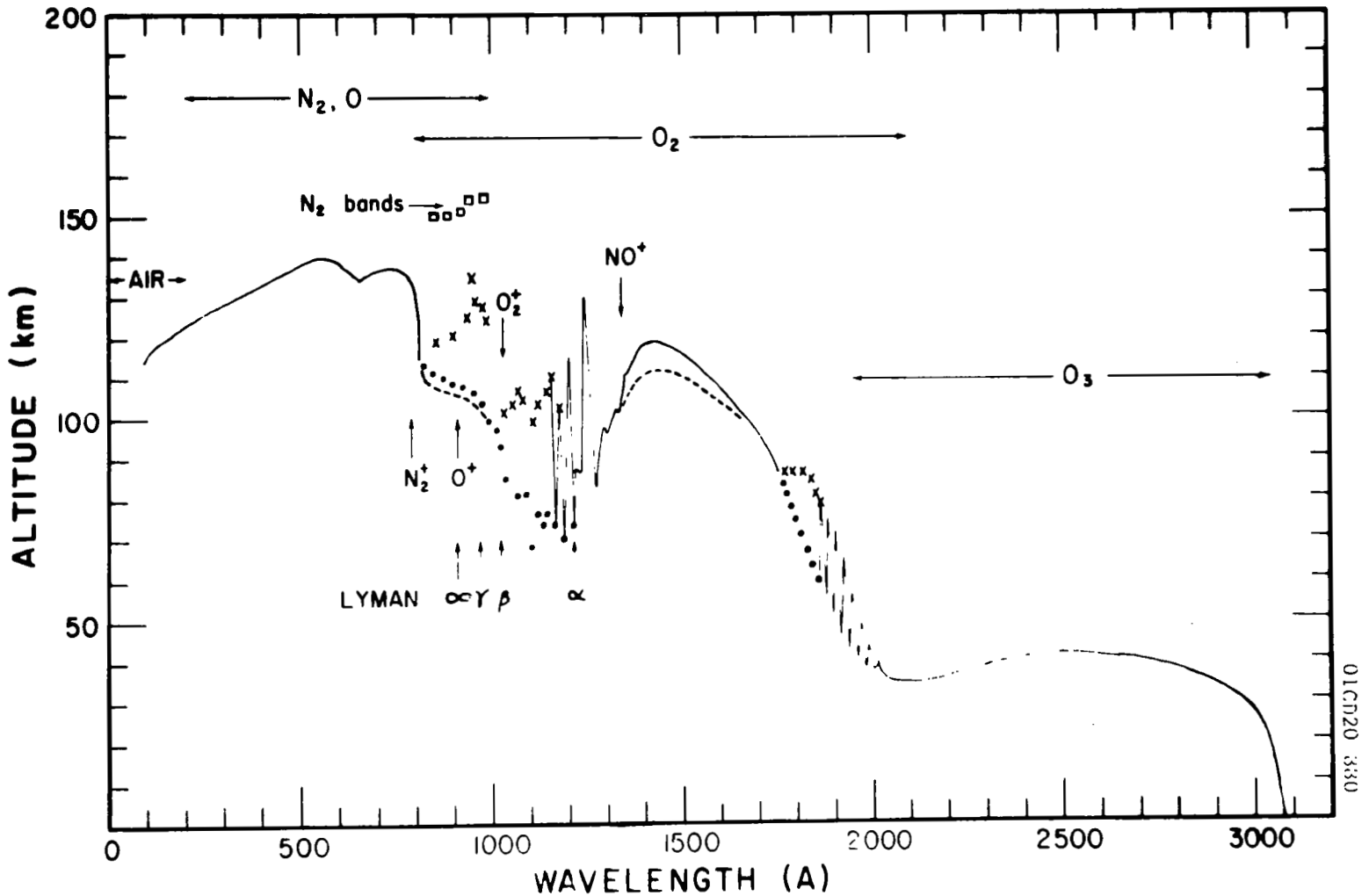

Figure 10. Penetration of solar ultraviolet radiation.[20]

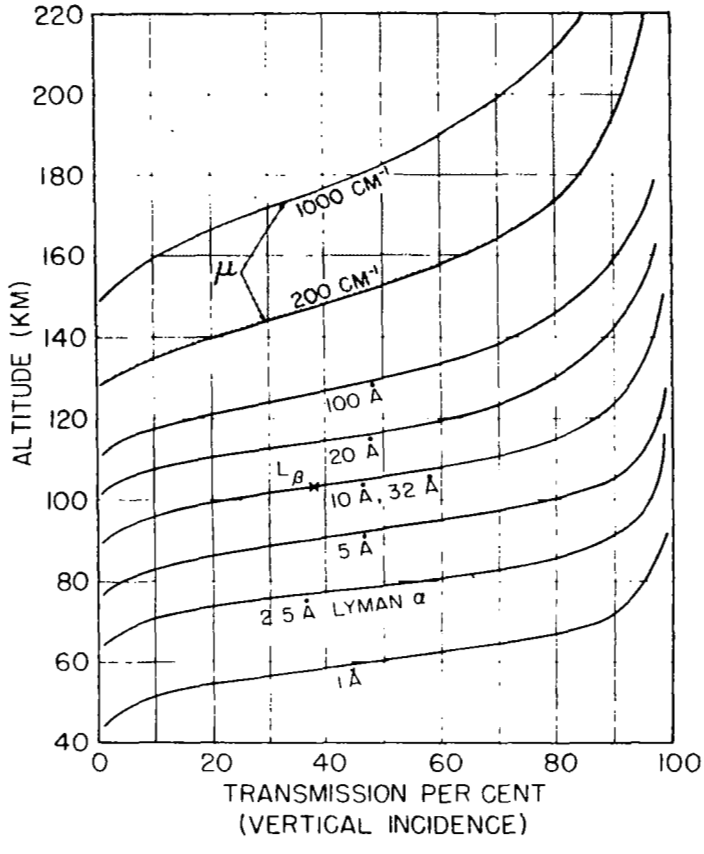

Figure 11. Penetration of the atmosphere by solar X-rays and ultraviolet radiation.[20]

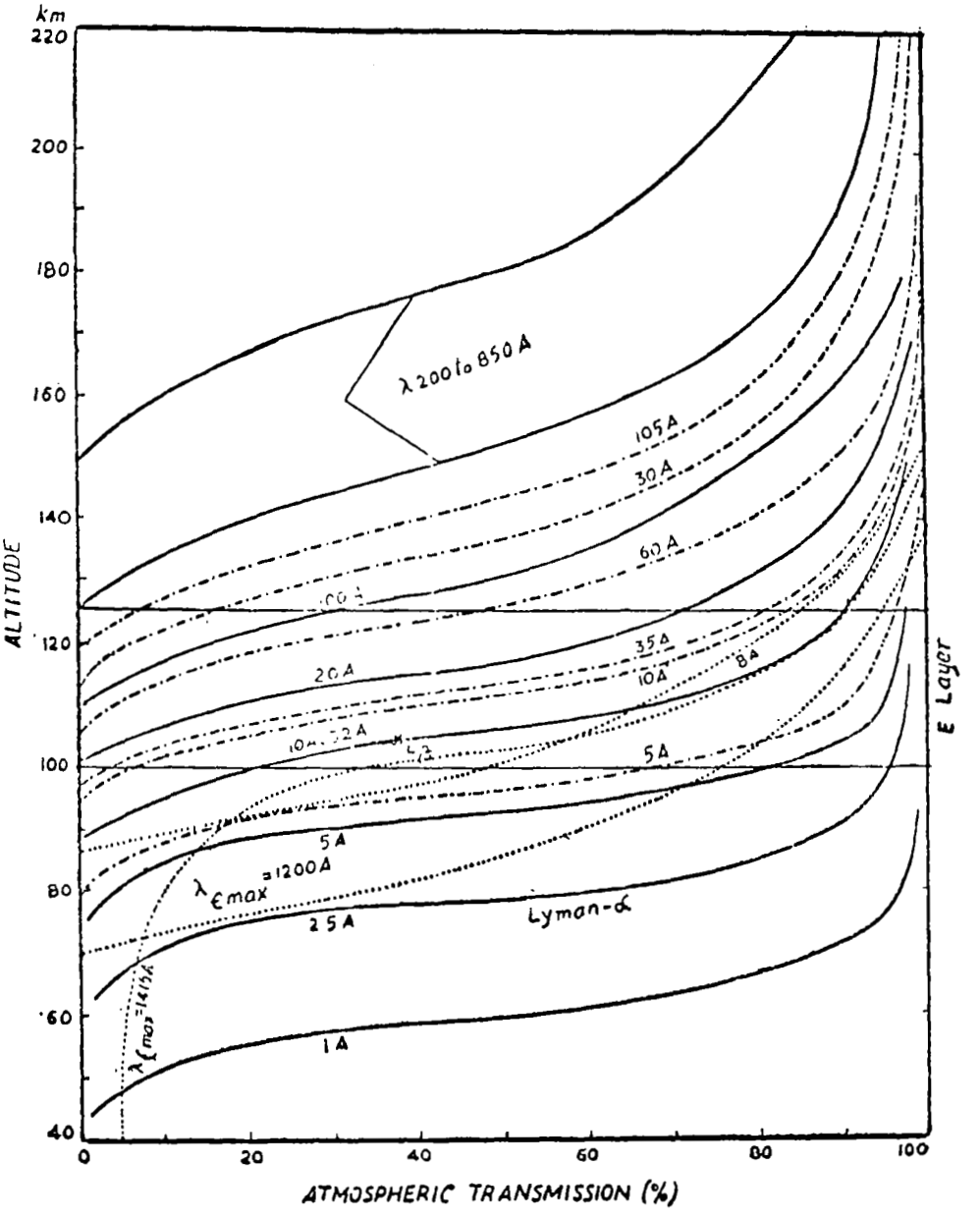

Figure 12. Atmospheric transmission for different wavelengths in the X-ray and ultraviolet regions.[21]

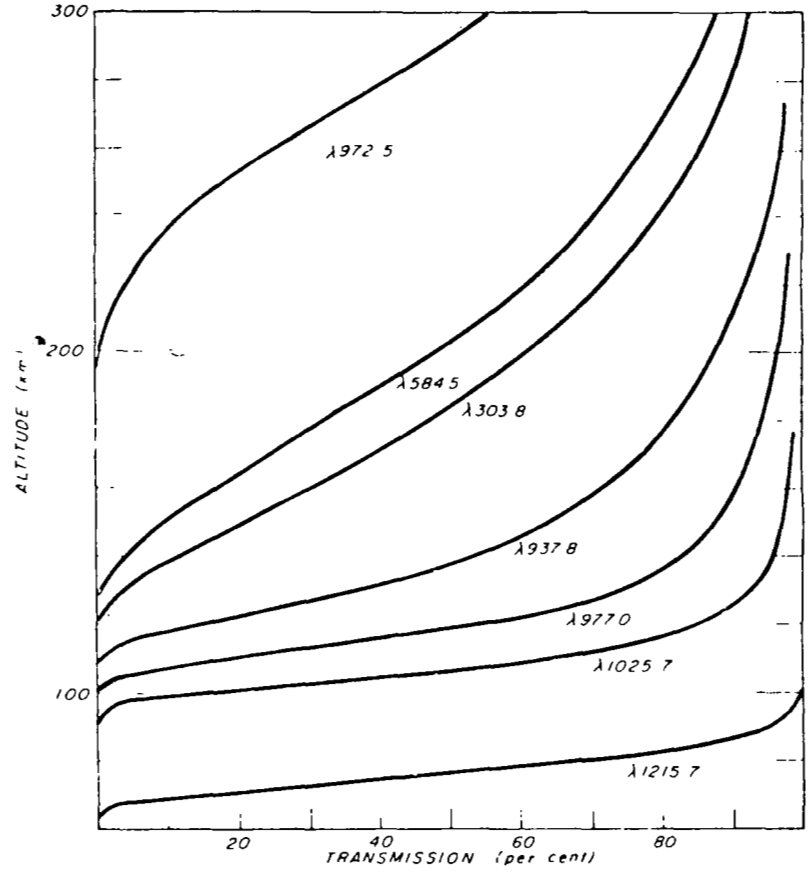

Figure 13. Penetration of the atmosphere by solar ultraviolet radiation.[22]

to a blackbody at 6000°K. Toward the far ultraviolet, the emission occurs higher in the photosphere. At these wavelengths the continuum falls abruptly, and at around 2100Å, the intensity of the continuum becomes about equal to the core intensities of the Fraunhofer lines, although these lines are still distinguishable to 1530Å. Radiation at 1300 to 1500Å originates at the top of the photosphere and corresponds roughly to a blackbody at 4700°K, the minimum temperature in the solar atmosphere. Starting at about 1850Å, chromospheric emission lines are observable in the spectrum, and into the extreme ultraviolet region they become predominant above the weakening continuum. Below 1000Å, the emission lines occur predominantly in the corona. The spectrum 10 to 1000Å resembles approximately a blackbody of 500,000°K. The most predominant of the chromospheric and coronal emission lines are the Lyman series and resonance lines of neutral and singly ionized helium. Most emission lines above 800Å have been identified while only about one-half of those below 800Å have been identified with certainty.

The intensity of the solar visible and ultraviolet emission varies little throughout the solar cycle. However, the X-ray emission below 100Å is highly variable and is subject to both short-term and long-term effects. X-rays at wavelengths 44 to 60Å exhibit an increase by a factor of seven from sunspot minimum to maximum. There is an increase by a factor of nearly fifty for the 8 to 20Å region and by a factor of several hundred for 2 to 8Å. Figure 14 shows the X-ray energy flux for various solar conditions. The data were calculated from X-ray photometer responses assuming a simplified form of the unknown solar emission curve.

In 1962, GCA [24] published a presentation of the solar ultraviolet flux from 50 to 3000Å. A current literature search has disclosed that the material is still valid. Consequently, this data on continuum and emission line photon fluxes, appearing in Tables 4 and 5 and Figures 15 through 19 will be used in the present study. The compilation was based essentially on the work of Watanabe [25], Hinteregger [26], Tousey [27], and Johnson [28].

Between 50 and 1850Å, the major emission lines were distinguished from the continuum and are presented separately. The continuum and weak lines are lumped together. The emission line data presented by Watanabe and by Tousey were modified to reflect the most recent measurements by Hinteregger. Beyond 1850Å, emission lines could not be resolved from the continuum. Below 283Å, the absence of emission lines merely reflects the lack of experimental data.

In the near ultraviolet, the data published by Johnson and by Tousey agree down to 2400Å; but at shorter wavelengths, they differ

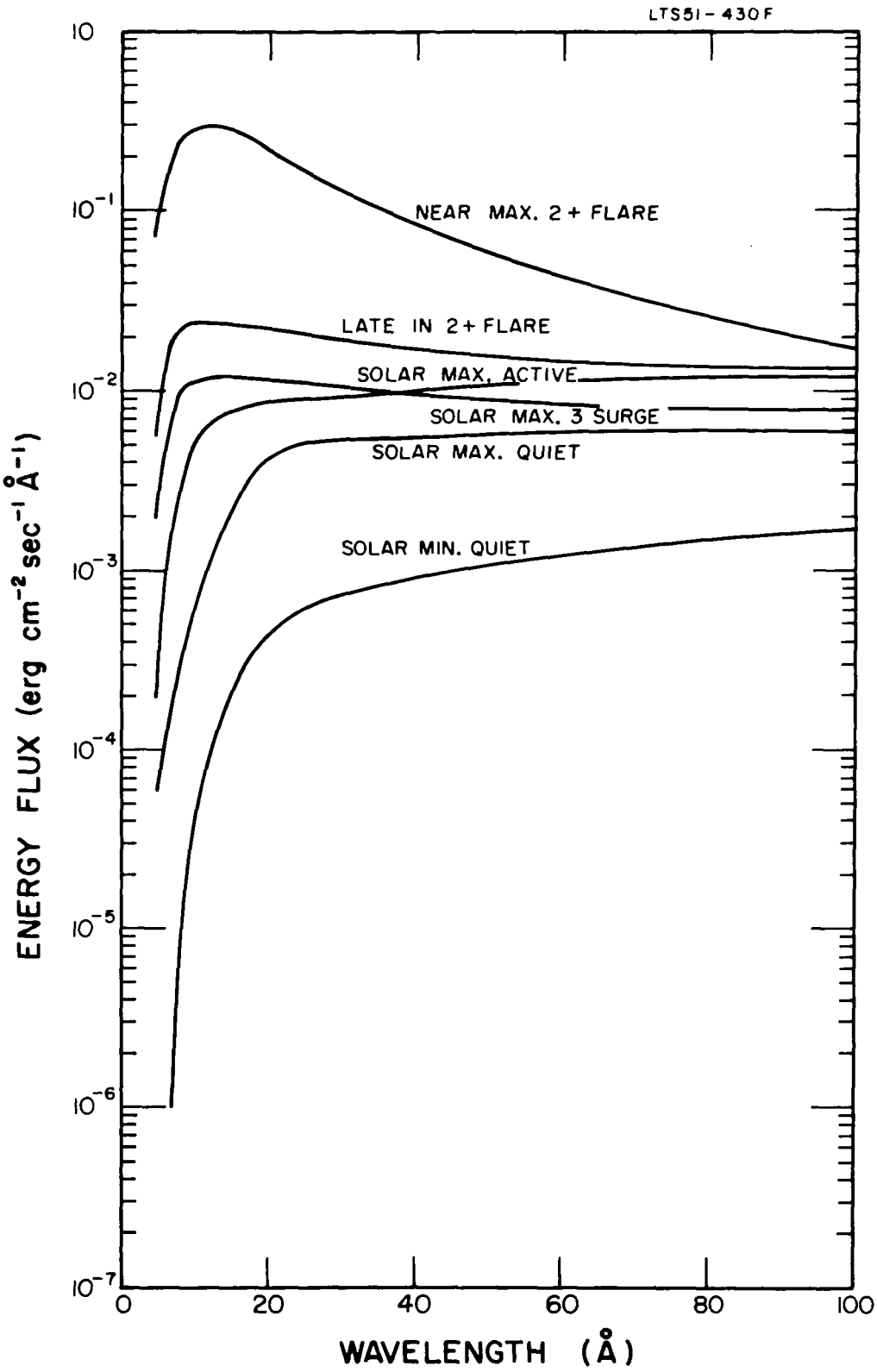

Figure 14. Solar X-ray energy flux for various solar conditions.[23]

TABLE 4

SOLAR PHOTON FLUX - CONTINUUM TO 3000Å
AT THE TOP OF EARTH ATMOSPHERE

Ref.: (a) 0-1625Å; K.Watanabe (see Atmospheric Processes, P.Nawrocki and R.Papa, Pergamon Press, 1962).
(b) 1525-2625Å; C.R.Detwiler et al., Ann. de Géophysique, 17, 263 (1961).
(c) 2525-3025Å; F.S.Johnson, J.Meteor., 11, 431 (1954).

λ±25Å	E/Photon λ	Total Flux	Photon Flux
Å	ergs photon^{-1} (x 10^{-11})	ergs cm^{-2}sec^{-1}(50Å)$^{-1}$	photon cm^{-2}sec^{-1}(50Å)$^{-1}$ (x 10^{10})
(a) 50	52.963	0.056	0.0106
100	21.185	0.075	0.0354
150	13.619	0.085	0.0624
200	10.088	0.130	0.129
250	8.0246	0.135	0.168
300	6.6666	0.072	0.108
350	5.7037	0.025	0.0438
400	4.9847	0.025	0.0502
450	4.4272	0.025	0.0565
500	3.9822	0.028	0.0703
550	3.6186	0.030	0.0829
600	3.3159	0.030	0.0905
650	3.0601	0.030	0.0980
700	2.8409	0.030	0.106
750	2.6511	0.030	0.113
800	2.4850	0.040	0.161
850	2.3386	0.150	0.641
900	2.2085	0.167	0.756
950	2.0921	0.047	0.225
1000	1.9873	0.012	0.0604
1050	1.8926	0.028	0.148
1100	1.8065	0.079	0.437
1150	1.7278	0.144	0.833
1200	1.6558	0.185	1.12
1250	1.5895	0.150	0.943
1300	1.5283	0.125	0.818
1350	1.4717	0.150	1.02
1400	1.4191	0.175	1.23
1450	1.3701	0.250	1.82
1500	1.3244	0.350	2.64
1550	1.2817	0.450	3.51
1600	1.2414	0.580	4.67
(b)1550	1.2817	1.36	10.6
1600	1.2414	3.20	25.8
1650	1.2038	4.69	39.0
1700	1.1684	8.20	70.2

TABLE 4 (continued)

SOLAR PHOTON FLUX - CONTINUUM TO 3000Å AT THE TOP OF EARTH ATMOSPHERE

$\lambda \pm 25$Å	$E/Photon_\lambda$	Total Flux	Photon Flux
Å	ergs photon^{-1} ($\times 10^{-11}$)	ergs cm^{-2} sec^{-1} (50Å)$^{-1}$	photon cm^{-2} sec^{-1} (50Å)$^{-1}$ ($\times 10^{13}$)
*1750	1.1350	12.0	0.106
1800	1.1034	18.4	0.167
1850	1.0736	28.0	0.261
1900	1.0454	40.9	0.391
1950	1.0186	55.0	0.540
2000	0.99310	70.0	0.705
2050	0.96888	90.0	0.929
2100	0.94581	145.0	1.53
2150	0.92381	240.0	2.60
2200	0.90282	310.0	3.43
2250	0.88276	350.0	3.96
2300	0.86357	360.0	4.17
2350	0.84519	320.0	3.79
2400	0.82758	340.0	4.11
2450	0.81069	390.0	4.81
2500	0.79448	380.0	4.78
2550	0.77890	560.0	7.19
2600	0.76392	700.0	9.16
(c) 2550	0.77890	490.0	6.29
2600	0.76392	765.0	10.00
2650	0.74951	975.0	13.00
2700	0.73563	1115.0	15.20
2750	0.72225	1185.0	16.40
2800	0.70936	1325.0	18.70
2850	0.69691	1815.0	26.00
2900	0.68490	2510.0	36.60
2950	0.67329	3210.0	47.70
3000	0.66207	3140.0	47.40

*Reference (b) continued [note that at λ = 1750Å, photon flux changes from ($\times 10^{10}$) to ($\times 10^{13}$)].

$$\text{Total Flux } I_o = \int_{\lambda-25}^{\lambda+25} I_o(\lambda)\, d\lambda \quad ; \quad \text{Photon Flux } Q = \frac{I_o}{E/Photon_\lambda} \quad ;$$

$$E/Photon_\lambda\Big|_{Ref.(a)} = \overline{E/Photon_{\lambda\pm25}} = \frac{hc}{2}\left(\nu_{\lambda-25} + \nu_{\lambda+25}\right)\Big/ Photon_\lambda \quad ;$$

$$E/Photon_\lambda\Big|_{Ref.(b),(c)} = \frac{hc}{\lambda}\Big/ Photon_\lambda \quad ; \quad hc = 1.9862 \times 10^{-16} \text{ erg cm}$$

Where data overlaps, photon flux was determined as per example at 1600Å:

$$Q|1550 = \left(2Q_{(a)1550} + Q_{(b)1550}\right)/3 \qquad Q|1600 = \left(Q_{(a)1600} + 2Q_{(b)1600}\right)/3$$

$$Q|1650 = Q_{(b)1600}, \text{ etc.}$$

TABLE 5

SOLAR PHOTON FLUX - EMISSION LINES TO 1850Å
AT THE TOP OF EARTH ATMOSPHERE

Ref: (a) 520-1600Å; K.Watanabe (see Atmospheric Processes, P. Nawrocki and R. Papa, Pergamon Press, 1962).
(b) 1600-1850Å; C.R. Detwiler, et al., Ann. de Géophysique, 17, 263 (1961).
†(c) 283-1215.7Å; H.E. Hinteregger, et al., Private Communication (flux measurements performed August 1961).

	λ	Identification	Mean λ in Group	E/Photon$_\lambda$	Flux	Photon Flux
	Å		Å	ergs photon^{-1} ($\times 10^{-11}$)	ergs cm^{-2} sec^{-1}	Photon cm^{-2} sec^{-1} ($\times 10^{9}$)
†	283			7.0184	0.04	0.62
†	303.8	He II		6.5378	0.3	3.8
†	335			5.9290	0.03	0.48
†	368.1			5.3958	0.03	0.60
†	465.2			4.2696	0.01	0.30
†	500			3.9724	0.02	0.44
(a)	520	Si XII		3.8197	0.02	0.52
	537	He I		3.6988	0.01	0.27
†	554	O IV		3.5853	0.02	0.53
†	584.3	He I		3.3993	0.05	1.6
†	610	Mg X		3.2561	0.03	0.80
	625	Mg X		3.1780	0.01	0.31
†	629.7	O V		3.1542	0.04	1.4
	770,80	Ne VIII	775	2.5628	0.015	0.58
†	788,90	O IV	789	2.5174	0.01	0.37
†	833,35	O II, O III	834	2.3816	0.01	0.46
†	865,85*		875	2.2699	0.05	2.3
	935,45	S VI	940	2.1130	0.0004	0.019
	938	Ly ϵ		2.1175	0.005	0.24
†	949.7	Ly δ		2.0914	0.007	0.35
†	972.5	Ly γ		2.0423	0.01	0.47
†	977.0	C III		2.0330	0.08	4.0
	990*	N III	990	2.0063	0.02	1.0
	1011*	C II, etc.	1011	1.9646	0.005	0.25
†	1025.7	Ly β		1.9363	0.05	2.5
	1032,38	O VI	1035	1.9191	0.07	3.6
	1064,75*	S IV	1069.5	1.8570	0.02	1.1
	1085	N II		1.8306	0.06	3.3
	1110*	Si III, etc.	1112	1.7862	0.03	1.7

* Indicates a blend of lines of the same and/or other elements or an unresolved multiplet.

TABLE 5 (continued)

SOLAR PHOTON FLUX - EMISSION LINES TO 1850Å
AT THE TOP OF EARTH ATMOSPHERE

	λ	Identification	Mean λ in Group	E/Photon$_\lambda$	Flux	Photon Flux
	Å		Å	ergs photon^{-1} ($\times 10^{-11}$)	ergs cm^{-2} sec^{-1}	photon cm^{-2} sec^{-1} ($\times 10^{9}$)
	1127*	Si III, etc.	1127	1.7624	0.02	1.1
	1134	N I		1.7515	0.01	0.57
	1140	C I		1.7423	0.02	1.1
	1152*	O I, etc.	1157	1.7167	0.04	2.3
	1170*		1170	1.6976	0.03	1.8
	1175	C III		1.6904	0.15	8.8
	1190*		1191	1.6677	0.02	1.2
	1200	N I		1.6552	0.02	1.2
†	1206.5	Si III		1.6462	0.08	5.1
†	1215.7	Ly α		1.6338	5.0	310.0
	1239	N V		1.6031	0.03	1.9
	1243*	N V	1245	1.5954	0.03	1.9
	1260*	S II	1258	1.5789	0.03	1.9
	1263*	Si II	1265	1.5702	0.04	2.5
	1277*		1277	1.5554	0.03	1.9
	1294*		1294	1.5350	0.04	2.6
	1302,05,06	O I	1304.5	1.5225	0.18	12.0
	1320*		1320	1.5047	0.06	4.0
	1335,36	C II	1335.5	1.4872	0.30	20.0
	1335*	O I, etc.	1335	1.4659	0.05	3.4
	1394	Si IV		1.4249	0.12	8.4
	1403	Si IV		1.4157	0.08	5.6
	1430*	S I, etc.	1430	1.3890	0.03	2.2
	1462*		1462	1.3586	0.03	2.2
	1480*	S I, etc.	1482	1.3403	0.05	3.7
	1527,33	Si II	1530	1.2982	0.07	5.4
	1548	C IV		1.2831	0.17	13.0
	1551	C IV		1.2806	0.12	9.3
	1560*	C I, etc.	1559	1.2741	0.10	7.8
(b)	1640.5	He II		1.2108	0.07	5.8
	1657.0	C I		1.1987	0.16	13.0
	1670.8	Al II		1.1888	0.08	6.7
	1808.0	Si II		1.0986	0.15	14.0
	1817.4	Si II		1.0929	0.45	41.0

* Indicates a blend of lines of the same and/or other elements or an unresolved multiplet.

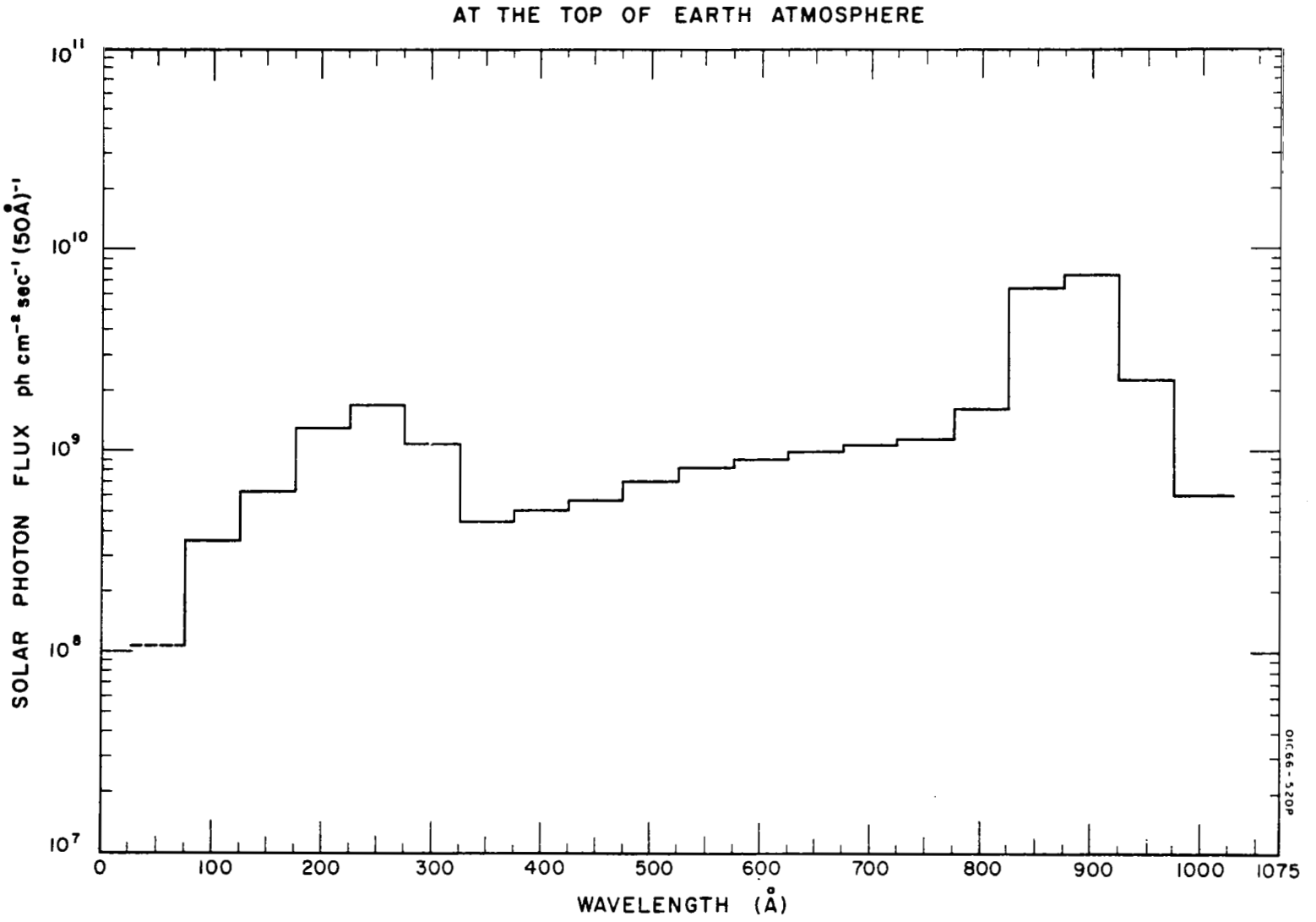

Figure 15. Solar photon flux - continuum to 1000Å

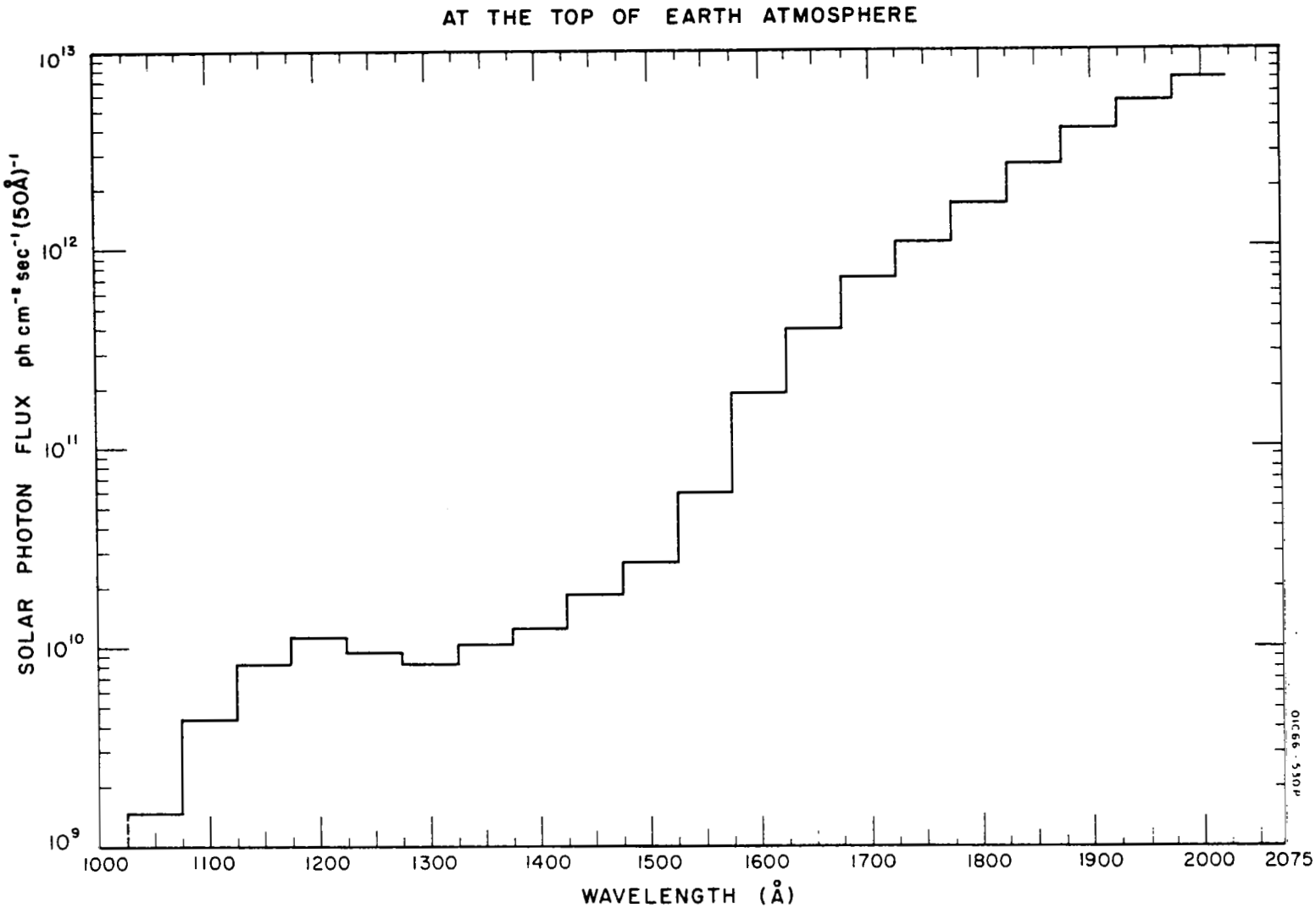

Figure 16. Solar photon flux - continuum 1000-2000Å

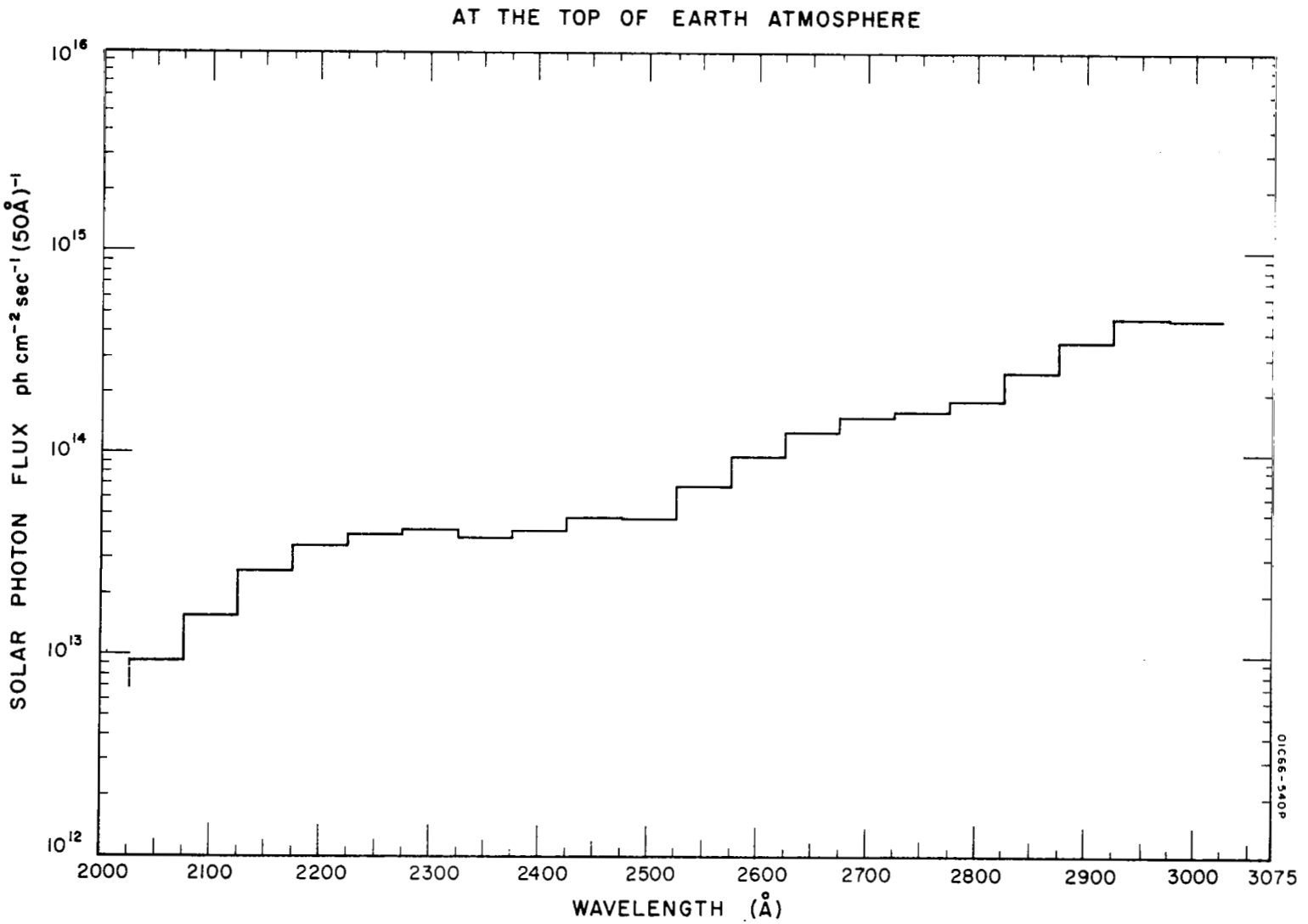

Figure 17. Solar photon flux - continuum 2000-3000Å

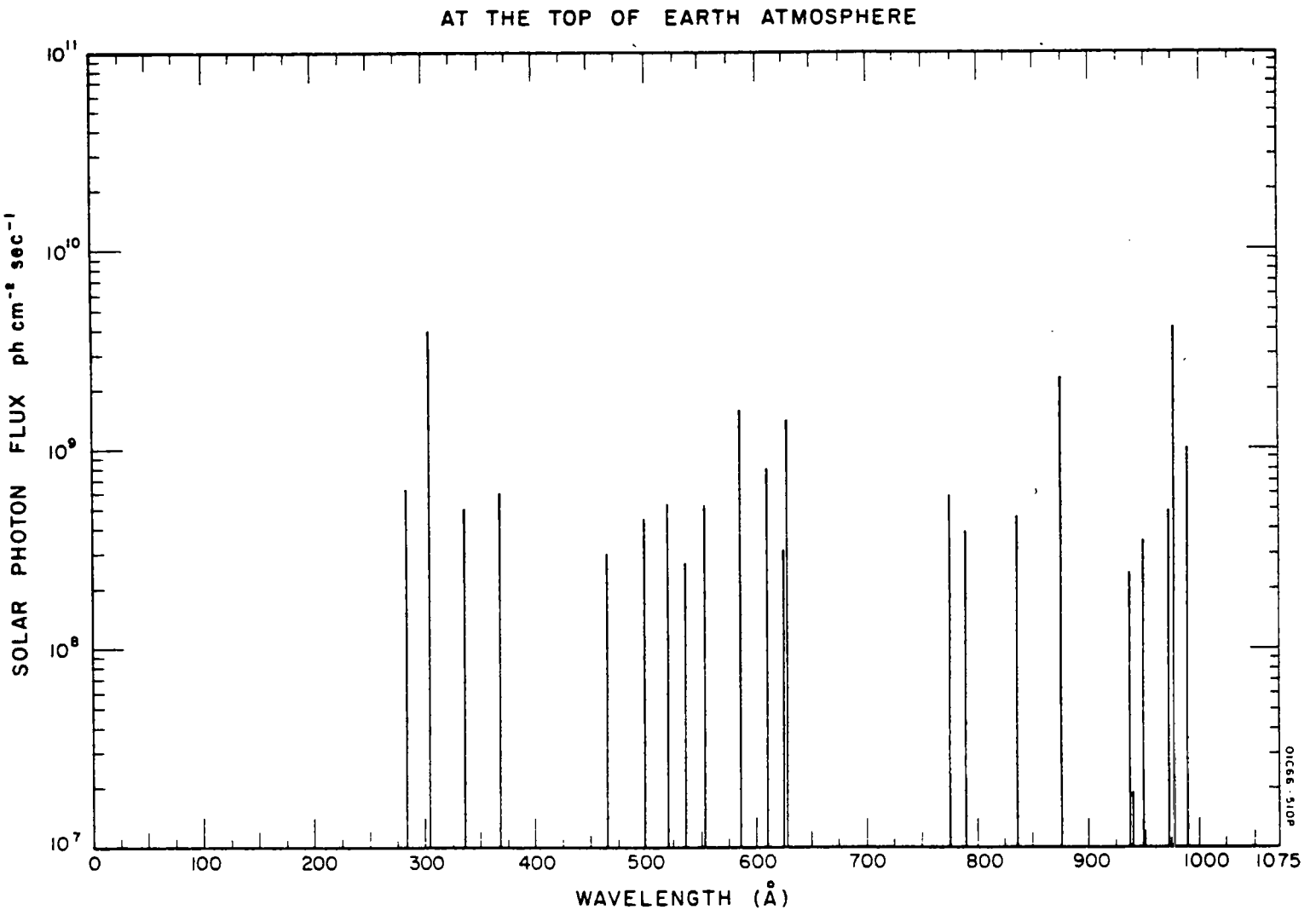

Figure 18. Solar photon flux - emission lines to 1000Å

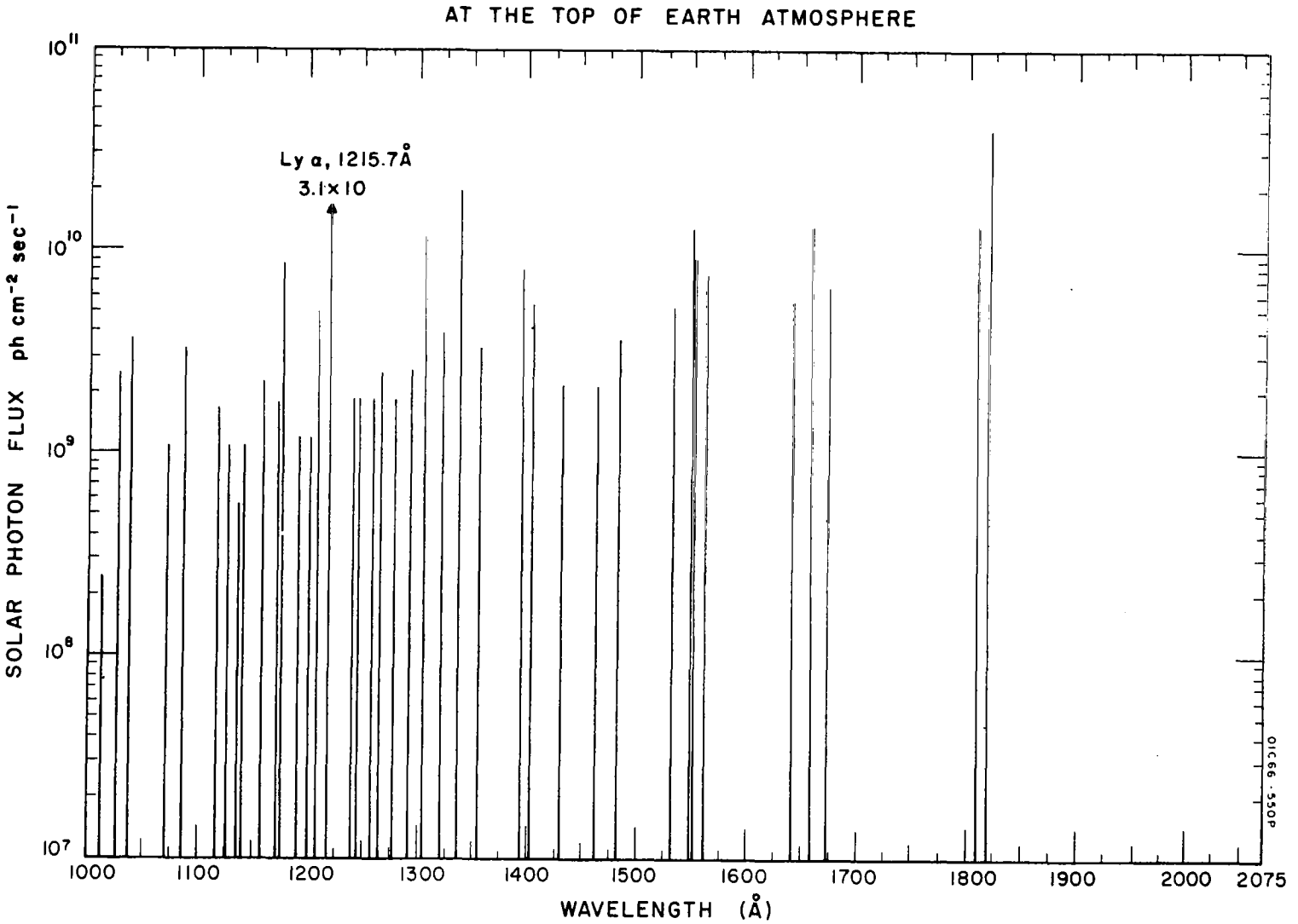

Figure 19. Solar photon flux - Emission lines 1000-1850Å

by a factor that reaches two at 2200Å. The two sets were joined at 2600Å by the method outlined in Table 4. In the far ultraviolet, the discrepancy between Tousey and Watanabe was not consistent, and the two sets of data were arbitrarily joined at 1600Å.

In Figures 15 through 19, the pure experimental data are plotted in two clear and unambiguous presentations of the tabulation; the plots provide a convenient comparison of the contribution of major emission lines with the contribution of the continuum and weak lines. As indicated in the tabulation, some of the individual emission lines contain contributions from the same and/or other elements or unresolved multiplets.

The errors in the intensity values reported by the various sources are as follows: for wavelengths longer than 2600Å, the maximum error is 10 percent; for wavelengths 500 to 2600Å, a factor of two; 80 to 500Å, a factor of three; below 80Å, again a factor of two.

III. REVIEW OF METHODS OF SIMULATION

Charged Particles

We first determine the feasibility of simulating charged particles in the D and E regions. Considering the most up-to-date measurements and the latest and most authoritative literature, the following species are considered: O_3^+, O_2^+, O_2^-, O^-, NO^+ and NO_2^+.

Although it was ascertained that very few, if any, adequate charged particle simulators are in existence, the literature was surveyed in some detail to determine not only what was available but also what laboratory experiments have been performed concerning the generation and subsequent study of charged species in the laboratory. Singer and Chopra [29] and Chopra [30] made some attempts with separate electron and ion beams; however, in general, they were unsuccessful.

Studies by G. Wehner and B. Meckel, on the other hand, have been promising. Their technique, in which a space-charge neutral low-energy plasma beam is produced provides an experimental condition whereby the motion of a satellite through an ionized medium can be simulated. Meckel [31] has used a low pressure, high density, singly charged ion plasma produced from a pool-type mercury-arc discharge system. From this plasma, ions are extracted by accelerating them to and through a mesh placed such that a fairly well defined parallel beam of ions is produced with a predetermined velocity. In order to prevent space-charge defocusing of the beam, a hot filament emits electrons in the vicinity of the plasma and thus prevents the latter from acquiring a localized charge density.

In Meckel's original setup, the operating parameters were a background pressure of 10^{-6} torr and an operating gas pressure variable between 5 and 0.001μ Hg permitting simulation from 82 to approximately 210 km. The mean free paths, therefore, are large under these experimental conditions. In addition, the plasma characteristics yield an available ion thermal velocity in the order of 10^5 cm/sec which is random in direction, an unidirectional apparent orbital body velocity of 10^6 cm/sec, an electron velocity distribution which is random in space averaging in the vicinity of 10^7 cm/sec and finally ion densities of 4×10^6 ions/cm^3.

Other similar studies have been performed by D. Hall, et al. [32], and E. Knechtel and W. Pitts [33]. Using a modified Cs ion engine, Hall, et al. [32], have produced a dilute collisionless plasma whose density

TABLE 6

SIMULATION OF NORMAL SHEATHS BY VARIOUS LABORATORIES [34]
(ZERO MAGNETIC FIELD)

	SPACE	STL	NASA	RCA
$n(cm^{-3})$	$2x10^4$	$3x10^5$ - $1.2x10^7$	10^8	10^{10}
Φ applied (volts)	-	0 - 400	-105 - -200	0 - -100
a (cm)	50	0.94 - 2.54	0.95 - 1.25	0.5
T (^oK)	$2x10^3$	$1.54x10^3$ - $1.54x10^4$	3.28×10^4	$7.74x10^3$ (1 eV)
V_o(m/s)	10^4	1.1×10^4	$8x10^6$ - $1.6x10^7$	2×10^4
W (cm)	∞	20	5	20
M (Kgms)	(He) $6.68x10^{-27}$	(Cs) 2.22×10^{-25}	(Hg) 3.36×10^{-25}	(Li) $1.169x10^{-20}$
$\sqrt{M/m}$	85.6	494	608	113.5

ranges from a maximum of about 10^6 ions/cm^3 to approximately 10^3 ions for detailed studies of wake structure. This, of course, simulates altitudes from several hundred km to approximately several thousand km. Knechtel and Pitts [33] have made some experimental investigations of electric drag on satellites with apparatus modeled after Meckel's system.

Another system which allows ions to be simulated under some geophysical conditions has been advanced by I. P. Shkarofsky [34]. In essence, his apparatus involves firing a condenser bank and ionizing metals (such as Ba, Na or Li) which are coated on the electrodes. Rather high ion velocities and densities are obtained, namely 3 x 10^6 cm/sec and 10^{12} ions/cm^3 respectively. Some decrease in ion density is noticed as the stream is allowed to expand. However, these fluxes are still somewhat excessive for ionospheric simulation. Table 6 summarizes some of the pertinent parameters that were obtained by laboratory simulation in some of the laboratories under zero magnetic field. Other pertinent data are given in Table 7, in which a comparison of parameters found in nature and in the laboratory generally are summarized.

TABLE 7

COMPARISON OF PARAMETERS FOUND IN NATURE AND IN LABORATORY [35]

	Characteristic Length cm	Charge Particle Density cm^{-3}	Particle Velocity cm/sec	Magnetic Field, gauss
Galaxy	10^{22}	10^0	...	10^{-6}
Magnetosphere	10^{10}	10^1	10^7	10^{-3}
Ionosphere	10	10^3 - 10^6	...	10^{-1}
Laboratory	10^0 - 10^1	10^{12} - 10^{15}	10^6 - 10^7	10^3 - 10^6

As part of this review, it is considered appropriate to mention some solar wind magnetosphere simulation studies with zero magnetic field. These were performed primarily by Osborne, et al., [36], Bostick, et al., [37], Claids, et al., [38], and Kawashima [39]. The state of art is summarized in Table 8.

TABLE 8

EXPERIMENTAL PARAMETERS FOR SIMULATION OF SOLAR WIND-MAGNETOSPHERE INTERACTION

	SOLAR WIND						DIPOLE FIELD		
	Charged Particle Density (cm^{-3})	Electron Temperature (^{o}K)	Duration (sec)	Velocity (cm/sec)	Ion Species	Trapped Magnetic Field Strength (Teslas)	Duration (sec)	Strength at Equator of Terrella (Teslas)	Terrella Radius (cm)
SPACE	5	2×10^{5}	10^{4} (Initial Phase Period)	5×10^{7}	H	5×10^{-9}	∞	3.11×10^{-5}	6.37×10^{8}
OSBORNE ET AL (1964) (RCA VICTOR, CANADA)	2×10^{13}	3×10^{4}	20μ	2×10^{6}	Na,Ba	0	5×10^{-3}	0.4	3
CLADIS ET AL (1964) (LOCKHEED U.S.A.)	5×10^{12}	2.3×10^{4}	20μ	6×10^{6}	H_2	0	not Specified	0.074	2.9
BOSTICK ET AL (1962) (STEVENS INST., U.S.A.)	10^{14}	not specified	10μ	2×10^{6}	Cu	0	2.7×10^{-4}	0.25 (1cm in front)	Rect.coil 5cmx37cm (2dim. dipole)
KAWASHIMA ET AL (1964) (UNIV. OF TOKYO, JAPAN)	10^{15}	not specified	15μ	3×10^{6}	He,A	0	4×10^{-4}	2	1
DANIELSSON AND LINDBERG (1964) (ROYAL INST., SWEDEN)	10^{14}-10^{15}	1.55×10^{4}	60μ	5×10^{6}	H_2	10^{-2}-7×10^{-2}	not specified	1	1.1
SCALING FACTORS	$\sim10^{13}$	$\sim$0.1	$\sim5\times10^{-9}$ (characteristic Time Scaling Factor)	$\sim$0.1	2-137	0-1.4×10^{7}	-	$\sim10^{4}$	$\sim5\times10^{-9}$ (characteristic Length Scaling Factor

Photoionization simulator. Notwithstanding some of the uncertainties of charged particle production and composition, the possibility exists of approximating the charged particle density of at least a part of the D region by photoionization, particularly since radiation sources in the uv and X-ray region are available which can produce radiation fluxes considerably in excess of the solar flux.

This mechanism of ion production has important implications, since it would facilitate, over a limited volume, at least, a good simulation of thermal charged particle densities in the presence of a relatively high neutral ambient density. One could thus, for example, perform calibration of Langmuir probes at a simulated altitude level where probe behavior is not amenable to theoretical evaluation.

To demonstrate the feasibility of simulating the charged particles in a simulation chamber by photoionization, the following calculation is performed for an infinite cylindrical vessel of radius R_2. The vessel contains a gas which is ionized by an infinite co-axial cylindrical beam of ionizing radiation of radius R_1 (Figure 20).

The following processes are responsible for the distribution of ions:

Ionization: The rate of ionization at the operating pressure is assumed to be q_p ions/cm^3/sec.

Diffusion: The diffusion is assumed to be ambipolar with a diffusion coefficient of D_{ap} cm^2/sec at the operating pressure.

Recombination: The recombination coefficient of positive ions with electrons is α cm^3/sec at the operating temperature.

The steady-state distribution of ions within the region of the beam of ionizing radiation is given by

$$D_{ap} \nabla^2 n - \alpha n^2 = - q_p \qquad (1)$$

and that outside the beam is given by the same equation where q_p is zero. Equation (1) is not analytically solvable for a cylindrical geometry. Therefore, we shall first consider the distribution of ionization under diffusive equilibrium alone. Later on, we shall find the effect of recombination on the steady-state diffusive distribution. Neglecting recombination, i.e., neglecting the second term of the lefthand side of Equation (1) we have

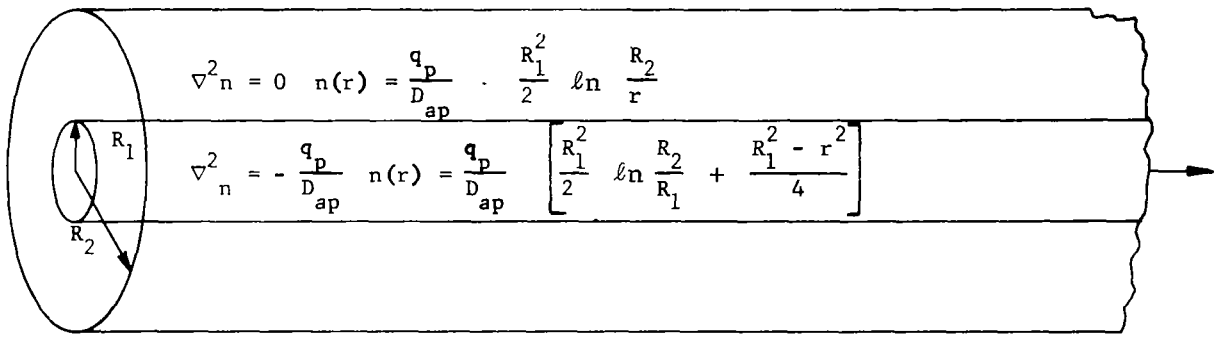

Figure 20. Schematic representation of the photoionization simulator.

$$D_{ap} \nabla^2 n = - q_p \tag{2}$$

or,

$$\nabla^2 n = - \frac{q_p}{D_{ap}}$$

which is Poisson's Equation with a source function $q_p(r)$ such that

$$\begin{aligned} q_p(r) &= q_p \quad \text{for} \quad r \leq R_1 \\ \text{and} \quad q_p(r) &= 0 \quad \text{for} \quad r > R_1 \end{aligned} \tag{3}$$

Equation (2) can be solved in cylindrical polar coordinates (r, ϕ, z) for source function (3) and the boundary condition,

$$n = o \text{ for } r = R_2 \tag{4}$$

The steady-state distribution of ionization, subject to the above boundary conditions, for a point source situated at (r_o, ϕ_o) inside the cylinder is given by [40].

$$n(r, \phi/r_o, \phi_o) = \frac{q_p(r_o, \phi_o)}{4\pi D_{ap}} \left\{ G(r, \phi/r_o, \phi_o) + 2 \ell n R_2 - 2 \sum_{n=1}^{\infty} \frac{1}{n} \left(\frac{r_o \cdot r}{R_2^2} \right)^n \text{Cos } [n(\phi_o - \phi)] \right\} \tag{5}$$

where $G(r,\phi/r_o \phi_o)$ is the appropriate Green's function. If the source function is independent of the length z of the cylinder and is only distributed as $q(r_o \phi_o)$, the steady-state distribution is given by,

$$n(r,\phi) = \frac{1}{2\pi D_{ap}} \int_o^{2\pi} d\phi_o \left\{ \int_o^r r_o \, dr_o \, [\ell n \left(\frac{R_2}{r} \right) \right.$$

$$-\sum_{n=1}^{\infty} \frac{1}{n}\left(\frac{r_o^n r^n}{R_2^{2n}} - \frac{r_o^n}{r^n}\right) \text{Cos } n(\phi_o - \phi)]\ q_p(r_o, \phi_o)$$

$$+\int_r^{R_2} r_o\, d_{ro}\left[\ell n\left(\frac{R_2}{r_o}\right) - \sum_{n=1}^{\infty} \frac{1}{n}\left(\frac{r_o^n r^n}{R_2^{2n}} - \frac{r^n}{r_o^n}\right)\right.$$

$$\left.\text{x Cos } n\ (\phi_o - \phi)\right]\quad q_p(r_o, \phi_o)\Bigg\} \tag{6}$$

Since the present source function is isotropic and only depends on r as given by (3), we find that Equation (6) reduces to

$$n(r) = \frac{1}{D_{ap}}\left[\ell n\left(\frac{R_2}{r}\right)\int_o^r q_p(r_o)\ r_o\ dr_o\right.$$

$$\left.+\int_r^{R_2} \ell n\left(\frac{R_2}{r_o}\right)\quad q_p(r_o)\ r_o\ dr_o\right] \tag{7}$$

Integrating the above equation with a source function given in (3) we have,

$$n(r) = \frac{q_p}{D_{ap}}\left[\frac{R_1^2}{2}\ \ell n\ \frac{R_2}{R_1} + \frac{R_1^2 - r^2}{4}\right] \tag{8}$$

which gives the steady state diffusive distribution of ions within the region of the beam of ionizing radiation.

The distribution of ions, outside the beam of ionizing radiation is given by

$$\nabla^2 n = 0 \tag{9}$$

which is Laplace's Equation. The solution of Equation (9) with boundary condition (4) is given by

$$n(r) = \frac{q_p}{D_{ap}} \left[\frac{R_1^2}{2} \ln \frac{R_2}{r} \right] \qquad (10)$$

Substituting the appropriate values of q_p and D_{ap} in Equations (8) and (10), we can calculate the distribution of ions in a vessel of cylindrical symmetry. We shall now discuss the processes and parameters necessary to calculate this distribution.

Ionization

Photoionization. The rate of ionization of a gas is given by Ghosh et al. [41].

$$q_{pz} = P_z \; n_p(x) = \sum_{\nu}' \; n(h\nu)_o \; K_{\nu z} \; k_\nu \qquad n_p(x) \qquad (11)$$

and

$$P_z = \sum_{\nu}' \; n(h\nu)_o \; K_{\nu z} \; k_\nu \qquad (12)$$

where

P_z - probability of ionization of the gas at a distance z from the entrance

$n(h\nu)_o$ - photon flux of wave number ν at the entrance

k_ν - absorption cross-section of the gas which is assumed to be equal to the photoionization cross-section

$K_{\nu z}$ - is transmission coefficient of the gas column of length z

$n_p(x)$ - concentration of gas molecules at pressure p

The summation is to be carried over the wavelength region which produces the ionization of the gas. The transmission coefficient in Equations (11) and (12) is given by,

$$K_{\nu z} = \exp(- n_p(x) \; . \; z \; . \; k_\nu) \qquad (13)$$

For low gas pressure and small length z of the chamber for which

$$n_p(x)\ z\ k_\nu < 1, \tag{14}$$

$K_{\nu z}$ is assumed to be equal to 1. Under the above conditions the rate of production of ions is independent of z and is given by

$$q_p = \sum_\nu n(h\nu)_o\ k_\nu\ \ n_p(x) \tag{15}$$

The probability of ionization of gases can be computed from the known absorption cross sections of the gases and the photon flux of the ultraviolet sources.

McDaniel [42] has summarized current information of the photoionization cross section of atmospheric gases. The optical absorption cross sections and the region of photoionization for different atmospheric gases is given in Table 9.

TABLE 9

OPTICAL-ABSORPTION CROSS SECTIONS OF ATMOSPHERIC GASES AT VARIOUS WAVELENGTHS

Molecule	$\lambda_{Threshold}$ (Å)	λ_{max} (Å)	k_{max}, cm^2
N_2	800	700 ± 100	2.2×10^{-17}
O_2	1050	600 ± 200	2.0×10^{-17}
NO	1250	900 ± 50	1.5×10^{-17}
CO	800	600 ± 100	2.0×10^{-17}

It is apparent from the table that the absorption cross sections in the photoionization region of these atmospheric gases is about 10^{-17} cm^2 and peak absorption lies between 950 and 400Å. Considering the characteristics of laboratory light sources of vacuum ultraviolet radiation,

it can be concluded that the following strong lines: Lyman α (1215.5Å, 10^{16} photon/sec), Lyman β (1025.7Å, $\sim 10^{10}$ photons/sec), together with others at lower wavelengths can be used for the photoionization of NO. O_2 can be photoionized by Lyman β (1025.7Å, $\sim 10^{10}$ photons/sec); C III (977.0Å, 10^{10} photons/sec) as well as radiation at lower wavelengths. However, N_2 can be effectively photoionized only by He, I (584.5Å, 10^{10} photons/sec). In Table 10 the photon flux (photon/sec) of the various laboratory light sources of vacuum ultraviolet radiation is given together with the appropriate absorption cross sections. Table 11 shows the maximum photoionization probability of some atmospheric gases which can be obtained in the laboratory. Table 12 shows the maximum rate of ion production per cm^3 at 1μ pressure. It can be concluded from Table 10 that with the available sources an ion production rate of about 10^6 ions/cm^3 sec at 1μ can be obtained.

Ionization by fast electrons. The measurements [43, 44] of plasmas generated by electron beams in gases in the pressure range of 10^{-4} to 10^{-2} torr indicate that ion densities many times the electron beam density can be generated. At these pressures, the scattering suffered by the beam electrons is very small. At higher or lower pressures, the situation is different. At very low pressures, the plasma formed by the beam is typically of about the same density as the beam. At high pressures, the beam is scattered so rapidly that only very short chambers can be used. However, in some cases, electron beam ionization can be used in place of photoionization. The advantages of using electron beam ionization are a higher rate of ion production and better controllability of the electron beam density as compared to the photon beam density.

The rate of primary ionization per cm^3 produced by an electron beam is given by

$$q = I.\ N.\ \sigma_i(E) \qquad (16)$$

where,

I = number of electrons/cm^2 sec in the electron beam

$\sigma_i(E)$ = ionization cross-section of the gas by electrons of energy E(eV)

N = number density of gas molecules in the vessel.

Recently, McDaniel [42] and Hasted [45] have reviewed the ionization cross-sections of various gases by electron bombardment. The data are summarized in Table 13.

TABLE 10

ABSORPTION CROSS SECTIONS OF ATMOSPHERIC GASES AT WAVELENGTHS OF THE STRONG LINES OF LABORATORY UV SOURCES

Gas \ λ(Å) Flux (Photons/cm^{-2} sec^{-1})	1215.5 10^{16} Lyman α	1025.7 10^{10} Lyman β	977.0 10^{10} C III	937.8 10^{8} Lyman ϵ	584.5 10^{10} He I	303.8 10^{7} He II
Nitrogen	2.44×10^{-18}	1.0×10^{-21}	8.2×10^{-19}	1.07×10^{-17}	2.31×10^{-17}	1.21×10^{-17}
Oxygen	1.85×10^{-20}	1.25×10^{-18}	3.98×10^{-18}	2.0×10^{-17}	1.19×10^{-17}	1.66×10^{-17}
Nitric Oxide	3.7×10^{-18}	1.07×10^{-17}	2.29×10^{-17}	1.55×10^{-17}	2.4×10^{-17}	1.65×10^{-17}
Carbon Monoxide	--	$< 1.5 \times 10^{-20}$	4.0×10^{-18}	1.5×10^{-17}	2.26×10^{-17}	1.14×10^{-17}

TABLE 11

PROBABILITY OF IONIZATION, P sec^{-1}

Gas \ λ(Å)	1215.5	1025.7	977.0	937.8	584.5	303.8
Nitrogen	0	0	8.2×10^{-19}	1.07×10^{-9}	2.31×10^{-7}	1.21×10^{-10}
Oxygen	0	1.25×10^{-8}	3.98×10^{-8}	2.0×10^{-9}	1.19×10^{-7}	1.66×10^{-10}
Nitric Oxide	3.7×10^{-2}	1.01×10^{-7}	2.29×10^{-7}	1.55×10^{-9}	2.4×10^{-7}	1.65×10^{-10}
Carbon Monoxide	0	0	4.0×10^{-8}	1.5×10^{-9}	2.26×10^{-7}	1.14×10^{-10}

TABLE 12

RATE OF PHOTOIONIZATION AT 1μ (ions/cm^3/sec)

Gas	q(1215.5A)	q(1025.7A)	q(977.0A)	q(937.8A)	q(584.5A)	q(303.8A)
Nitrogen	0	0	2.94×10^5	3.83×10^4	8.3×10^6	4.35×10^3
Oxygen	0	4.5×10^5	1.43×10^6	7.2×10^4	4.3×10^6	6.0×10^3
Nitric Oxide	1.33×10^{11}	3.62×10^6	8.25×10^6	5.6×10^4	8.6×10^6	5.95×10^3
Carbon Monoxide	0	0	1.44×10^6	5.4×10^4	8.15×10^6	4.1×10^3

TABLE 13

IONIZATION CROSS-SECTION (cm^2)
ELECTRON ENERGY

Gas	Electron Energy 50 eV	100 eV	1 kev	100 keV	1 MeV
H_2	1.22×10^{-16}	1.31×10^{-16}	2.7×10^{-17}	1×10^{-16}	3.5×10^{-17}
N_2	2.22×10^{-16}	2.63×10^{-16}	1.00×10^{-16}	2.4×10^{-16}	1.5×10^{-16}
O_2	2.13×10^{-16}	2.9×10^{-16}	1.1×10^{-16}	2.4×10^{-16}	1.5×10^{-16}
CO	2.56×10^{-16}	3.06×10^{-16}	1.0×10^{-16}	2.6×10^{-16}	1.4×10^{-16}

It is apparent from the above table that the ionization cross-section of about 10^{-16} cm^2 can be assumed for the ionization of atmospheric gases by high energy (~ keV) electrons. Assuming a pressure of 1μ and an electron flux of 1μ A/cm^2, we find that the rate of ionization is given by,

$$q = 6 \times 10^{12} \times 3 \times 10^{13} \times 10^{-16} \text{ ions/cm}^3 \text{ sec.}$$

$$= 1.8 \times 10^{10} \text{ ions/cm}^3 \text{ sec.}$$

The maximum rate of ionization at this pressure by photoionization is about 10^6 ions/cm^3, which is about four orders of magnitude less than the rate of ionization produced by electron impact. The above rate of ionization can be further increased by increasing the flux of the incident electron beams.

Diffusion. The diffusion of electrons and ions through a gas is an important process for controlling the distribution of ions in an ionospheric simulator. If the density of ionization is low, each charged particle species should be considered as an independent gas. The charged particles of either polarity, namely electrons and positive ions, diffuse through the neutral gas without appreciably interacting with particles of the same or of opposite charge.

Fick's law of diffusion states:

$$\vec{J} = -D \nabla n \tag{17}$$

where $\vec{J}$ is the particle current density, D is the diffusion coefficient and ∇n is the density gradient of the diffusing particles. The above equation holds only in binary mixtures at uniform temperatures and pressure. It can be shown that even with an ion density of 10^{12} ions cm^{-3} the thermal energy of ions is several times greater than the average potential energy of electrostatic interaction between ions. For ion concentrations less than 10^7 - 10^8 ions cm^{-3}, space charge effects are negligibly small and the electrons and ions diffuse independently.

The mutual diffusion of a single particle (electron or ion) in a gas depends on the type of interaction between the two. According to the Chapman-Enskog theory, the ion-atom mutual diffusion coefficient is given by

$$D_{12} = \frac{3\sqrt{\pi}}{16} \left(\frac{2\ kT}{M_r}\right)^{7/2} \frac{1 + \epsilon_o}{(N_1 + N_2)P_{12}} \tag{18}$$

where,

$$P_{12} = \int_o^\infty v_o^5\ q_D\ (v_o)\ e^{-M_r v_o^2/2\ kT}\ d_{vo} \tag{19}$$

and

$$q_D(v_o) = 2\pi \int_o^\infty (1 - \cos\theta) b\ db \tag{20}$$

where M_r is the reduced mass of the ion-molecule system, N_1 and N_2 are, respectively, the gas and ion number densities, ϵ_o is a second order correction which is usually less than the experimental error. The ionic number density N_2 is usually less than the gas density N_1 and, therefore, can be ignored. P_{12} is an average of the diffusion cross-sections and depends on the nature of the ion-molecule interaction through the impact parameter b and scattering angle θ. Therefore, the diffusion coefficient can be obtained from the theoretically computed diffusion cross-section q_D.

The information regarding the diffusion coefficient of ions in gases can also be obtained from reduced mobility data. The relation between the reduced mobility and the diffusion coefficient is given by [42]

$$\frac{K_i}{D_i} = \frac{1.16 \times 10^4}{T} \tag{21}$$

where T is the temperature of the gas. The above relation is exactly correct for an interaction potential $V(r) \propto r^{-4}$ only. Table 14 gives the reduced mobility of some atmospheric ions in their parent gases.

TABLE 14

MOBILITY OF GASEOUS IONS

Ion	Gas	Mobility (cm^2/volt-sec)
H_2^+	H_2	12.0
N_2^+	N_2	1.8
O_2^+	O_2	1.6
CO^+	CO	2.25

A representative value of about 50 $cm^2 sec^{-1}$ for the diffusion coefficient of atmospheric ions is obtained at 273°K and 1 torr pressure, corresponding to the reduced mobility of about 2.5 cm^2/volt-sec.

The relation between the electronic mobility and its diffusion coefficient is given by the following modified expression [42]:

$$\frac{K_e}{D_e} = \eta \frac{kT}{e} \tag{22}$$

where η equals the ratio of the mean translational energy of the electrons to the mean thermal energy of the gas molecules. It should be noted that electrons produced by photoionization of gases will have the excess energy of the photon. The energy possessed by the photoelectrons is equal to $h(\nu - \nu_o)$ where ν_o is the threshold frequency of

ionization and ν is the frequency of the ionizing photons. Therefore, the diffusion coefficient of the electrons should vary with the wavelength of the ionizing radiation. It may also be noted that high-energy secondary electrons are produced during the ionization of gases by fast electrons. However, from the published data [42] of electron drift velocities, it may be concluded that the diffusion coefficient of low energy (approximately thermal) electrons in atmospheric gases is about 5×10^4 cm^2/sec at 273°K and 1 torr.

In the above discussion we have considered the free diffusion of ions and electrons, neglecting the effects of electrostatic interaction and space charge fields. The diffusion of electrons is much more rapid ($D_e \sim 5 \times 10^4$ cm^2/sec^{-1} at 273°K and 1 torr) than that of positive ions ($D_i \sim 50$ cm^2/sec at 273°K and 1 torr). Therefore, even at low ion densities ($N_i < 10^{12}$ ions cm^{-3}) where electrostatic interaction between ions is negligible, the more rapid diffusion of electrons can produce net space charge field of considerable magnitude. This space charge field accelerates the diffusion of positive ions and retards the diffusion of electrons. Therefore, under equilibrium condition, the electrons and ions diffuse together with a common diffusion coefficient given by,

$$D_a = \frac{D_i K_e + D_e K_i}{K_i + K_e} \tag{23}$$

where D_i and D_e represent the diffusion coefficients K_i and K_e the mobilities of ions and electrons, respectively.

If a thermally-equilibrated plasma consisting only of electrons and positive ions is contained in a vessel, the faster-moving electrons tend to diffuse outward to the container wall. The excess positive charge left behind then retards the electrons. However, the difference between the distribution of positive ions and electrons can only be maintained within a certain distance in the plasma, which is known as Debye shielding distance, λ_{De}. For an ion in a plasma this is given by

$$\lambda_{De} = \left[\frac{\epsilon \, kT_e}{4\pi \, e^2 \, n_e} \right]^{1/2} \tag{24}$$

The free diffusion of electrons and ions can only be maintained in a vessel of dimensions less than λ_{De}. However, if the dimension of the

vessel is larger than λ_{De}, the diffusion of ionization is ambipolar. In a large vessel the diffusion of ionization in a region near the wall (distance $< \lambda_{De}$) is free, and in regions distant from the wall (distance $\gg \lambda_{De}$) it is ambipolar. Table 15 shows the Debye length for the plasma of different electron densities.

TABLE 15

DEBYE LENGTH vs. ELECTRON DENSITY

n(e) electrons/cm^3	λ_{De} (cm)
1	121
10	38.2
10^2	12.1
10^3	3.82
10^4	1.21

It is apparent from the above table that near the wall of the vessel the distribution of ions and electrons may be considerably different from that calculated from the ambipolar diffusion equilibrium. However, the assumption of ambipolar diffusion in the central region of a simulation chamber of about 100 cm diameter is valid only down to ion densities of 10^2 ions/cm^3. The ambipolar diffusion coefficient of about 150 cm^2 sec^{-1} may be assumed for the atmospheric ions in atmospheric gases. Representative values of the diffusion coefficient are listed in Table 16.

TABLE 16

DIFFUSION COEFFICIENT AT 1 TORR AND 273°K

Free Diffusion	Electron	5×10^4 cm^{2}sec^{-1}
	Positive ions	50 cm^{2}sec^{-1}
Ambipolar Diffusion		150 cm^{2}sec^{-1}

Recombination. The recombination of a positive ion with an electron can proceed by the following mechanisms:

(i) Radiative Recombination

$$A^+ + e \rightarrow A + h\nu$$

(ii) Dielectronic Recombination

$$A^+ + e \rightarrow A'' \rightarrow A' + h\nu$$

(iii) Dissociative Recombination

$$AB^+ + e \rightarrow A' + B'$$

(iv) Three body recombination

$$A^+ + e + M \rightarrow A + M'$$

The mechanism (iv) is significant only at high pressures and, therefore, can be neglected in ionospheric simulation studies. Dissociative recombination (iii) is only possible for polyatomic ions. In general, the rate coefficient of the dissociative recombination is several orders of magnitude higher than the first mechanisms (i) and (ii). Therefore, in the case of molecular ions, the recombination is controlled by dissociative recombination. The mechanisms (i) and (ii) are mainly responsible for the recombination of atomic ions. The recombination coefficients of some ions of interest are given in Table 17 [42].

TABLE 17

RECOMBINATION OF POSITIVE IONS

Ions	Mechanism	Rate Coefficient (cm^3/sec)
O^+	Radiative Recombination	$3\text{-}2 \times 10^{-12}$
H^+	Radiative Recombination	$4.8\text{-}3.1 \times 10^{-12}$
N_2^+	Dissociative Recombination	$(2.8 \pm 0.5) \times 10^{-7}$
O_2^+	Dissociative Recombination	$(1.7 \pm 1) \times 10^{-7}$
NO^+	Dissociative Recombination	3.2×10^{-7}

Calculations. The distribution of ionization in an ionospheric simulator of cylindrical symmetry can be calculated from Equations (8) and (10). The expressions within brackets depend on the geometry of the cylinder and the distance r at which the ion density is required. We assume that the radius of the vessel is 50 cm and that of the ionizing beam is 1 cm. The distribution of ionization is calculated for ambipolar diffusion. From Table 16 the ambipolar diffusion coefficient is given by

$$D_{ap} = \frac{1.5 \times 10^5}{p} \tag{25}$$

where p is the pressure in microns. From Table 12, the rate of photoionization as a function of the pressure p (microns) is given by

$$q_p = 10^6 p \tag{26}$$

Therefore q_p/D_{ap} is given by

$$\frac{q_p}{D_{ap}} = \frac{10^6 \, p^2}{1.5 \times 10^5} \tag{27}$$

The calculated distribution of ionization with distance from the axis of the cylinder is given in Table 18.

TABLE 18

CONCENTRATION OF IONS vs. PRESSURE AND RADIAL DISTANCE

Pressure Microns	$\frac{q_p}{D_{ap}}$	Concentration of Ions n_o^*	n_1^*	n_{25}^*	n_{40}^*	n_{49}^*
1000	6.65×10^6	1.46×10^7	1.30×10^7	2.3×10^6	7.3×10^5	6.6×10^4
100	6.65×10^4	1.46×10^5	1.30×10^5	2.3×10^4	7.3×10^3	6.6×10^2
10	6.65×10^2	1.46×10^3	1.30×10^3	2.3	7.3×10^{-1}	6.6×10^{-2}

*The subscript denotes the radial distance from the axis of the cylindrical chamber.

It can be concluded from Table 18 that ion concentrations comparable to the maximum ionospheric concentration can be obtained at a pressure of about 100μ by photoionization. The Debye length at these concentrations (10^5 - 10^3 ions/cm^3) is much smaller (< 4 cm, Table 15) than the dimension of the vessel. Therefore, the principal mode of diffusion is ambipolar diffusion.

In order to estimate the effect of recombination on the diffusive distribution of ions, we now compare the rate of ionization with the rate of dissociative recombination. We also compare the equilibrium concentration of ions when dissociative recombination is the predominant mode of loss of ions with that when the diffusion is the predominant loss process of the ionization. The calculated values of the rate of ionization q, the rate of dissociative recombination αn^2, and the equilibrium concentration of ions under dissociative recombination $n_{eq} = \sqrt{\frac{q}{\alpha}}$ are given in Table 19. The dissociative recombination coefficient α is assumed to be equal to 1.7×10^{-7} cm^3/sec (See Table 17).

TABLE 19

Pressure Micron	q_p ions/cm^3	αn^2 ions/cm^3	n_{eq} $\sqrt{q/\alpha}$	Debye length at the axis, cm	Debye length at the wall, cm
1000	10^9	5.9×10^7	5.9×10^7	0.03	0.48
100	10^8	5.9×10^3	1.86×10^7	0.31	4.85
10	10^7	5.9×10^{-1}	5.9×10^6	3.12	48.5

The comparison of n_{eq} (Table 19) with n_o (Table 18) shows that even up to a pressure of 1 torr, the diffusive equilibrium predominates under steady-state conditions. The loss of ionization by dissociative recombination is always less than that by diffusion. Diffusion is ambipolar at pressures higher than 10μ and free at lower pressures.

From the previous discussion it is apparent that the ionospheric charged particle density (Figure 2) can be simulated by photoionization over a cylindrical volume of approximately 50 cm diameter at an ambient pressure of about 100μ, corresponding to an altitude of 80 km. At higher pressures (lower altitude), the charge density produced by photoionization is too high, at higher altitudes it is too low.

For the simulation of charged particle densities at higher altitudes, it becomes necessary to employ either an electron beam to ionize the gas in the chamber directly or to employ an external plasma gun. In either case, ionization can no longer be obtained under conditions of thermal equilibrium

Plasma gun simulator. Whereas a good approximation to the appropriate thermal equilibrium conditions of charged species (ions and electrons) can be achieved by photoionization in simulating the lower D region, this is not possible in the E region where the ambient neutral density is much lower. Here, diffusion to the walls of a simulation chamber would be so rapid that ion production by photoionization becomes impractical. A compromise solution has to be adopted which involves the production of a space-charge neutral plasma. As an example, electron densities as high as 10^6 cm^{-3} have been achieved by R. B. Cairns [46] of the GCA Technology Division staff. Cairns employed a mercury plasma over the pressure range 10^{-2} to 10^{-4} torr to establish the electron collision frequency for these densities but with no attempt to relate the data to the neutral or ionic species involved. One disadvantage noted in employment of this technique was that a higher electron temperature than desirable was encountered, but this feature was deemed unavoidable. In brief, the main purpose of this simulation experiment was to test probe theory in the intermediate region between collision-free and collision-controlled electron motion under conditions which correspond to the terrestrial D region of the ionosphere. In a dynamic system, it is possible to achieve the pertinent charged species number densities with a plasma gun of special design [31]. Such species are extracted from the plasma and accelerated to some desired velocity (i.e., that appropriate to an orbital vehicle), and are then space-charge neutralized by electrons supplied from an auxiliary hot filament. This technique has recently been explored by the GCA Technology Division under a NASA-sponsored program designed to simulate the ambient conditions encountered by an Earth-bound satellite.

Only the energy of the positive ions can be controlled correctly. The electrons introduced to space-charge neutralize the beam do not obey a Maxwellian energy distribution and thus cannot be used directly to calibrate Langmuir probes and other instruments for the measurement of electron density and energy. The results of this investigation are described in reference [1]. In summary, GCA designed and constructed a simulation chamber and mass spectrometer to test a plasma gun built by Physics Technology Laboratories. The gun was designed to produce an ion beam of variable diameter (1 to 15 cm), variable energy (1 to 10 eV) with a current density of 2×10^{-8} A/cm^2, for molecular and atomic ions of the atmospheric gases.

Although the development of the plasma source is not yet complete, it was possible to show that energies of the order of 10 eV can be obtained. Furthermore, it is possible to achieve exceptionally high rates of dissociation of molecular ions (30 percent N^+ ions from molecular nitrogen). Anyone acquainted with the difficulties of producing low energy plasma beams will appreciate the significance of these results.

Solar Ultraviolet Spectrum

The latest techniques concerning the simulation of the important solar ultraviolet emission lines with various light sources have been extensively evaluated. In addition, several of the staff members at the GCA Corporation who have actively engaged in the research of vacuum ultraviolet spectroscopy were repeatedly consulted. The consensus of opinion of these studies is presented below.

The most applicable method for simulating the solar ultraviolet lines at the required intensities is presented in Table 20. Under these experimental conditions the dc hot filament discharge lamp appears to be the most appropriate light source. The Lyman α (1215.7Å) line which is very important in the formation of the D region can be produced in the laboratory monochromatically with sufficiently high intensities. This can be achieved by using a 40 to 60 percent mixture of hydrogen and helium and a LiF window.

The simulation of all other solar ultraviolet lines, however, will necessitate differential pumping since these wavelengths lie below the transmission cutoff of lithium fluoride. It is expected that the simulation of the 304Å HeII line will be difficult. This line can be produced only under ideal conditions with a spark discharge lamp. Since more than 90 percent of this line is absorbed by the atmosphere above 140 km, it may be wise to avoid this line completely.

The design and performance details of the various light sources are contained in the discussion of the conceptual design of the simulation facility.

Solar X-ray Spectrum

Simulation parameters. Since 1949, the measurement of X-ray emission from the sun has been studied by Friedman and colleagues at NRL [47]. British and Soviet observations have also been made [48, 49, 50]. These measurements have provided X-ray data distributed over almost a full solar cycle, particularly in the 2 to 8, 8 to 20, 44 to 60Å, and 44 to 100Å bands of the X-ray spectrum. Earlier NRL and Soviet observa-

TABLE 20

SIMULATION OF SOLAR ULTRAVIOLET AND X-RAY FLUX
FOR THE D AND E REGION

Radiation	Ionosphere Region	Solar Flux (photons/sec)	Laboratory Simulation (photons/sec)	Normal Method of Simulation		Other Instrumentation
				Lamp	Gas	
1215.5Å, Lyman α	D	3.1×10^{11}	10^{16}	dc filament discharge	H_2 and H_e	None
1025.7Å, Lyman β	E	3.1×10^{9}	$\sim 10^{10}$	dc filament discharge	H_2	Differential Pumping
977.0Å, C III	E	2.5×10^{9}	10^{10}	dc filament discharge	CO_2, trace of O_2	Differential Pumping
937.8Å, Lyman ϵ	E	3.1×10^{8}	10^{8}	dc filament discharge	H_2	Differential Pumping
800-910Å, Lyman Continuum	E	1.2×10^{10} (integrated)	-	Cannot be simulated.		
584.5Å, He I	E	1.6×10^{9}	$\sim 10^{10}$	dc filament discharge	He	Differential Pumping
303.8Å, He II	E	3.8×10^{9}	$\sim 10^{7}$	High voltage spark discharge	He	Differential Pumping

TABLE 20 (Continued)

Radiation	Ionosphere Region	Solar Flux (photons/sec)	Laboratory Simulation (photons/sec)	Normal Method of Simulation		Other Instrumentation
				Lamp	Gas	
10-100Å X-ray	E	2×10^8 (integrated)	10^{15}	Soft X-ray generator		
Below 10Å	D	Only observed during the disturbed sun.				

tions were made mainly with ion chambers, Geiger counters, and photon counters. All of these provided narrow band integrated intensities over the respective bandwidths. A few were carried out with thermoluminescent phosphors. The U.K. satellite Ariel advanced the state-of-the-art by the introduction of the nondispersive proportional counter spectrometer [51]. This instrument determines the shape of the spectrum, but it cannot distinguish line emission. A further advance was recently achieved by NRL with dispersive spectrum analysis. Several review articles on the various experiments conducted, comparisons of the detectors used, and analyses of the data have been published [21, 47, 52, 53].

The problem of the relative roles played by the solar X-rays (40 to 100Å) and ultraviolet radiation (912 to 1030Å) in the formation of the E region has yet to be resolved [13, 14, 54, 55]. A conservative approach, clearly, would be to consider both possibilities and even to extend the simulated X-ray spectrum to 10Å. However, the initial investigation of this specific problem for the present contract supports the X-ray hypothesis [15]. Accordingly, for optimum design only 40 to 100Å need be simulated for the normal E region. For normal solar conditions in the D region, hard X-rays (1 to 10Å) need not be considered. Radiation at these wavelengths penetrates to the D region only during enhanced solar activity [5,6]. On this basis and also because quiet solar conditions will persist for several years simulation of the solar X-ray flux reduces to a relatively routine task. Should consideration of extreme solar conditions become necessary, simulation can be achieved without difficulty but would require more elaborate and costly equipment. The ranges in the operating specifications of the X-ray source proposed for the present application permit the extension of the soft X-ray spectrum to 10Å. For the inclusion of hard X-rays (< 10Å), two approaches can be considered: a hard X-ray generator, specifically designed and mounted within the chamber; alternatively, an industrial commercial X-ray tube installed externally to one of the chamber ports. The photon flux intensities of commercially available tubes are compatible with the simulation requirements. Since a great variety of commercial support equipment is available for industrial X-ray tubes, the latter installation appears to be more economical and reliable, particularly since its operation will be independent of the pressure in the simulation chamber.

The fine structure of the solar soft X-ray spectrum has not been determined to-date, although progress in instrumentation has made such a measurement feasible for future probe missions [51,56]. Accordingly, the most practical approach to simulation is the production of an integrated intensity equal to the known integrated solar intensity. In consequence, an expensive X-ray vacuum spectrograph, as has been described by Kirkpatrick [57] for the wavelength range from 5Å to 120Å is not needed to simulate the spectral distribution.

The upper pressure limit of operation of a soft X-ray source probably should not exceed 10^{-4} torr. Because of the interaction of X-rays with the gas in the chamber (see Figures 21 and 22 for the absorption cross section of air for X-rays), a glow discharge can readily occur at the potential applied to the X-ray source. The lowest representative altitude for soft X-ray simulation thus lies between 100 and 105 km.

Laboratory production of X-rays. X-rays are usually produced in the laboratory when the atoms of an element, mostly metallic, are bombarded with high energy electrons. The material bombarded is termed the anode, or target. In modern practice, X-rays are generated in a Coolidge-type tube evacuated to at least 10^{-5} torr, in which the electrons are emitted by a heated tungsten filament, the cathode. The thermionic electrons are accelerated by a high potential difference between anode and cathode. When an electron with sufficient energy strikes the target, it ejects an inner-shell electron from one of the target atoms. The resulting vacancy in the shell is immediately filled by an electron from an outer shell with the emission of an X-ray quantum of energy, $h\nu$, equal to the decrease in potential energy experienced by the electron. When this occurs, a line spectrum, characteristic of the element, is produced. In addition to the line spectrum, a continuous background spectrum (Bremsstrahlung) arises due to the sudden deceleration of those electrons striking the anode which do not eject bound electrons. The X-rays thus produced are radiated through a suitable window, which, in the most usual case, is the glass envelope of the tube, but, in special cases may be a light-metal foil or thin-plastic sheet transparent over the desired wavelength region of the X-rays.

X-ray tubes with sophisticated modifications of the Coolidge-type are available from industrial and commercial sources. Nearly all off-the-shelf tubes have operating voltages in excess of 15 kV corresponding to the hard to very-hard X-ray regions (< 1Å). One such tube, available from Machlett Laboratories [58] uses a beryllium window with a peak operating voltage of 40 kV (0.3Å max.) and a plate current of 50 mA. Although the X-ray cutoff of this tube extends to longer wavelengths than tubes with glass windows, it occurs at 8Å. This is much shorter than the spectrum desired which extends to almost 100Å. Leading commercial and industrial manufacturers were consulted regarding the availability of X-ray tubes operating in the 10 to 100Å region. Whereas, in theory, a soft X-ray tube is simple enough to construct for most specifications, none are apparently available commercially, primarily because of their limited application [59]. Other possibilities were

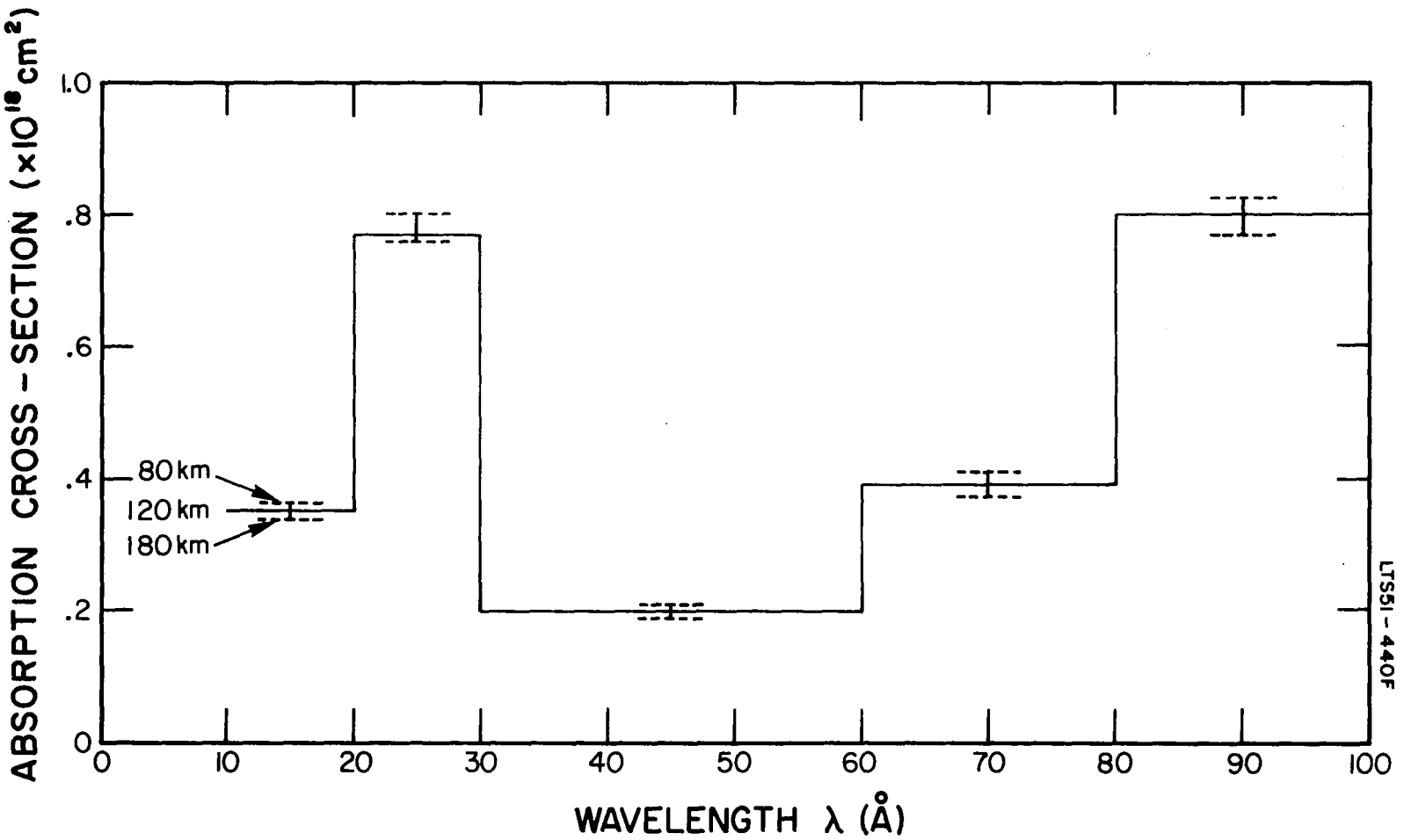

Figure 21. Total absorption cross section of air at X-ray wavelengths.[22]

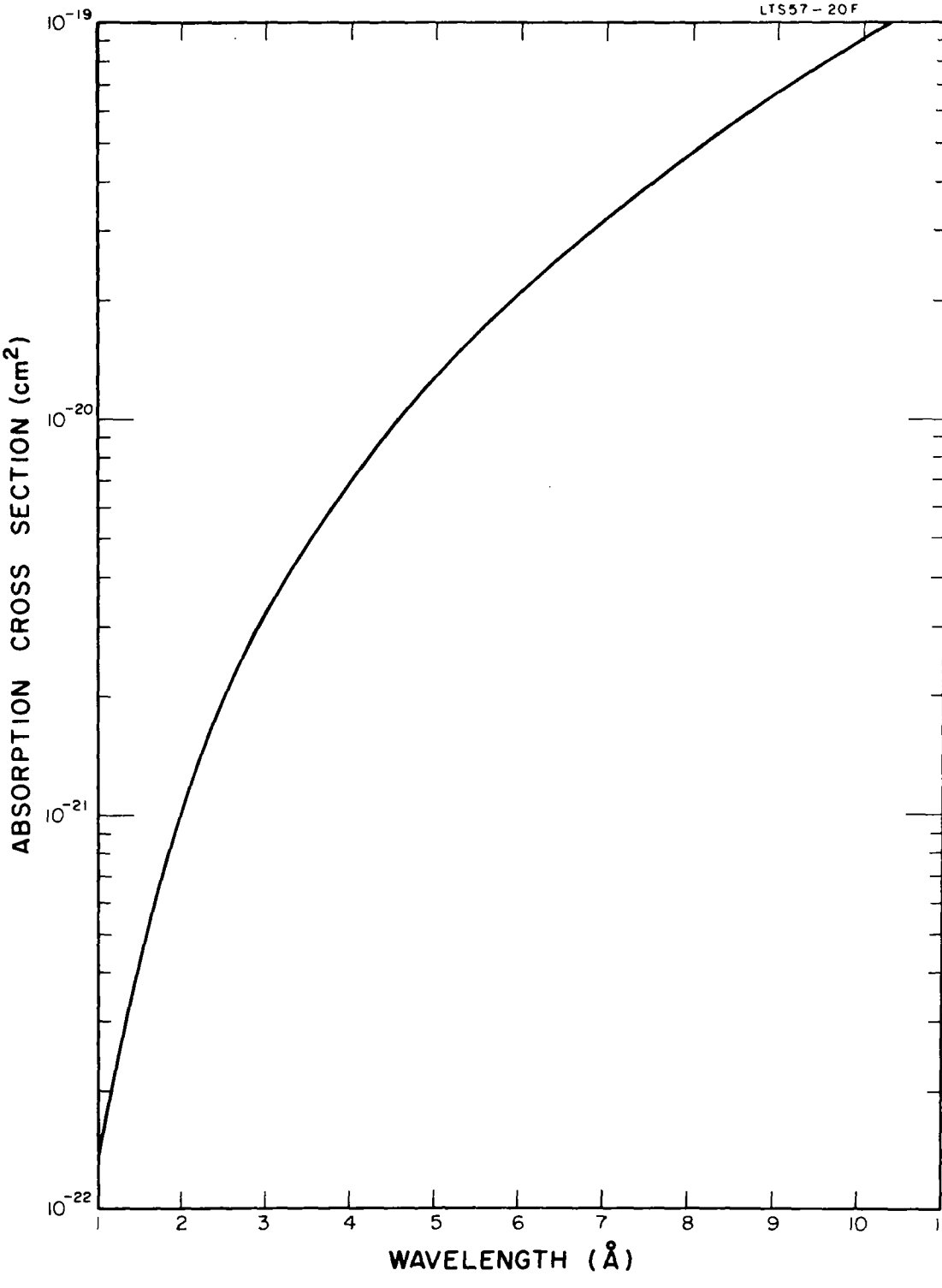

Figure 22. Absorption cross-section of air (1-10Å).[47]

considered, for example, devices generating flash discharges [60] and monochromatic isotopic radiation sources. However, it was decided that an optimum combination of all factors, namely, expense, availability and performance could be met by a soft X-ray generator designed specifically for the simulation of solar-X-rays in the ionosphere. This generator can be mounted within the simulation chamber and obviates the complexity of an external vacuum tube with appropriate transmission filters for the desired spectrum.

Atomic Oxygen

Production of atomic oxygen. Oxygen exists largely in atomic form in the ionosphere due to dissociation by the solar uv flux. As in the case of the simulation of charged particles, we must distinguish between methods of simulation depending on the neutral density of different regions of altitude.

Photodissociation. We first consider the conditions required for simulation of the atomic oxygen concentration by photodissociation.

The following processes are operative under equilibrium conditions:

(a) Photodissociation - Radiation from a Xenon lamp is a strong source of photodissociation of oxygen. The photon flux is about 10^{16} photon/cm^2/sec at 1471Å. The absorption cross section of O_2 at 1471Å is 10^{-17} cm^2. Assuming the idealized geometry of Figure 23, the rate of photodissociation is given by

$$q_p = n(h\nu)\ k(\nu)\ n(O_2)$$

where $n(h\nu)$ = photon flux in the beam
$k(\nu)$ = absorption cross section
$n(O_2)$ = concentration of oxygen molecules.

Substituting the value given above we have the atomic oxygen production rate,

$$2q_p = 2 \times 10^{16} \times 10^{-17} \times n(O_2)$$

$$= 2\ n(O_2) \times 10^{-1} \text{ atoms/cm}^3\text{/sec}$$

We calculate $2q_p$ for the following pressure range:

Pressure	$n(O_2)$	$2q_p$	Path length for reducing the incident photon flux by 1/e
			cm
10μ	3×10^{14} mol/cm^3	6×10^{13} atoms/cm^{3}sec	300
100μ	3×10^{15} mol/cm^3	6×10^{14} atoms/cm^{3}sec	30
1000μ	3×10^{16} mol/cm^3	6×10^{15} atoms/cm^{3}sec	3

(b) Diffusion - Assuming a diffusion coefficient of about 0.356 cm^2 sec^{-1} at NTP or D = 270 cm^2/sec at 1 torr, we obtain

Pressure	D
10μ	2.70×10^4 cm^2 sec^{-1}
100μ	2.70×10^3 cm^2 sec^{-1}
1000μ	2.70×10^2 cm^2 sec^{-1}

(c) Wall Recombination -

$$\frac{dn(0)}{dt} = \gamma \frac{1}{4} \bar{c}\, n(0)_{wall}$$

where γ is the recombination coefficient, and

$\bar{c}$ is the average atomic velocity

γ for pyrex: 2×10^{-5}; $\bar{c}$ for atomic oxygen at 300°K: 6.24×10^4 cm/sec.

$$\frac{dn(0)}{dt} = \frac{2 \times 10^{-5} \times 6.24 \times 10^4}{4} n(0)/cm^2/sec$$

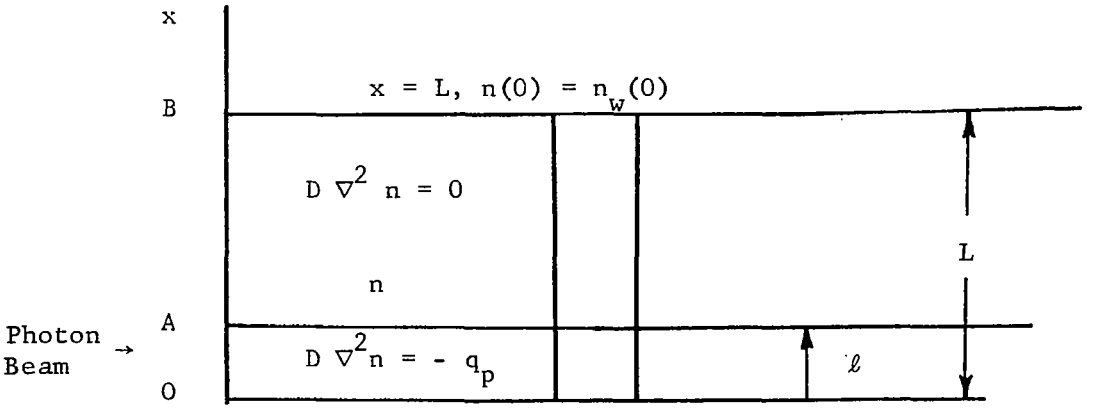

Figure 23. Idealized geometry for distribution calculation

(d) Volume Recombination - The depletion of oxygen atoms in the volume is due to the following processes:

$$O + O + O_2 \rightarrow O_2 + O_2 \quad (1)$$

$$O + O_2 + O_2 \rightarrow O_3 + O_2 \quad (2)$$

$$O + O_3 \rightarrow O_2 + O_2 \quad (3)$$

At room temperature

$$k_1 = 4 \times 10^{-33} \text{ cc}^2/\text{molecules}^2 \text{ sec}$$

$$k_2 = 4 \times 10^{-34} \text{ cc}^2/\text{molecules}^2 \text{ sec}$$

$$k_3 = 3 \times 10^{-14} \text{ cc/molecules sec}$$

where k_n is the rate coefficient for the individual reaction.

Neglecting the volume reactions, the distribution of the atomic oxygen in the region outside the beam is given by

$$D\nabla^2 n = 0$$

and in the beam region by

$$D\nabla^2 n = -2q_p$$

Assuming that the only loss of atomic oxygen is due to wall recombination, the rate of surface recombination will be equal to the rate of production; accordingly, we have

$$\frac{\gamma}{4} n_w(0) \bar{c} = 2q \times \ell$$

where $n_w(0)$ is concentration of oxygen atoms at the wall.

Assuming ℓ = 1 cm

$$n_w(0) = \frac{2q_p}{312} \times 10 \text{ atom/cm}^3$$

Pressure	$n_w(0)$ atoms/cm^3
10μ	1.9×10^{14}
100μ	1.9×10^{15}
1000μ	1.9×10^{16}

The above condition corresponds to about a 32 percent dissociation of atomic oxygen. Under diffusive equilibrium the distribution of atoms will be given by

$$n = n_w(0) + \frac{2q}{D} \ell (L - x)$$

Therefore, in the central region the concentration can be obtained from $2q/D$ and the geometry of the vessel. $2q/D$ at different pressures is given by

Pressure	$2q/D$	$n_w(0)$
10μ	2.22×10^{9}	1.9×10^{14}
100μ	2.22×10^{11}	1.9×10^{15}
1000μ	2.22×10^{13}	1.9×10^{16}

Compared with $n_w(0)$, the $2q/D$ term has no appreciable effect and, therefore, the distribution of atomic oxygen under diffusive equilibrium and surface recombination is uniform throughout the vessel, and is given by $n_w(0)$.

After primary dissociation the composition is given by

Pressure	(0)	(0_2)
10μ	2×10^{14}	2×10^{14}
100μ	2×10^{15}	2×10^{15}
1000μ	2×10^{16}	2×10^{16}

We now calculate the effect of volume recombination.

The rate of the two processes governed by k_1 and k_2 as a function of pressure is given by

Pressure	$k_1(0)^2(0_2)$	$k_2(0)(0_2)^2$	q_p
10μ	3.2×10^{10}	3.2×10^{9}	6×10^{13}
100μ	3.4×10^{13}	3.2×10^{12}	6×10^{14}
1000μ	3.2×10^{16}	3.2×10^{15}	6×10^{15}

Thus, at 1000μ the atomic oxygen will be depleted by volume reactions but at a pressure of 100μ or less volume reactions will not have an appreciable effect.

The steady state concentration of ozone at these pressures is given by

$$n(0_3) = \frac{k_2}{k_3} (0_2)^2$$

Pressure	$n(0_3)$
10μ	5×10^{8} molecules/cm^3
100μ	5×10^{10} molecules/cm^3
1000μ	5×10^{12} molecules/cm^3

which is again negligible under the above conditions.

(e) Conclusions

(1) The recombination rate at the pyrex surface is negligible compared with the rate of production. The distribution is practically uniform.

(2) The concentration of ozone is negligible.
(3) The main process for volume recombination is

$$O + O + O_2 \rightarrow O_2 + O,$$

$$k = 4 \times 10^{-33} \text{ cc}^2/\text{molecules}^2 \text{ sec}$$

(4) If the volume of the photodissociation region in the vessel is v and the total volume is V then under the following conditions the volume recombination rate is equal to rate of production:

Pressure	V/v
10μ	2×10^3
100μ	2×10^1

(5) An atomic oxygen concentration of about 10^{14} atoms/cm^3 can be obtained in a pyrex vessel at 10μ provided the ratio of the volume of the vessel to the volume of the dissociation region is less than 1000.

Thus, the atomic oxygen concentration can be simulated realistically over various portions of the D region.

It turns out that the pressure of 10 to 100μ is too high for certain simulation requirements, as for example, the calibration of mass spectrometers for atomic oxygen.

In this case, it may be possible to dilute the ambient density by producing an outflow into an additional evacuated chamber from the vessel containing the mixture of atomic and molecular oxygen produced by photodissociation. This can be achieved readily through an aperture in a pyrex or teflon disc. The resulting beam is directed into the ion source of the mass spectrometer to be calibrated. The pumping speed in the second chamber must be high enough to reduce the density of the background gas at least an order of magnitude below the density of the calibrating mixture.

Atomic beam system. Rather than by photodissociation, a beam containing about 20 percent atomic oxygen can also be produced by microwave discharge. A particle flux of $3 \times 10^{14}/cm^2/sec$ has been produced over an area of 2 cm^2 in a system built by GCA for the Goddard Space Flight Center which is described in GCA Final Report, Contract No. NAS5-3251, September 1964 (Figure 24).

This system is considerably more complex than the proposed photodissociation chamber, but it facilitates the simulation of atomic oxygen under conditions which apply to higher altitudes. The relevant references to this method of atomic oxygen production are given in the above mentioned GCA report.

Photoionization of atomic oxygen. The photoionization cross section of atomic oxygen has been computed by Bates and Seaton [61], Dalgarno and Parkinson [62] and most recently by Dalgarno, et al.[63] who listed cross sections appropriate to some important solar lines with wavelengths less than 900Å. Recently this laboratory [64] has produced the first measurements of the total absorption cross section of atomic oxygen within the wavelength range 910 to 504Å. The various cross sections are listed in Table 21.

Conclusions

A survey of existing methods of simulating the various parameters of interest has shown that simultaneous simulation is possible for several restricted altitude ranges of the D and E regions.

The literature survey was supplemented by various experimental and theoretical studies which have greatly extended the scope and feasibility of simultaneous ionospheric simulation.

(1) Simulation of the atmospheric charged particle density under static, thermally realistic conditions can be achieved by photoionization provided that a uv intensity level considerably greater than the corresponding solar intensity can be tolerated. This method of simulation is restricted to the lower D region.

(2) Simulation of atmospheric charged particle density under dynamic conditions can be performed with a low energy (~ 10 eV) space-charge neutral plasma device. In this case, simultaneous simulation with the solar X-ray and uv spectrum is possible. Ambient conditions for this type of simulation correspond to the higher D region and the whole of the E region.

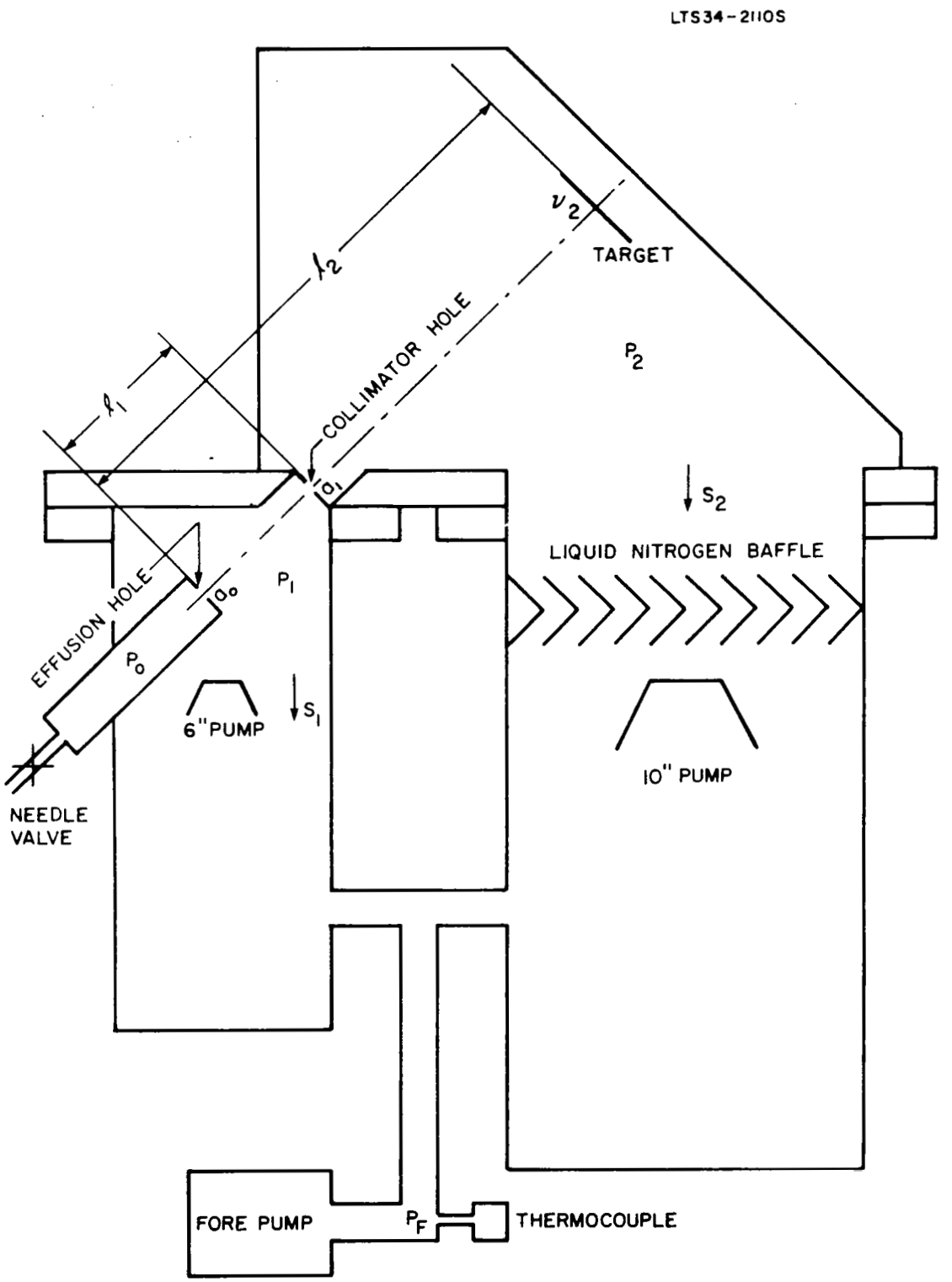

Figure 24. Two-aperture system.

TABLE 21

ABSORPTION CROSS SECTIONS OF ATOMIC OXIGEN,
λ = 504 to 910Å

λ(Å)	$\sigma(0)(cm^2 x10^{-18})$	λ(Å)	$\sigma(0)(cm^2 x10^{-18})$
508.434 A III 508.595 A III	13.3	725.542 A II	16.7
		735.89 Ne I	14.3
551.371 A VI	13.2		
		743.70 Ne I	7.6
584.331 He I	11.9		
		758.677 O V	
585.754 A VII	12.3	759.440 O V	
		760.229 O V	8.3
624.617 O IV		760.445 O V	
625.130 O IV	13.0	761.130 O V	
625.852 O IV		762.001 O V	
636.818 A III 637.282 A III	13.7	760.439 A IV	7.9
		774.522 O V	7.6
683.278 A IV	11.8		
		779.821 O IV	11.1
684.996 N III		779.905 O IV	
685.513 N III	17.3		
685.816 N III		822.159 A V	6.0
686.335 N III			
		832.754 O II	
699.408 A IV	12.7	832.927 O III	
700.277 A IV		833.326 O II	5.3
		833.742 O III	
702.332 O III		834.462 O II	
702.822 O III 702.899 O III	13.0	850.602 A IV	5.0
703.850 O III			
		901.168 A IV	4.7
715.599 A V 715.645 A V	12.2	901.804 A IV	

(3) Simulation of the solar X-ray and uv spectrum can be performed independently of and simultaneously with the simulation of all other atmospheric parameters, provided a simulation chamber of appropriate dimensions is chosen, which will probably not exceed 1 cubic meter.

(4) As in the case of atmospheric charged particle density, simulation of the atomic oxygen concentration can be performed under static or dynamic conditions. In the static case, simulation is restricted to the D region and the effective volume will be restricted to a few liters. Atomic oxygen will be produced by photodissociation in a concentration of about 30 percent.

Alternatively, the atomic oxygen concentration can be simulated in a chamber whose ambient pressure corresponds to the E region. This is accomplished by means of a directed beam of oxygen which contains 20 percent atomic and 80 percent molecular oxygen. Simulation of this parameter cannot be readily combined with charged particle production, but permits simultaneous simulation of the solar X-ray and uv spectrum.

IV. DETECTION OF RADIATION

Necessary prerequisites for the simulation of the D and E region are the detection of radiation in the vacuum ultraviolet and X-ray regions and the calibration of the detectors. Within the past fifteen years, many new vacuum ultraviolet light sources have been developed. Concurrently, these advances have stimulated the development of new photoelectric detection methods. Monochromatic detectors have not been developed; however, in some spectral regions, monochromatic detection can be approximated. Such narrow band detectors when combined with selective thin-film filters, window materials, and judicious use of grating monochromators have advanced the state-of-the-art. Progress has also been made in the field of absolute intensity measurements in the vacuum ultraviolet. Generally, the X-ray spectrum has been extensively studied and many pertinent properties are known. However, experimental methods for the measurement of the absolute intensity of the soft X-ray flux pertinent to simulation techniques are practically nonexistent. In the following sections, the various types of detectors developed for extreme ultraviolet and, where appropriate, soft X-ray regions, together with the latest techniques for their calibration, will be discussed.

Ultraviolet Spectrum

The detection of radiation below 2000Å is discussed in terms of: (1) photoelectric effect, (2) photoionization of gases, and (3) fluorescence. Blackening of photographic plates is also an appropriate consideration; however it will not be discussed further since it is the least versatile of the four.

Photoelectric Effect. The "surface" photoelectric effect is small compared to the volume effect. The volume effect was unknown until the studies of Kenty,[65] in 1933, on several metals. Very little quantitative data had been obtained until the work of Hinteregger, Watanabe and Weissler [66,67] who twenty years later measured the yield of a metal down to 500Å. These authors obtained yields (electrons released per incident photon) of the order of 10 to 15 percent. The lack of suitable light sources and means for determining the absolute number of incident photons prevented further work to shorter wavelengths. Brunet, et al. [68] have made measurements below 500Å, but their results are relative. Using rare-gas ion-chambers, present studies at the GCA Corporation are measuring yields down to 200Å on an absolute basis.

The selectivity of the photoelectric effect is effective in discriminating radiation above and below 1200Å. Figure 25 shows a typical curve for the absolute photoelectric efficiency as a function of wavelength

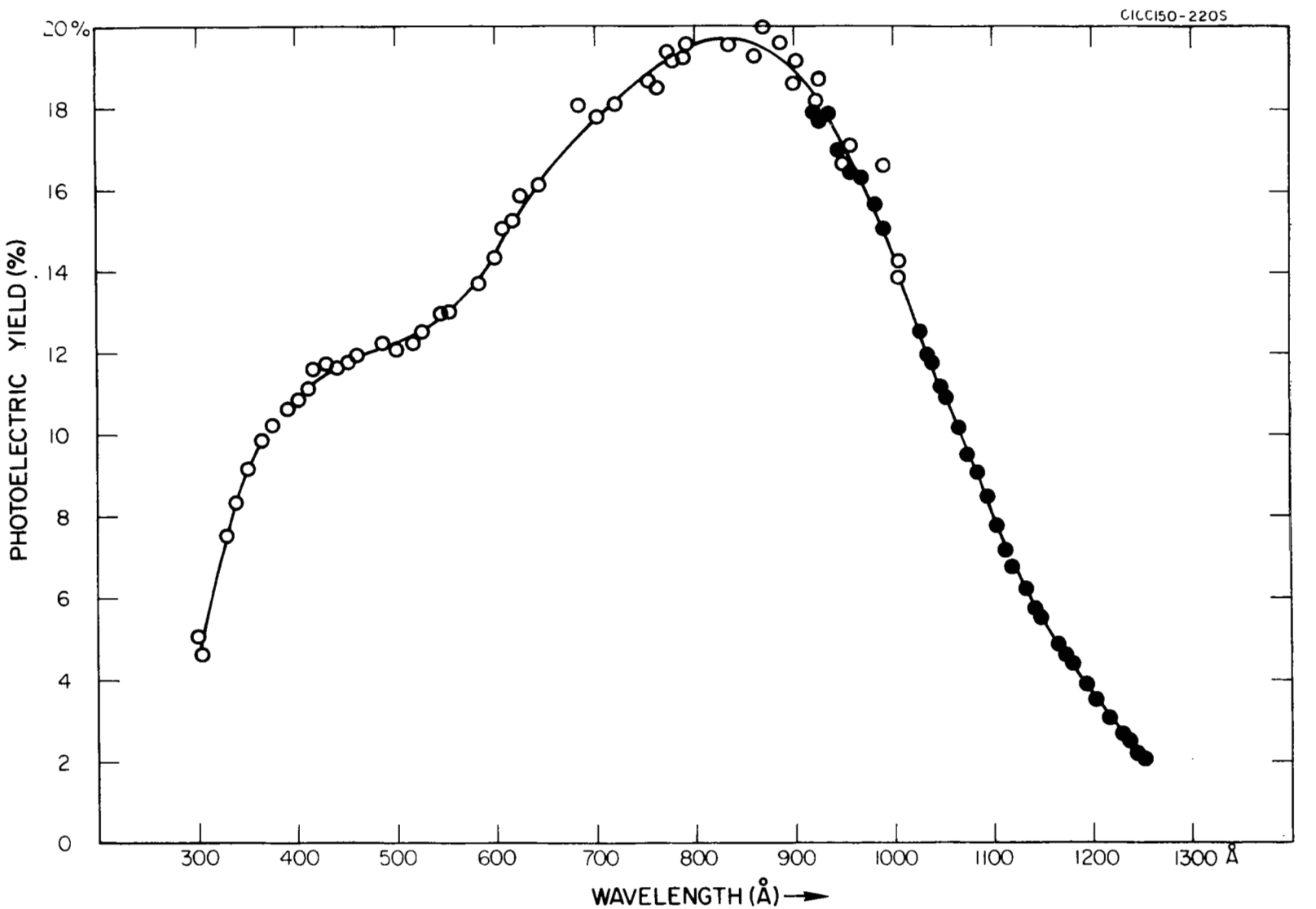

Figure 25. Absolute photoelectric efficiency.

of an aluminum cathode [69]. This curve is typical of many metals indicating that these cathodes are particularly suitable for use between 200 and 1200Å and can discriminate against both the X-rays and longer ultraviolet and visible light. The use of more exotic cathodes such as thin layers of lithium fluoride and strontium fluoride on the other hand is expected to give higher yields in the 100 to 200Å region.

Photoionization of Gases. Experiments on photoionization of gases have been conducted since the turn of the century. In an original experiment, Lenard [70] inferred that ultraviolet light from air ionized by a spark was capable of discharging an electroscope. However, subsequent measurements of ion mobilitites indicated that the ions, particularly those produced in unfiltered air, were relatively large particles or nuclei and not molecular ions. In order to eliminate large particles, Hughes [71] and others used carefully filtered air; nevertheless, they found that ultraviolet radiation transmitted by fluorite (transmission limit about 1240Å) was capable of producing ions of molecular size but radiation transmitted by quartz was not effective. Since the ionization potentials of the constituents of air correspond to wavelengths much lower than 1240Å, the observed ions could not have been produced by direct photoionization, but possibly by a two step process, or by ionization of some impurities such as mercury vapor, or by accelerated photoelectrons. It is difficult to interpret the results of these early experiments, since undispersed radiation was used and quantum yields were not measured. Hughes and DuBridge [72] describe these experiments and explain "that the state of our knowledge regarding the ionization of these gases is extremely unsatisfactory".

Several early investigators studied the photoionization of the alkali vapors, taking advantage of the fact that these vapors can be ionized in the region 2000 to 3200Å where quartz optics could be used. Experimental techniques, in particular, energy measurements, improved in studies utilizing monochromatic radiation. Thus, many quantitative data were obtained, particularly by Mohler and co-workers [73] and by Lawrence and Edlefsen, [74]. The study of photoionization cross section of alkali vapors has been reviewed and summarized by several writers [72,75,76].

Studies on the photoionization of gases almost ceased after 1930. It was not until 1950 that the first thermocouple measurement of dispersed vacuum ultraviolet radiation by Packer and Lock [77] and its application to the absolute quantum yield of $CaSO_4$:Mn phosphor by Watanabe [78] confirmed the feasibility of photoionization and photoelectric studies in the spectral region below 2000Å with dispersed radiation obtained from a vacuum monochromator developed by Tousey, et al. [79]. In 1953, Watanabe, Marmo and Inn, [80] and Wainfan, Walker and Weissler [81] reported on photoionization measurements in the vacuum ultraviolet region. The former group showed that accurate determination of the ionization potential is possible by utilizing monochromatic light of 0.01 ev bandwidth, and ionization potentials for about 80 molecules have been reported [82,82]. Later, Sakai, Little, and Watanabe [82] reduced the bandwidth to 0.001 ev.

More recently, GCA Corporation has completed the measurement of the yields of some 20 molecules in a study to find suitable gases for narrow band ionization chambers. To produce narrow spectral band sensitivities it is necessary to select the appropriate choice of window material and gas filling. The short wavelength cut-off is determined by the window material while the long wavelength cut-off is determined by the ionization potential of the gas. Table 22 indicates two possible narrow band ion chambers that could be used for the detection of Lyman α (1215.7Å) radiation.

TABLE 22

ION CHAMBERS AND MEASUREMENTS

Gas Filling	Chemical Formula	Window Material	Spectral Response (Å)	QE* (%)
Carbon Disulfide	CS_2	LiF	1050-1240	50-60
Nitric Oxide	NO	LiF	1050-1350	10-50

*Based on a value of 81 percent for NO at Lyman alpha (1215.7Å)

Fluorescence. The technique for extending the sensitivity range of standard photomultipliers down to the soft X-ray region is to coat the outer glass envelope with a material which will fluoresce when illuminated by uv radiation. Recently, many materials have been studied [83]. Anthracene, stilbene, sodium salicylate, oil, coronene, and a host of other materials will fluoresce. However, the most generally useful material is sodium salicylate since it has a high quantum efficiency and is reported to have a sensitivity which is independent of wavelength [84]. Recent measurements at the GCA Corporation indicate that this may be true with certain reservations [85,86].

Absolute Intensity Measurements. Certain specific parameters require special attention in any study concerned with the measurement of absolute photon fluxes greater than 100Å. These parameters include photon efficiency, wavelength cut-off for certain interactions or phenomena, flux threshold requirements and amenability to wavelength resolution. A discussion of these parameters follows.

Photon efficiency. Some indication of photon efficiencies has already been given in the description of the photoelectric and photoionization methods, however, photon efficiency is specifically related to the calibration of absolute intensities.

Until recently the absolute intensity of radiation less than 1000Å was measured with a calibrated thermopile or similar heat sensitive device. The problems involved in obtaining accurate results with a thermopile below 1000Å are many and to this date no absolute calibrations have been made with them for any narrow spectral region below 500Å. This problem however, has been alleviated by the development of the rare gas ionization chamber method [85]. Although the technique employed here has appeared in the open literature [85] and is accepted as a standard, for completeness a brief description of the system is presented below.

Referring to Figure 26 for an analysis of the single ion chamber, we define I_o as the light intensity at the exit slit of the monochromator and I as the transmitted intensity at the end of the ion chamber. Then, the photoionization yield, γ, is given by

$$\gamma = \frac{\text{ions formed/sec}}{\text{photons absorbed/sec}}$$

$$= \frac{i/e}{I_o - I}$$

$$= \frac{i/e}{I_o(1-I/I_o)}$$

therefore,

$$I_o\gamma = \frac{i/e}{(1-I/I_o)} \tag{28}$$

For the rare gases $\gamma = 1$, hence, I_o can be found.

The ratio I/I_o is measured by the detector which must lie exactly at the end of the ion chamber. This ratio is independent of absolute intensities and any detector which has a linear response with respect to intensity may be used. This method requires that all the ions formed from the exit slit to the detector be collected and counted. To achieve this, it is necessary to connect the exit slit electrically to the positive repeller plate. The ion chamber would then have a field distribution as shown in Figure 26 and all ions formed within the ion chamber system would be collected. The major advantage of this system is that no measurement of an absorption coefficient is made which must obey Beer's law. Actually, I_o is independent of the pressure used and in the limit when $I/I_o \rightarrow 0$

$$I_o = \frac{1}{\gamma}\ i/e. \tag{29}$$

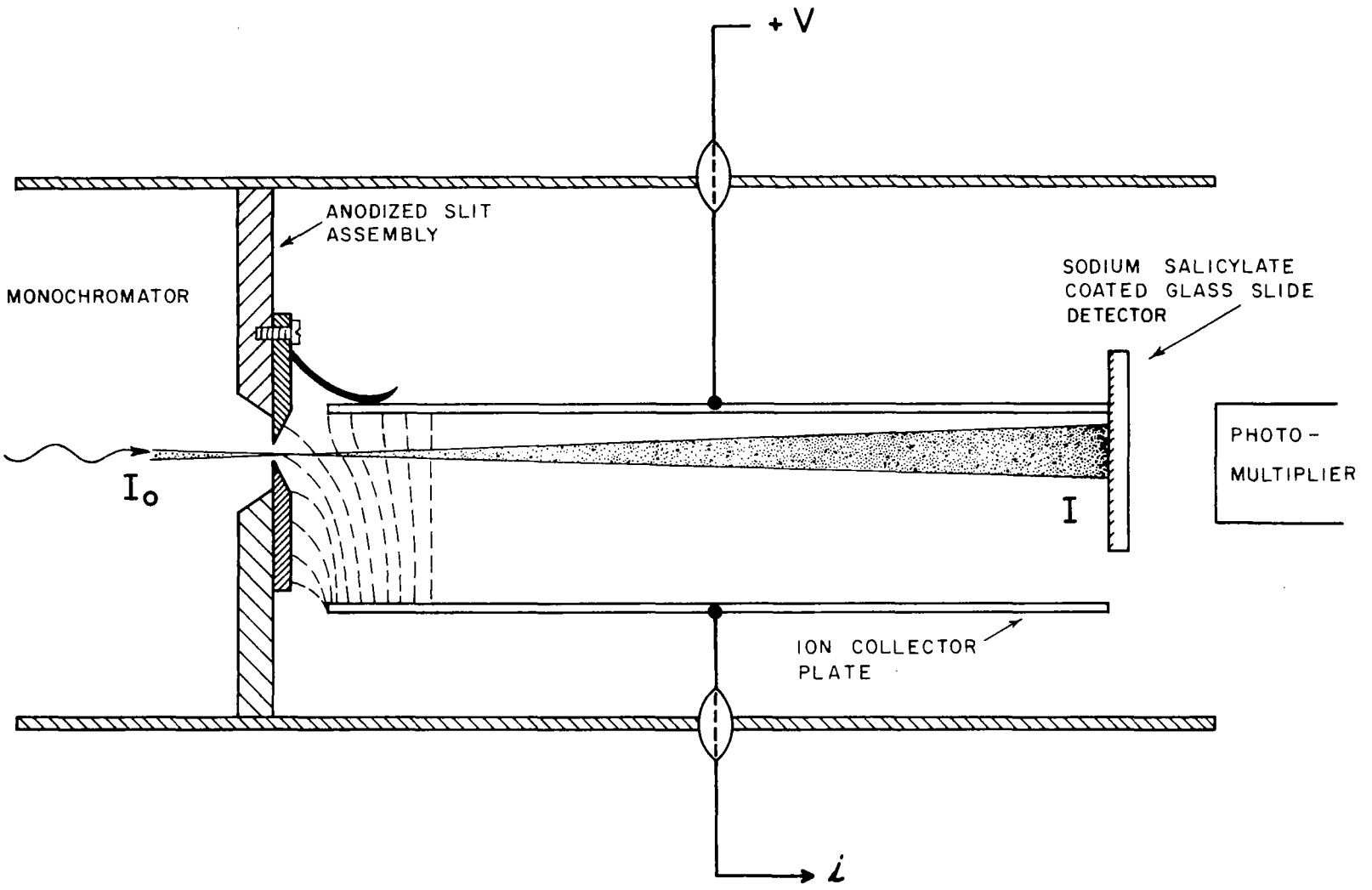

Figure 26. The single ion chamber. I_o is the flux passing through the exit slit of the monochromator while I is the flux at the detector. The dashed lines indicate typical electric field lines.

This is the condition for total absorption of the radiation and for $\gamma = 1$ the number of photons/sec passing into the ion chamber is just equal to the number of ions produced within the ion chamber. Using the rare gases, absolute intensities can be measured from 1022Å (the ionization potential of xenon) down into the soft X-ray region.

Wavelength cutoff. No sharp wavelength cutoff is expected for fluorescent detectors; however, some discrimination is shown by the photoelectric effect and very sharp onsets are given by the photoionization of the gas.

Wavelength discrimination can also be achieved through the use of thin metallic filters. Self-supporting films of this nature are not very rugged; however, when used in conjunction with the appropriate fluorescent material they form a rugged and simple narrow band detector. Figure 27 shows the transmittance of a typical GCA Corporation detector using an indium filter which is applicable for this program.

Recently, data have been accumulating on the transmissivity of thin metal films in the spectral region below 1500Å [87 thru 95]. Such information has had the practical value of providing filters in a region where none previously existed. Further, the accumulation of transmission data is of value to the theoretical understanding of metals.

The energy range of extreme ultraviolet radiation lies approximately between 6 and 60 ev. These energies are comparable with the characteristic energy losses experienced by fast electrons in passing through thin metal films. Some of these energy losses can be explained by the collective nature of the free electrons in the metal films. The theory of the collective free electron model, as developed by Bohm and Pines [96], predicts a collective oscillation of the free electrons at a frequency given by

$$\nu_p = \left(\frac{n\ e^2}{\pi\ m}\right)^{\frac{1}{2}},$$

where ν_p is the plasma frequency, n the density of the valence electrons, m the electron mass, and e the electronic charge. The fast electrons, as they penetrate the metal, lose an amount of energy equal to $h\nu_p$ in exciting this resonance oscillation. This model also views the electron plasma as being able to support an electromagnetic wave at frequencies greater than ν_p. At these frequencies the metal is predicted to change from a reflecting to a transmitting medium. The plasma frequency is the same as that given by the individual free electron model where the long range Coulomb interactions are neglected. Many metals studied thus far do exhibit a region of relative transparency in the vicinity of ν_p.

No optical data previously existed for carbon; however, a large characteristic electron energy loss has been observed at 22 ev by several observers [16,22,97]. The free electron plasma frequency is calculated to be 23.6ev (526Å) if the density of carbon is taken to be 2 gm/cc and if the number of free electrons per atom is taken as 4.

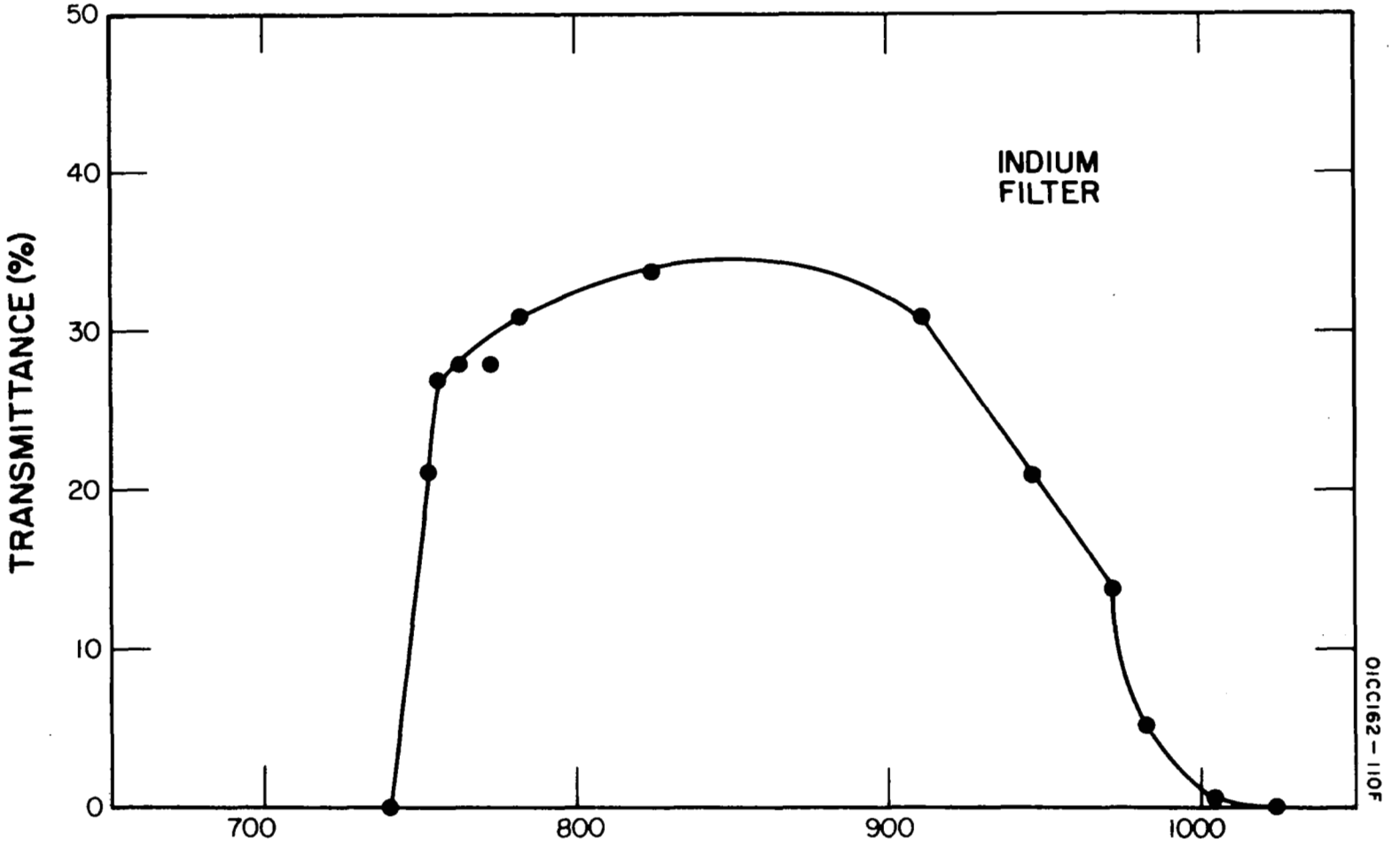

Figure 27. Typical response of a detector using an indium filter.

Recent experimental results by Samson and Cairns [97] for carbon are shown in Figure 28 for a thin film approximately 270Å thick. The carbon film was evaporated in vacuum onto a substrate and subsequently floated off in distilled water and mounted on a wire mesh.

The transmittance decreases continuously from 41 percent at 2000Å to 1 percent at 1000Å . Between 900Å and 600Å carbon is very highly absorbing. In the vicinity of the free-electron plasma frequency (526Å)the transmittance again starts to increase reaching 56 percent at 209Å. Presumably, the transmittance will reach a maximum at shorter wavelengths and fall to zero at 43.6Å, the carbon K absorption edge. This is represented by the dashed curve in Figure 28.

The transmittance at 304Å is 30 percent while at 584Å it is about 1 percent, a discrimination of 30:1. Increasing the thickness by a factor of 2 provides a discrimination of 900:1 with a transmittance of 9 percent at 304Å.

For the detector system to be selective (with a 100Å maximum bandpass width) use can be made of the selective nature of the primary process, filters, and/or a diffraction grating.

Flux threshold requirement. The flux threshold for detecting radiation between 100 and 1250Å depends on the type of detector used. The efficiencies of the photon conversion for the three primary processes are approximately as follows:

Photoionization	100 percent
Photoelectric	10 percent
Fluorescence	20 percent

Although photoionization looks most promising, the simple geometry of the detector requires a small aperture to prevent a rapid loss of gas; thus its sensitivity is reduced slightly. The photoelectric process on the other hand while only ~ 10 percent efficient in the primary stage can be used in conjunction with an electron mutiplier with gains up to one million. The fluorescence technique while using the advantages of a photomultiplier suffers from being sensitive to scattered visible light.

Wavelength Resolution. The most direct and precise method for dispersing radiation into any desirable bandpass is the use of a concave diffraction grating monochromator. A very compact monchromator can supply a 100Å bandpass. As a single instrument, however, to cover the range 100 to 1000Å and Lyman α (1215.7Å), a simple grating instrument would produce overlapping higher order spectra. The need then arise for filters as described above, and/or the use of a selective primary process.

The use of a gas-filled ion chamber provides well-defined onset levels for detection and well-defined wavelength intervals. For instance, a helium-filled ion chamber or Geiger counter will respond only to radiation of wavelengths shorter than 504.2Å, while an argon-filled counter will operate from 786.7Å.

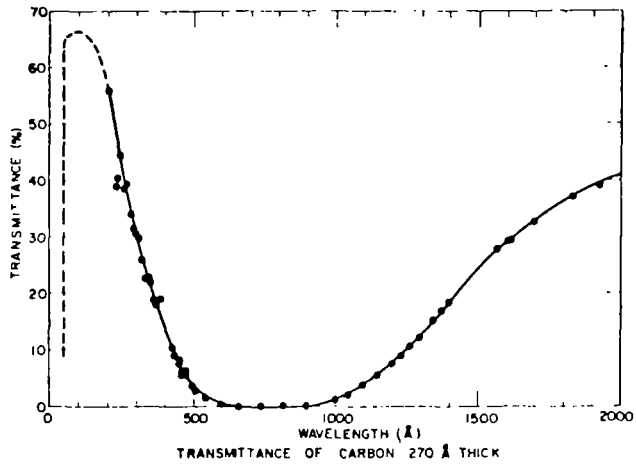

Figure 28. Transmittance of carbon 270Å thick. The dashed curve represents the suggested transmittance below 200Å.

Application. In the previous paragraphs, the detection of vacuum ultraviolet radiation as well as the calibration of these detectors has been discussed in general terms. For the simulation of the D and E regions, it has been shown that the following wavelengths namely Lyman α (1215.7Å), Lyman β (1025.7Å), C III (977.0Å), Lyman ϵ (937.8Å), He II (584.5Å) and He I (303.8Å) are pertinent for simulation. The choice of detectors will depend on whether simulation is performed simultaneously or separately. Ideally, simultaneous simulation is desired; however, this is not without consequence. Depending on the level of sophistication, the various options of simulation are shown in Table 23 and the suggested modes of simulation are noted in Tables 24 and 25.

Some comments on the various detectors may well be in order. Several types of detectors can be used to detect the pertinent wavelengths. First and foremost, the standard detector (100 to 2000Å) for case 1 (Table 24) is the conventional photomultiplier which has been coated with sodium salicylate. This material fluoresces at about 4100Å. Since it does not behave as a narrow band detector, the simulated radiation must be monochromatic, i.e., each wavelength must be duplicated separately. One of the inherent problems of this detector is its response to scattered visible light. It can be avoided by using a multiplier with a pure metal photocathode such as tungsten. Since tungsten has a photoelectric onset of 1400Å, its useful range is restricted to shorter wavelengths. This removes the problem of scattered visible light and allows all radiation below 1400Å to be monitored. Under these conditions a monochromator is essential.

For case 3 (Table 25) where the radiation is not dispersed monochromatically, other types of photon detectors are utilized. For the detection of Lyman α (1215.7Å), the most appropriate detector is the photoionization counter filled with nitric oxide. This gas-filled counter is particularly adaptable for Lyman α (1215.7Å) and is an accepted standard for measuring absolute photon fluxes in the 1050 to 1350Å region. A typical efficiency of a nitric oxide ion chamber at Lyman α with a lithium fluoride window is approximately 50 percent, i.e., 50 percent of the incident photons are utilized to form ions.

For all other wavelengths, the method of photoemission of metals for detection and calibration offers several advantages over other techniques. The designated construction can be accomplished easily. Since the detector will be located in the differential pumping assembly outside the simulation chamber, it can be moved in and out of the light beam with a minimum of difficulty. Such detectors cannot only monitor the vuv radiation in a routine manner, they also serve as secondary standards when calibration is necessary. It is suggested, however, that the various platinum detectors be calibrated against the photoionization of rare gases technique initially prior to mounting in the chamber.

TABLE 23

METHODS OF SIMULATION

Method of Simulation	Light Sources and Dispersing Devices	Comments
Case 1 - Each line is simulated separately.	One light source and one standard vacuum ultraviolet monochromator.	Most applicable and least expensive.
Case 2 - All lines are simulated simultaneously.	Six light sources and one standard vacuum ultraviolet ½-meter and five specially constructed monochrometers.	Most expensive method.
Case 3 - All lines are simulated simultaneously.	Six light sources, one standard vacuum ultraviolet ½-meter monochromator, thin film and gas filters.	A compromise.

TABLE 24

MODES OF SIMULATION

Lines	Depth at Unit Optical Thickness	Method of Detection	CASE 1 and CASE 2 Calibration Methods	Method of Simulation
1215.7Å	75 km	Photomultiplier with sodium salicylate coating	Standard ion chamber with nitric oxide	Hydrogen hot filament discharge lamp and monochromator
1025.7Å	108 km	Photomultiplier with sodium salicylate coating	Standard ion chamber with oxygen and differential pumping	Hydrogen hot filament discharge lamp and monochromator
977.0Å	120 km	Photomultiplier with sodium salicylate coating	Photoionization of rare gases	Mixture of carbon dioxide and oxygen, hot filament discharge lamp and monochromator
937.8Å	136 km	Photomultiplier with sodium salicylate coating	Photoionization of rare gases	Hydrogen hot filament discharge lamp and monochromator
584.5Å	≈ 200 km	Photomultiplier with sodium salicylate coating	Photoionization of rare gases	Helium hot filament discharge lamp and monochromator
303.8Å	182 km	Photomultiplier with sodium salicylate coating	Photoionization of rare gases	Helium spark discharge lamp and monochromator

TABLE 25

MODE OF SIMULATION

Lines	Depth at Unit Optical Thickness	Method of Detection	CASE 3 Calibration Methods	Method of Simulation
1215.7Å	75 km	Photoionization counter or photoemission from platinum	Standard ion chamber with NO or photoemission from platinum	Hydrogen helium hot filament discharge lamp with LiF window
1025.7Å	108 km	Photoemission from platinum	Photoemission from platinum with nitrogen gas filter	Hydrogen hot filament discharge and lamp, thin film filter
977.0Å	120 km	Photoemission from platinum	Photoemission from platinum	Carbon dioxide-oxygen (trace) hot filament discharge lamp, monochromator
937.8Å	136 km	Photoemission from platinum	Photoemission from platinum	Hydrogen hot filament discharge lamp with thin film filter
584.5Å	≈200 km	Photoemission from platinum	Photoemission from platinum	Helium hot filament discharge lamp
303.8Å	182 km	Photoemission from platinum	Photoemission from platinum	Helium spark discharge lamp

Difficulties arise if undispersed radiation from a hydrogen discharge and a thin-film filter are used for simulating Lyman β (1025.7Å) and Lyman ϵ (937.8Å). Unwanted contributions of almost equal intensity due Lyman γ (972.5Å) and Lyman δ (949.7Å), as well as the underlying continuum will be transmitted also. For calibration purposes, however, the Lyman β (1025.7Å) line can be isolated by means of a nitrogen gas filter. The next section shows in some detail the upper limit of detectability of the various detectors for actual simulated densities in the space chamber. The predicted performance is tabulated in Table 26.

The parameters in Table 26 were determined by assuming a simulation chamber of 1-meter diameter. The target is considered to be in the center of the chamber 50 cm from the light source. As a maximized condition for detection, the detector (ion chamber, photomultiplier, Geiger counter) is assumed to be 100 cm from and directly opposite the light source. A half-meter monochromator is considered for the calculations of reduced flux at the target, according to the following geometry:

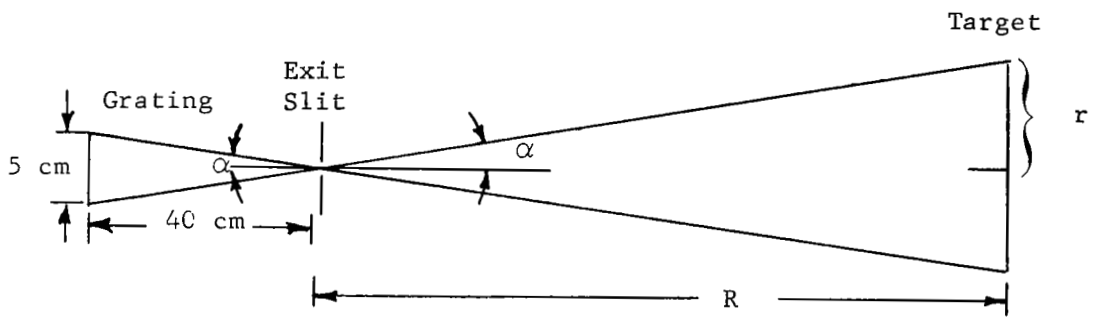

$\tan \alpha = \frac{2.5}{40} = .062$ $\quad r = R \tan \alpha$ $\quad A = \pi r^2$ $\quad I_T = \frac{I_M}{A}$; $\quad I_M$ = monochromator intensity, I_T = intensity at target

for 50 cm, reduction factor is $\frac{1}{30.2}$

for 100 cm, reduction factor is $\frac{1}{120}$

For an undispersed source, the reduction factor is

$\frac{I_u}{4\pi R^2} = I_T$ $\quad I_u$ = undispersed intensity, R = distance from source

TABLE 26

IONOSPHERIC SIMULATION OF STRONG SOLAR EUV EMISSION LINES
(1-Meter Diameter Chamber)

(1)	(2)	(3)	(4)	(5)	(6)	(7)	(8)	(9)	(10)
Identification	λ (Å)	Extinction Cross Section (megabarn)			Effective σ_{air} at 120 km**	Maximum Intensity of Source (photons/sec)		Photon Flux at 50 cm	
		N_2	O_2	O	(megabarns)	Monochromatic	Undispersed	Monochromatic	Undispersed
H Lyman α	1215.7	0	0.01	0	0.002	10^{10}	10^{16}	3×10^{8}	3×10^{11}
H Lyman β	1025.7	0.001	1.52	0	0.33	10^{10}	10^{13}	3×10^{8}	3×10^{8}
C III	977.0	0.082	3.98	0	0.82	10^{10}	--	3×10^{8}	---
*H Lyman ϵ	937.8	*	*	0	2.83	10^{8}	10^{11}	3×10^{6}	3×10^{6}
He I	584.5	23.1	23.2	7.6	20.3	10^{10}	10^{13}	3×10^{8}	3×10^{8}
He II	303.8	12.1	16.6	8.3	11.9	10^{7}	10^{10}	3×10^{5}	3×10^{5}

*Effective cross section for air derived from Watanabe and Hinteregger transmission data (reference [22]). All data for H Lyman ϵ are estimates.

**Effective σ_{air} changes with altitude above 120 km owing to the variation in mixing ratios.

TABLE 26 (continued)

(1)	(11)	(12)	(13)	(14)	(15)	(16)	(17)	(18)	(19)	(20)†
Identification	Photon Flux at 100 cm		Highest Altitude Capable of Simulation (km)	Lowest Altitude Capable of Simulation (km)			Lowest Altitude of Interest (km)	Max. Number Density at Lowest Alt.	Altitude at $\frac{I}{I_o} = 1/e$ (km)	Flux Outside Atmosphere (photons cm^2 sec^1)
	Monochromatic	Undispersed		Ion Chamber Threshold 10^7	Photomultiplier Threshold 10^5	Geiger Counter Threshold 10^2				
H Lyman α	$8x10^7$	$8x10^{10}$	>250	< 50	< 50	< 50	55(D)	1.2(16)	75	3.1(11)
H Lyman β	$8x10^7$	$8x10^7$	102	< 90	< 90	< 90	90(E)	6.6(13)	108	2.5(9)
C III	$8x10^7$	--	104	< 90	< 90	< 90	90(E)	6.6(13)	120	4.0(9)
H Lyman ϵ	$8x10^5$	$8x10^5$	115	--	< 90	< 90	90(E)	6.6(13)	136	2.4(8)
He I	$8x10^7$	$8x10^7$	184	< 90	< 90	< 90	90(E)	6.6(13)	≈200	1.6(9)
He II	$8x10^4$	$8x10^4$	124	--	--	< 90	90(E)	6.6(13)	182	3.8(9)

†Solar flux values from Schultz, E. D. and Holland, A.C., [24].

for 50 cm, reduction factor is $\frac{1}{3.12} \times 10^{-4}$

for 100 cm, reduction factor is $\frac{1}{1.26} \times 10^{-5}$

The maximum source intensity for monochromator and undispersed sources is listed for the various wavelengths in columns (7) and (8). For the monochromatic sources, the value quoted is the total number of photons emitted at the exit slit per second. In columns (9-12) the highest attainable flux at distances of 50 cm and 100 cm is tabulated. The CIII line can be generated as an isolated line only by using a monochromator.

In the model atmosphere considered for the transmission calculations, molecular nitrogen and oxygen and atomic oxygen are the only constituents included. All minor consitituents are neglected owing to their relatively significant absorption. With the exception of the H Lyman ϵ line, the total absorption cross sections for N_2, O_2 and O are from Samson and Cairns [16]. An effective cross section for N_2 O_2 at the H Lyman ϵ line was derived from the transmission data presented by Watanabe and Hinteregger [22]. Effective cross sections for air, based on mixing ratios at 120 km, appear in columns (3-6).

The model atmosphere used is a combination of the U. S. Standard Atmosphere (1962) and a recent theoretical contribution by Jacchia [98]. Jacchia has computed atmospheric density and composition models for various exospheric temperatures from a fixed set of boundary conditions at 120 km. The Jacchia model chosen is that in which the exospheric temperature agrees with the corresponding U.S. Standard Atmosphere value. The Standard Atmosphere depicts idealized middle-latitude year round mean conditions for solar activity between average and maximum. It is recognized that the transmission parameters in Table 24 will vary appreciably with the solar cycle.

Whether the solar emission lines of interest can be simulated for the appropriate altitudes depends on a number of considerations. First, the transmission data must be known accurately. Accordingly, new data were generated in the light of a more recent model atmosphere and absorption cross sections. Second, the capability of simulating these lines at the specified intensities and atmospheric densities corresponding to the D and E regions depends critically on the dimensions of the simulation chamber. The values quoted in Table 24 pertain only to the chamber assumed.

The altitude ranges capable of simulation are given in columns (13-16). This information implies that within these bounds atmospheric density, emission line intensity and detection can be simultaneously achieved.

Columns (17,18) predict that only the H Lyman α line penetrates to the D region (lower boundary 55 km); all other lines contribute only to the E region (lower boundary 90 km). In all cases the lines can be simulated to the lowest appropriate boundary. However, under the assumed maximum conditions, an ion

chamber cannot be used owing to a high detection threshold for the H Lyman ϵ line, and for the same reasons, only a Geiger counter is capable of detecting the He II line. Relocation of target and/or detector can remove these restrictions.

Column (13) identifies the highest corresponding altitude capable of simulation. This condition results from the line intensity limit at the given distance from the source.

The calculations were performed as follows:

In general $I(\lambda) = I_o \exp\{-\sigma(\lambda)\, nL\}$

For a gas mixture $I(\lambda) = I_o \exp\left\{-L\left(\sum_i \sigma_i(\lambda)\, n_i\right)\right\}$

I=laboratory intensity
σ= absorption cross section
n=particle density per cc
L=path length

For known I_o (intensity at target) and I (threshold limit of detector) a number density limit can be computed which corresponds to the lowest altitude capable of simultion.

Transmission through an atmosphere is calculated as follows:

In general $\Phi(\lambda,h) = \Phi_o(\lambda) \exp\left\{-\sigma(\lambda) \int_h^\infty n(h)\, dh\right\}$

Φ = solar flux
Φ_o = flux outside atmosphere

For a mixed atmosphere $\Phi(\lambda,h) = \Phi_o(\lambda) \exp\left\{-\left(\sum_i \sigma_i(\lambda) \int_h^\infty n_i(h)\, dh_i\right)\right\}$

Over a limited altitude region, it may be assumed that

$$\Delta N_i = \int_h^{h+\Delta h} n_i(h)\, dh_i \simeq n_i(h)\, \Delta H_i$$

where $\Delta H = \frac{RT}{mg}\Big|_h^{h+\Delta h}$

By considering individual scale heights varying with altitude, taken in 10 km steps, a close approximation to the particle count per cm^2 column for constituent i, is

$$N_i(h) \simeq (n_{h1_i} - n_{h2_i})\, H_{1_i} + (n_{h2_i} - n_{h3_i})\, H_{2_i} + \cdots n_{hM_i} H_{M_i}$$

where $hM > h(M-1) \cdots > h2 > h1$

Then $\Phi(\lambda,h) \simeq \Phi_o(\lambda) \exp\left\{-\sum_i \sigma_i(\lambda)\ N_i(h)\right\}$

Using this expression, Φ_o from column (20) and the maximum intensity Φ from column (9,10), the minimum number density per column N can be computed which then determines the highest altitude that can be simulated.

Soft X-Ray Spectrum

Types of Detectors. For the soft X-ray region the simple detectors available are: a gas counter (proportional and Geiger regions), a photomultiplier with an appropriate scintillator, and a photographic emulsion. The Geiger counter and the photomultiplier are very useful since a multiplication factor of $> 10^6$ allows for the detection of very small fluxes.

A survey of the possible choices for monitoring the simulated X-ray flux has shown that the most feasible is an ionization chamber or photon counter of the types successfully flown in rocket-borne experiments [99]. These counters have sensitivities in the following ranges: 8 to 20, 44 to 60, and 44 to 100Å. The detectors will determine the major areas of the energy curve and thus monitor the distribution of the X-ray spectrum with reasonable accuracy. The spectral sensitivities of various transmission windows for the hard and soft X-ray regions are shown in Figures 29 to 33. The pertinent parameters regarding gas filling and window characteristics are noted.

Several gas mixtures are suitable in Geiger counters. Usually a rare gas is combined with a quenching agent, a simple hydrocarbon such as alcohol or ether, a halogenated hydrocarbon such as methylene bromide, a halogen, or nitric oxide. In some cases, possible reaction with the tube material must be considered [20]. The 44 to 60Å Geiger counter as designed by Accardo [100] is suggested as the most versatile and appropriate soft X-ray monitor for the ionospheric simulator.

Operation of Geiger Counter. The operation of a Geiger counter is dependent upon the incident radiation producting at least a single ion pair within the sensitive volume of the counter. This will in general be a function of many parameters including the type of radiation (quantum or corpuscular), the energy of the radiation, the wall thickness of the counter, gas filling, etc. Subsequent to the production of the ion pair, the electron is accelerated to the anode (usually a tungsten or nickel wire of several mils diameter). As the electrons approach this region of high electric field strenght in the vicinity of the center wire, they obtain enough energy to further ionize the gas in the counter by collisions. This process results in a Townsend avalanche along the wire and gives rise to an electrical pulse capable of being detected in either the anode or cathode of the counter. A trace amount of quenching

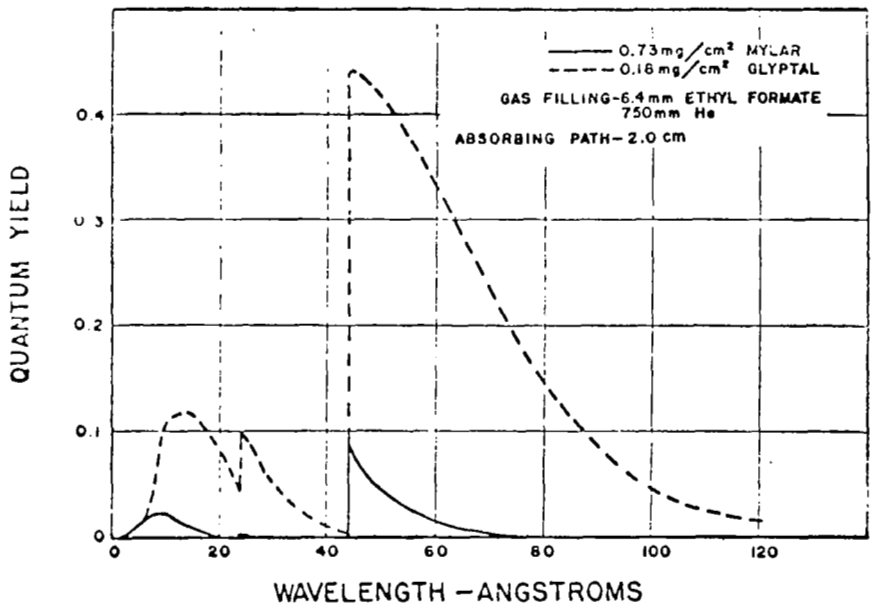

Figure 29. Spectral sensitivities of photon counters with Mylar and Glyptal windows. Discontinuities at 22 and 43Å are due to oxygen and carbon K edges. Mylar is Dupont Polyester film. Glyptal is a General Electric Co. alkyd resin. [20]

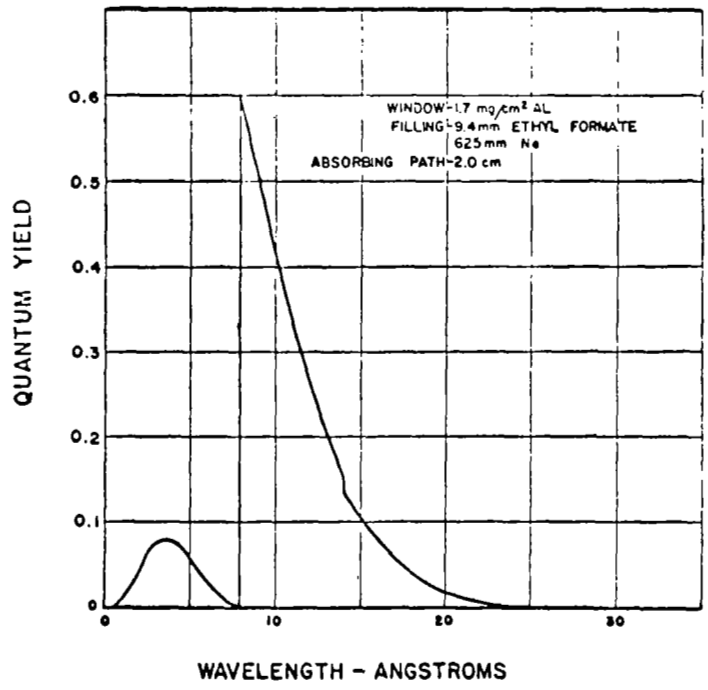

Figure 30. Spectral Sensitivity of photon counter with aluminum window. Discontinuities at 8 and 14Å are due to Aℓ and Ne K edges. [20]

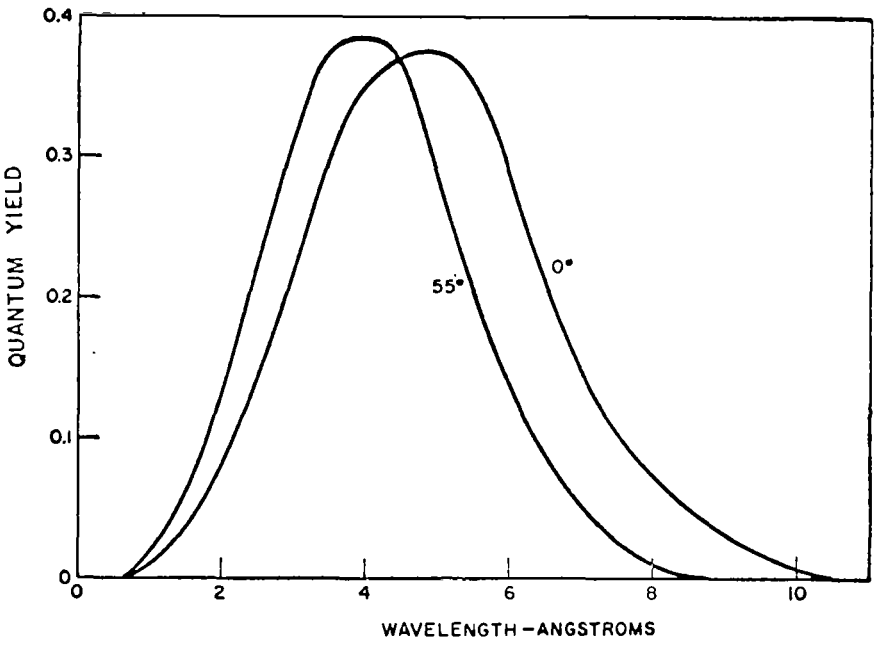

Figure 31. Spectral sensitivity of photon counter with beryllium window, 0.005 inch thick for 0^{o} and 55^{o} incidence angle. Be K edge is far from the region in which tube is used. [20]

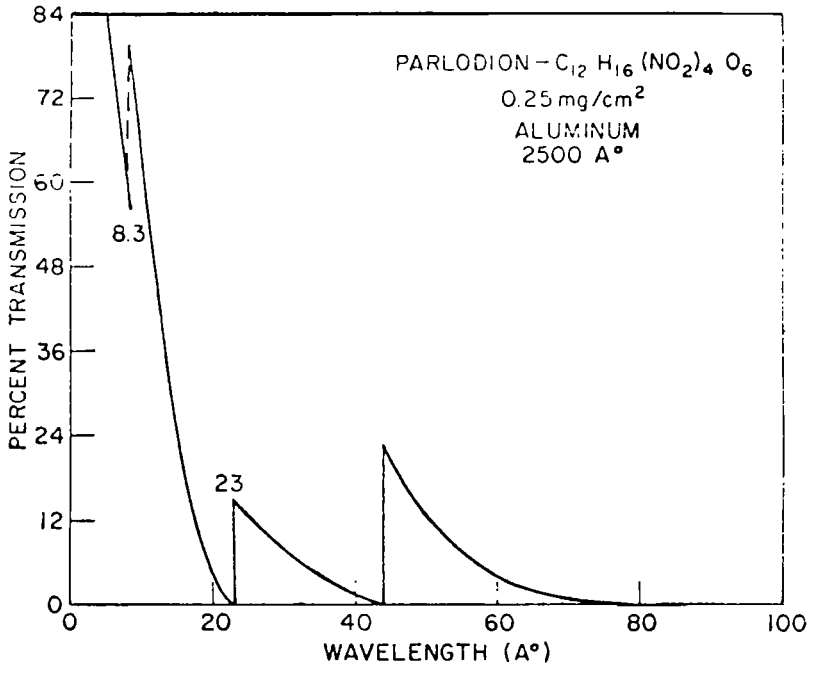

Figure 32. Spectral sensitivity of aluminized Parlodion film (a form of cellulose nitrate). [101]

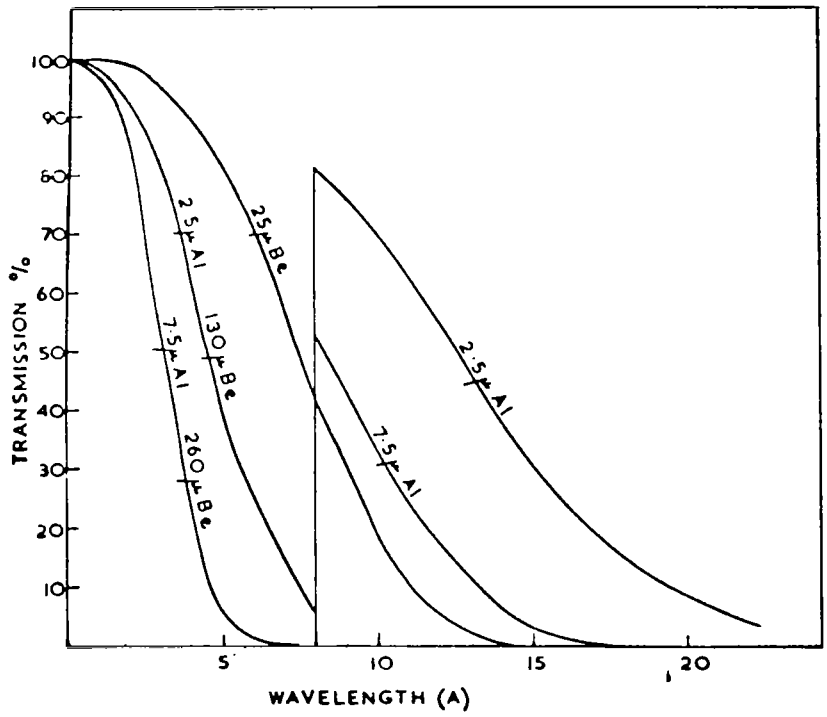

Figure 33. Spectral sensitivity of two balanced filters of aluminum and beryllium. [102]

gas is used with the primary counter gas to prevent spurious pulses from being produced.

The operating voltage of the counter is usually found from a plot of the count rate as a function of the applied voltage for a constant intensity source located at some fixed distance from the counter. Correcting for the pulses occurring during the dead time can be avoided if a low rate is selected for this measurement ($\sim$ 100c/sec). Depending on various parameters, e.g. positioning of the fine anode wire, the nature of the plateau (region of linearity) may differ. The operting voltage is normally selected near the center of the plateau.

The radiation to be measured is admitted to the counter through a thin window which is partially transparent to these wavelengths. The efficiency of the counter is given by the product of the transmissivity of the window and the photoionization of the Gas:

$$\epsilon(\lambda) = \exp\{-[\mu/\rho(\rho r)]_W\} \left\{1 - \exp\left(-[\mu/\rho\ (\rho r)]_G\right)\right\},$$

where μ/ρ is the mass absorption coefficient, ρ is the density, r is the distance traversed by the radiation, and W and G designate those terms pertaining to the window and gas, respectively. For the wavelengths of interest, mylar has proven successfuly as a window since it allows the wavelengths 44 to 60Å and 2 to 20Å to be transmitted. The high energy cutoff at 43.6Å is determined by the K edge of carbon (principal constituent of mylar), and the transmissivity at lower energies falls off approximately as the inverse cube of the wavelength. The primary gas, neon, has a very high mass absorption coefficient at the higher wavelength window and drops with increasing energy. The neon is mixed with 1.15 percent isobutane which serves as the quenching agent. For a 1/4 mil mylar window thickness and gas pressures of one-half to one atmosphere, the normal counter efficiency at 44 to 60Å is a few percent.

Construction of Geiger Counter. A photograph of the proposed design is shown in Figure 34. The Geiger counter is a rugged side-window type, self-quenched, with metal envelope and window support constituting the cathode, and ceramic-metal feed-throughs for support of the central anode wire. A metal exhaust-gas fill tubulation is centrally located in the side of the envelope. The tubes are filled to a given pressure and pinched off.

Inherent to the design is considerable flexibility in use of window materials, gas-fills, and cathode and anode materials. For the particular application to radiation in the range of 44 to 60Å, a very thin mylar window (0.00025 inch) is attached to the window support base by a special technique. The aperture is 1/4-inch diameter, but is easily changed to any practical size.

Calibration. With the exception of dispersive X-ray optics (grating spectrograph), which is expensive and highly specialized, it is very difficult to obtain monochromatic sources in the soft X-ray region and most experimentalists

Figure 34. Side window-type Geiger counter.

have depended on theoretical efficiency curves. Compton and Allison [103] suggest that absolute intensities are perhaps most easily found by measuring the heat produced from X-rays with, for example, a bolometer. Tomboulian [104] indicated that a specially constructed Geiger counter under a given situation can measure absolute photon fluxes of soft radiation. Preliminary theoretical calculations of absolute intensities, made by Tomboulian [104] may be applied for calibration purposes. Generally, few if any reliable methods are available for the calibration of counters in the soft X-ray region.

The 44 to 60Å Geiger counter flown by GCA Corporation [100] was calibrated with an iron-55 isotope source. This isotope emits a monochromatic X-ray at 1.9Å which lies within the higher energy window of the mylar counter as seen in Figure 29. Since the source strength is 5 millicuries it is possible to obtain relative efficiency measurements at various aspect angles. Unfortunately, an absolute efficiency calibration of the counter for this wavelength is not possible since the flux from the source is not known accurately.

V. IONOSPHERIC SIMULATION FACILITY

As shown in the foregoing discussion, the simultaneous simulation of many ionospheric parameters is possible. These include uv and X-ray radiation and the production of charged particles by either direct ionization of the gas within the chamber or by injecting a space-charge neutralized particle beam from a plasma gun exterior to the chamber. Similarly, it is possible to produce atomic oxygen either by direct photodissociation of oxygen within the chamber or by producing atomic oxygen exterior to the chamber and injecting a beam containing a known mixture of atomic and molecular oxygen through a port in the chamber wall.

Both the external plasma gun and the external atomic oxygen generator are expensive and bulky, particularly because they require a fairly complex differentially-pumped vacuum system. They are also expensive and need not be an integral part of the initial installation, provided adequate floor space is allowed and sufficient vacuum connecting ports on the simulation chamber are provided for their eventual installation.

The present discussion will, therefore, be confined to the design of the vacuum chamber proper, the vacuum system and the equipment for the simulation of charged particle and atomic oxygen densities, and X-ray and uv radiation integral with the ionospheric simulator.

Much thought has been given to the simulation chamber concept and in view of the complexity and cost of much of the associated equipment, it was felt that considerations pertaining to ruggedness and ease of assembly and operation should govern the design.

For this reason, a metal vacuum chamber is proposed with adequate connecting and viewing ports to permit accessibility and visual observation. High-quality stainless-steel vacuum components of great variety are now available commercially and this type of construction has considerable merit compared with a glass chamber. In particular, it is a simple matter to change the configuration of an experimental arrangement, if all components are fitted with metal flanges which are readily interchangeable. With a glass chamber, on the other hand, even small modifications require expert skill and notwithstanding great care and patience, costly and time-consuming accidents will occur.

A stainless-steel chamber is not incompatible with any of the proposed methods of simulation except with the production of atomic oxygen by photodissociation. This latter experiment requires a liner of low recombination rate, such as pyrex or teflon which can readily be inserted into the chamber.

It will be shown subsequently that a circular 1-meter diameter chamber will permit the installation of all instrumentation considered necessary. For adequate flexibility sixteen 6-inch flanged ports are recommended which will be staggered in two rows on the circumference. In addition, glass viewing ports which are commercially available in many sizes can be mounted along the circumference or on top of the chamber. The concept of the complete simulation facility is shown in Figure 35.

The Vacuum System

Methods of Pumping. The operating pressure of the simulation chamber covers the region from approximately 1 torr to 10^{-6} torr.

Whereas the attainment of these pressures presents little difficulty with conventional vacuum pumps, it is considered desirable to provide a pumping system which is accident-proof and does not introduce undesirable and uncontrolled contaminants.

During the past decade it has been established conclusively that both mechanical eccentric rotor pumps and oil diffusion pumps, no matter how well trapped, can seriously contaminate the various components of a vacuum system and affect the mechanical and electrical performance of test objects placed in such systems. Furthermore, accidental exposure of hot pump oil to atmospheric pressure may necessitate a lengthy and laborious cleaning procedure - costly in time and manpower.

Although liquid-nitrogen-trapped mercury diffusion pumps can operate in completely contamination free fashion, they require a constant supply of liquid nitrogen (the vapor pressure of mercury is approximately 10^{-3} tor at room temperature). Furthermore, accidents are likely to be far more serious in view of the toxic nature of mercury vapor.

It is fortunate that the state of the vacuum art has progressed to a point where most of these difficulties can be overcome in a simple manner.

Reduction from atmospheric pressure below 1 torr in completely oil-free fashion can be attained by means of liquid-nitrogen chilled zeolite sorption pump. For example, a sorption pump containing 2 lb of zeolite after prechilling, can evacuate a 100-liter volume to 0.1 torr in less than 10 minutes. The limitation of zeolite sorption pumps is their inability to pump helium and neon, whose partial pressures in the atmosphere are 1.4×10^{-2} and 4×10^{-3} torr, respectively. Thus, simple sorption pumping cannot reduce the total pressure below 10^{-2} torr.

Oil-free pumping in the range from 10 torr to 10^{-5} torr can however, be performed by mechanical pumps which employ the Roots principle. They are relatively simple in construction, consisting primarily of two "figure-eight" intermeshing rotors revolving in a close-fitting housing, and a motor. The rotors counter-rotate and are synchronized by a pair of timing gears mounted on the rotor shafts.

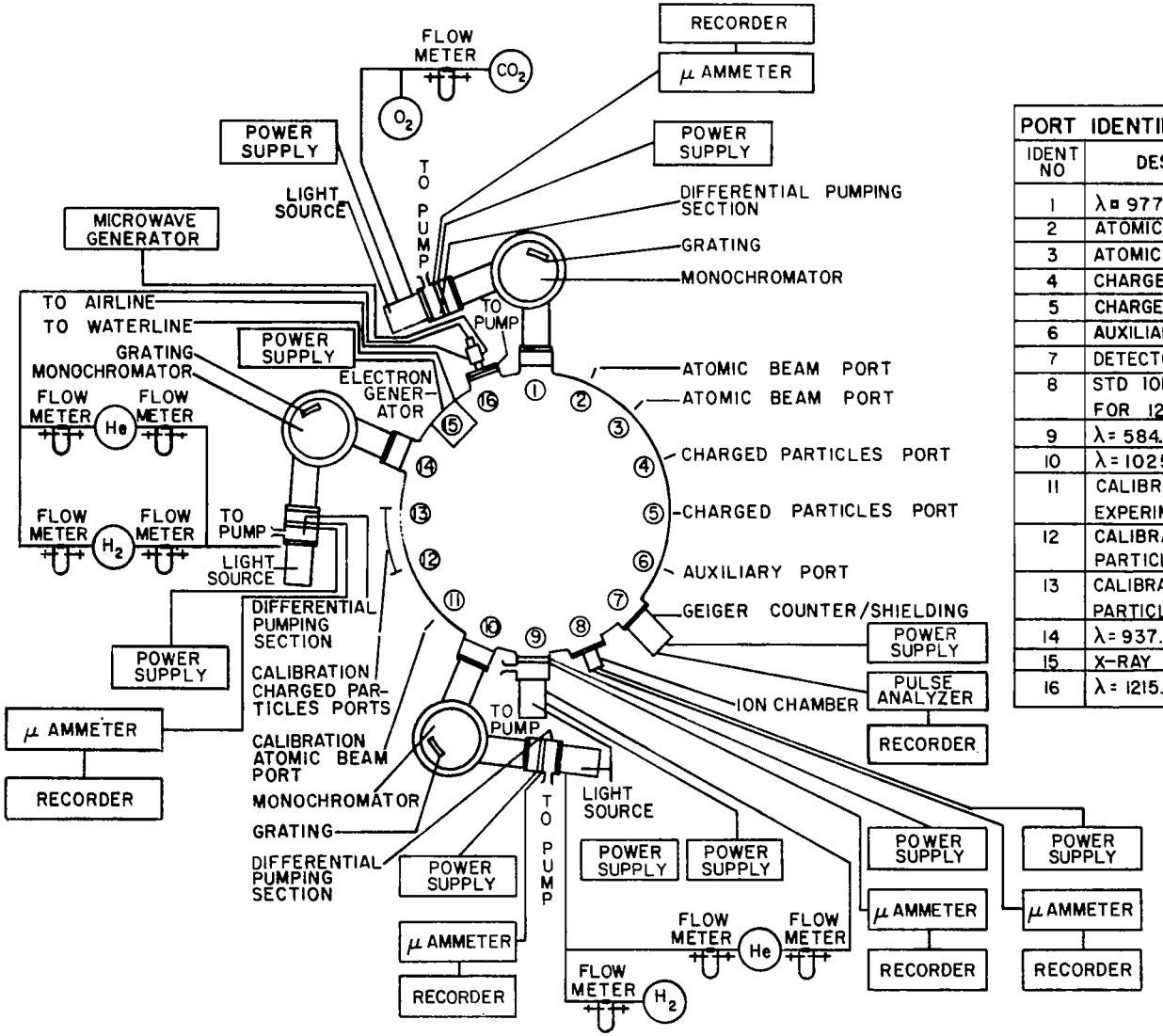

PORT IDENTIFICATION TABLE	
IDENT NO	DESCRIPTION
1	λ = 977.0 Å EXPERIMENT
2	ATOMIC BEAM EXPERIMENT
3	ATOMIC BEAM EXPERIMENT
4	CHARGED PARTICLES EXPERIMENT
5	CHARGED PARTICLES EXPERIMENT
6	AUXILIARY PORT
7	DETECTOR X-RAY EXPERIMENT
8	STD ION CHAMBER DETECTOR FOR 1215 Å
9	λ = 584.5 Å EXPERIMENT
10	λ = 1025.7 EXPERMENT
11	CALIBRATION, ATOMIC BEAM EXPERIMENT
12	CALIBRATION, CHARGED PARTICLES EXPERIMENT
13	CALIBRATION, CHARGED PARTICLES EXPERIMENT
14	λ = 937.8 Å EXPERIMENT
15	X-RAY EXPERIMENT
16	λ = 1215.7 Å EXPERIMENT

Figure 35. Ionospheric simulator block diagram

Although Roots pumps can discharge directly to atmosphere without backing pumps to produce a rough vacuum, this procedure is not recommended. The addition of a backing pump makes it possible to operate the Roots pump at lower inlet pressures; the low pressure limit under these conditions is about 10^{-5} torr. The rotors of Roots pumps are precision machined to insure a minute clearance between the rotors themselves and between the rotors and the chamber wall. As a result, no sealing or lubricating oil is needed in the pumping chamber. In consequence, back migration of pumping fluid is essentially eliminated. For ultimate cleanliness, a liquid-nitrogen cooled trap may be provided at the inlet of the Roots pump and a dry-ice or zeolite trap ahead of the backing pump.

Whereas Roots pumps operate efficiently over the pressure region covering the whole of the D Region and the lower E region, they are not capable of efficiently reproducing the pressure of the upper E Region. This limitation may be acceptable for initial operation of the ionospheric simulator. However, if evacuation to lower pressures is desired, this can also be accomplished in accident-proof and fluid-free fashion. Titanium sputter-ion pumps function very efficiently in this pressure region. Some of the ions and excited atoms produced in the electrical discharge of these pumps can, however, migrate into the simulation chamber. No such problems arise with turbomolecular mechanical pumps which perform satisfactorily from about 10^{-3} to below 10^{-9} torr. These pumps consist of a stator and rotor made up of discs into which are milled inclined radial slits. The rotational speed of the rotor is 16,000 rpm. For optimum performance a forevacuum of less than 5×10^{-3} torr is required, which, as in the case of Roots pumps, is provided by a trapped eccentric rotor pump.

A pumping system consisting of a single eccentric rotor pump which alternately backs a Roots pump or a turbo-molecular pump via suitable valving appears to be the most attractive solution to the problem outlined above. For initial evacuation from atmospheric pressure into the range to 10^{-2} torr, one or more commercial liquid-nitrogen-chilled sorption pumps can be added to the system.

Vacuum Gauges. The pressure range to be monitored includes the difficult region between 1 torr and 10^{-3} torr where, until recently no reliable commercial continuously-reading monitors were available. Below 10^{-3} torr, a wide variety of good commercial ionization gauges can be obtained.

The McLeod gauge, in spite of its excellent accuracy, is not a very convenient pressure monitor, and in any case, does not lend itself to automatic pressure control. Fortunately, high accuracy of measurement and pressure control can be obtained with a commerical capacitance manometer. Unlike other types of pressure monitors (ionization or thermal conductivity gauges), a capacitance manometer gives a pressure indication independent of the species of gas to an accuracy better than 2 percent full scale over the pressure range from 1000 torr to 5×10^{-4} torr. Below this level, an ionization gauge is the most reliable pressure monitor. The output signal of the capacitance manometer or the ionization gauge can be used to actuate a commercial pressure

controller which can maintain the pressure, via a variable gas leak, at a constant value with less than 0.3 percent full scale random drift per day.

Simulation of Charged Particles

As discussed in some detail in Section III, the production of charged particles under conditions of thermal equilibrium can be realistically simulated over only a limited-altitude range. With available sources of ultraviolet radiation, as discussed in the following section, the charged particle density can be produced directly by photoionization at a gas pressure of 100 μ, corresponding to an altitude of 80 km.

At other altitudes, the production of charged particles by photoionization cannot be performed under conditions which simulate other ionospheric parameters realistically.

Compromise solutions can include a fast electron gun or a plasma gun as discussed in Section III, which will require differential pumping. Since the design of these devices has been adequately documented in the literature referred to previously, they can be added to the simulation facility at some later date. For this purpose, an adequate number of 6-inch flanged ports have been made available on the proposed simulation chamber.

Another area, which is also widely documented is that of charged particle detectors, which range from simple ionization chambers for measurement of total charge produced to charged particle spectrometers of varying degrees of sophistication. A decision on the most suitable type of instrumentation will depend on the types of experiments proposed and need not be made in the initial planning phase. The chamber dimensions have been chosen sufficiently large to accommodate all types of charged particle detectors in current use.

Simulation of Important Vacuum Ultraviolet Solar Lines

The conceptual design of the experimental facilits shown in Figure 35 includes the latest techniques to simulate the important vacuum and extreme ultraviolet solar lines and is the result of detailed analysis of the relative merits of pertinent experimental apparatus. Not readily evident is the absence of the He II 304 Å light source. It was decided to omit this light source altogether, because it produces the least important of the series of solar ultraviolet emission lines necessary for the simulation of the E region (depth at unit optical thickness is 182 km, which lies in the F_1 region) and because the experimental difficulties of simulating this line are severe. It requires a spark discharge source which is not necessary for simulating the other solar lines. The photon fluxes emitted are not very intense and are further reduced if a monochromator is used, since the reflectivities of the various gratings that are available today are poor below 400 Å. In the following sections, the salient features of the instrumentation are discussed in some detail.

Vacuum Ultraviolet Monochromators. In Section IV it was shown that some light sources could be made nearly monochromatic by means of gas and/or thin metal filters. This was suggested as a means to separate the Lyman β (1025.7Å) and the Lyman ϵ (937.8Å) atomic lines in the hydrogen spectrum without having to use two monochromators. For the C III (977.0Å) line, on the other hand, a monochromator was deemed essential since it is not possible to separate this line without allowing other equally intense impure lines to be emitted also.

After considering the expected loss of intensity due to the various filters and the resulting loss of spectral purity, it became obvious that a dispersive device was the best approach to separate Lyman β and Lyman ϵ. Once this was decided, detailed studies were made concerning various designs of vacuum ultraviolet monochromators. One approach was based on a separate chamber, containing a single grating along a 0.5m or 1-meter Rowland circle from which all pertinent wavelengths could be focussed into one port of the ionospheric simulation chamber. Calculations indicated that, for this purpose, 5 light sources would have to be positioned on the circumference of the Rowland circle separated by a distance of 4 degrees, that is, 10 cm. Although, at first glance, this seemed impracticable, further study indicated that the capillaries of the various light sources (whose diameter is less than 1 cm) might be stacked sufficiently closely to meet this restriction. However, a firm design could not be worked out without further laboratory studies.

Another approach considered was the stacking of two 5-mm gratings in a single monochromator for the separation of the 937.8Å and 1025.7Å atomic hydrogen lines. However, the cost of designing and constructing this special monochromator will be greater than the cost of the more conventional instrumentation proposed below.

The final design consists of three monochromators which approximately duplicate the arrangement by Seya and Namioka [105]. It was chosen mainly because the 35-degree angle of incidence results in favorable intensities within the prescribed geometry. This configuration is not quite as compact as a monochromator where the angle of incidence is increased to 70 degrees and where the entrance and exit slits can be nearly in line close to the axis. Calculations showed that in the latter case, the beam would be attenuated by a factor of 3; furthermore, an instrument of this type would have to be specially designed and constructed.

The specifications for the three monochromators are as follows: the diameter of the Rowland circle is 0.5 m with a grating (platinized) of 1200 lines/mm and blazed at 750Å. Simple rotation of the grating will give the desired line yet maintain good focusing of the image. A resolution of 1Å is then available which is more than adequate for line emission light sources. A fast 4-inch oil diffusion pump (backed by a 13 CFM mechanical pump) which produces a vacuum of 10^{-5} torr should be provided. This pressure can be maintained under operating conditions, i.e., with windowless light sources, since a differential pumping section is available. It is suggested that at least one of the monochromators be equipped with a drive mechanism so that the entire wavelength region of interest can be scanned by rotating the grating.

Ultraviolet Detectors and Calibration Techniques. The proposed detectors outlined below represent the present state of the art which has progressed considerably in recent years. They include ionization chambers and photoelectric detectors. The various calibration techniques are outlined in some detail.

Ionization chambers. The ionization chamber is commonly used when an absolute radiant flux measurement is required. The conventional chamber has two parallel plates, one the ion collector and the other the ion repeller. The ions are formed in a region where the electric field is uniform and sufficiently large to collect all ions but not large enough to cause ion production by secondary electron collisions. Using the measured ion current and the known photoionization yield of the filling gas, the absolute radiant flux can be determined.

A simpler and more compact ion chamber can be constructed out of a metal cylinder and central collector pin. This construction is commonly called a photon counter, [106]. Such counters are suitable as narrowband detectors of absolute radiant flux in the vacuum ultraviolet region of the spectrum. Their bandwidth lies between the wavelength corresponding to the ionization potential of the gas and the shortwave limit of transmission of the window. For example, a counter filled with nitric oxide gas with a lithium fluoride window is sensitive from 1350Å (ionization potential of NO) to 1050Å (the limit of transmission of lithium fluoride).

As a detector of absolute radiant flux, the photon counter can be applied as a secondary standard in the laboratory or as a narrowband detector as applied by NASA and the U.S. Naval Research Laboratory to determine the absolute radiant flux from the sun in the vicinity of the Lyman-α line (1215.7Å). For the ionospheric simulator, this photon counter is proposed for the detection of Lyman-α (1215.7Å using nitric oxide as the filling gas.

Experiments have shown that the effect of impurities in nitric oxide on the photoionization current for Lyman-α is only one percent. Since the photon counter is used for detecting only Lyman-α (1215.7Å), the effect of impurities is not detrimental; in fact, it may even be beneficial since the photoionization current at wavelengths other thay Lyman-α is decreased. However, the unpurified gas is probably more corrosive than pure nitric oxide and this should be borne in mind.

Calibration of NO-filled photon counters and O_2 filled ionization chambers. It is known that calibrated NO-filled photon counters can be purchased on the open market, however, since all the instrumentation necessary to calibrate these counters will be available as part of other apparatus, it is strongly suggested that this calibration be performed in situ.

To calibrate the photon counters, the total photon flux emerging from the exit slit of the monochromator is measured with an ionization chamber filled with nitric oxide gas. From the known photoionization yield [80] of NO the radiant flux is determined. This flux is then compared with the

$$eY' = i/P \tag{32}$$

or

$$Y' = Y\ i/I \tag{33}$$

Subsequent counters can be calibrated directly against the one initially calibrated against the ion chamber.

The detection and calibration of Lyman β (1025.7Å) can be performed by one of two methods. The first utilizes the photoionization yield of oxygen, the second depends on the photoelectric yield of a metal. The principles of and procedures for the calibration of an ionization chamber filled with oxygen for Lyman β are essentially the same as that described for Lyman α except that for Lyman β, the conditions are windowless, and thus differential pumping is necessary. The dimensions of the ionization chamber can be the same as those mentioned above or can be made smaller if necessary. The absolute photon flux is calculated from Equation (31), using Y = 55 percent for O_2 at 1025.7Å.

Metallic photoelectric detector. For all other wavelengths, namely, 1025.7, 937.8, 584.5 and 303.8Å, the metallic photoelectric detector serves not only as a detector of radiation but also as a secondary standard. The procedure, which is as follows, is quite simple. A sample of aluminum or platinum (untreated), large enough to intercept the light beam near the entrance of the light source is cleaned with acetone or benzene before placing it in the system. It is mounted in front of the light source, by means of a traverse rod which allows the metal to be moved in and out of the light beam at will without breaking the vacuum. A circular wire loop is mounted directly in front of the metal surface to collect the photoelectrons ejected. With the light source on, the photoelectric current of the metal sample is measured by increasing the voltage between the loop and the surface until all electrons are collected. The absolute photon flux, P, can then be calculated by the formula:

$$Y = \frac{i/e}{P} \tag{34}$$

where Y is the photoelectric yield of the metal at a given wavelength, i is the current in amperes and e is the electronic charge. The metal detectors should be calibrated using the photoionization of rare gases technique prior to mounting them in the chamber. The specific experimental details of this method are given in the literature [85].

Vacuum Ultraviolet Light Sources. For the simulation of the various solar ultraviolet emission lines, at least three different light source designs are proposed, a result of detailed studies to optimize performance and to facilitate adequate instrumentation.

Microwave discharge lamp. For Lyman α, (1215.7Å), the microwave discharge lamp is the most applicable. The microwave light source is simply a long quartz tube placed within a microwave cavity. The quartz tube in the cavity has to be forced-air-cooled to dissipate the intense heat generated by the discharge. The quartz tube is sealed by a Teflon ferrule via a "Swagelok" fitting to a water-cooled flange. A 2450 Mc, 125-watt microwave generator is used to excite the cavity. By adjusting the tuning stub, maximum coupling light intensity can be achieved. The hydrogen spectrum produced in the microwave cavity is similar to that of the dc glow and hot-filament arc-discharges, discussed below, although somewhat weaker. Like the hot filament arc, the microwave discharge in hydrogen tends to favor the atomic spectra. In a hydrogen-helium mixture, the microwave discharge produces perhaps the most monochromatic source of Lyman-α radiation. The advantages of an electrodeless discharge are the absence of sputtered electrode material and impurities embedded within the electrodes. This, in turn, prolongs the life of the windows.

The radiation is transmitted through a window of lithium fluoride. The plates are about 2 mm thick and 25 mm in diameter. Cleaved plates are preferred to polished plates because of their superior transmission characteristics. The action of the discharge and/or the formation of F-centers on prolonged use causes accumulative loss of transmittance, requiring periodic replacement of the window. Rapid and convenient replacement can be achieved by the O-ring design shown in Figure 37 due to Warneck [107]; the window is placed between two butyl-rubber O-rings, located in grooved brass flanges.

Hot filament discharge lamp. For the simulation of the 1025.7, 977.0, and 937.8Å lines, the hot filament arc discharge lamp has been found to be more efficient than other available light sources. For the two higher members of the Lyman series of atomic hydrogen, namely, β and ϵ, a mixture of hydrogen and helium produces the maximum intensity. For the C III, 977.0Å line, carbon dioxide with a trace of oxygen produces the best results. A general description and the advantages of this lamp follows.

The use of hot filaments to provide the free electrons necessary to sustain a discharge in hydrogen and other gases has been described in the literature [108,109]. A hot-filament arc discharge can support a discharge current of several amperes at low voltage, typically 50 to 100 V. Thus, there is no need for a high voltage power supply. A typical 150 V - 5 A power supply is shown in Figure 38 which can easily be constructed by most laboratories. Should a higher degree of current stabilization be required, an excellent circuit is given by Moak, et al. [110]. Although periodic renewal of the filament is required, this does not present any particular difficulties.

The proposed hot filament arc source shown in Figure 39 is due to Hartman [109,111]. The filament is a helically coiled nickel ribbon dipped in barium carbonate and activated in a hydrogen atmosphere. A trigger pin is inserted in the quartz discharge tube to strike the arc initially. A Tesla coil is suitable to trigger the discharge. The filament draws

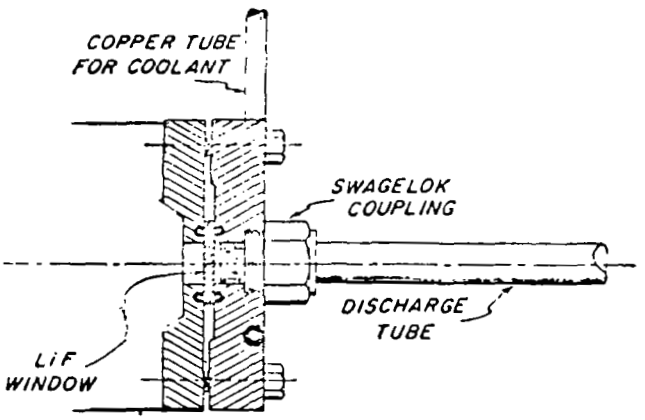

Figure 37. Diagram of the light source.

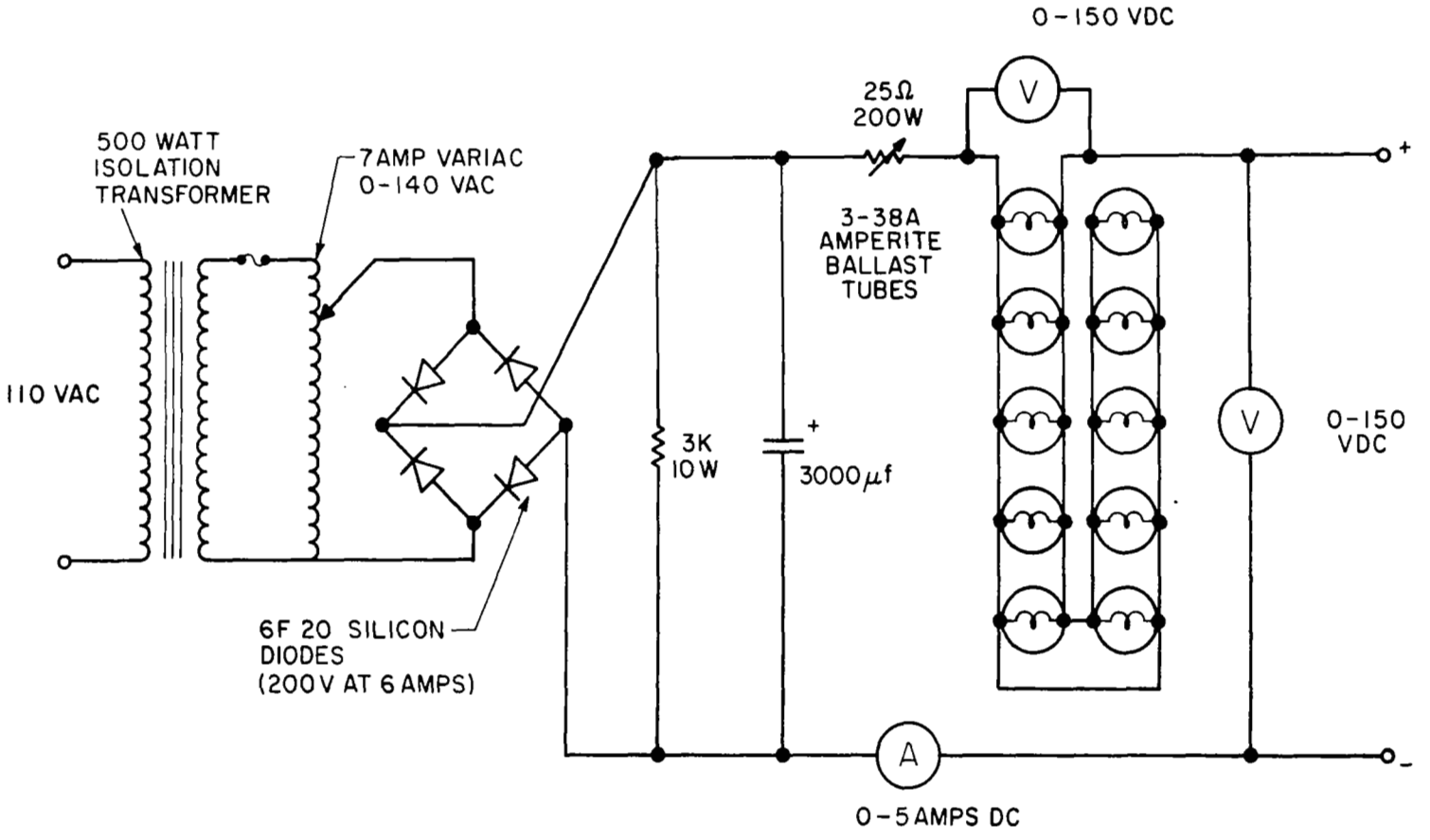

Figure 38. Current regulated power supply.

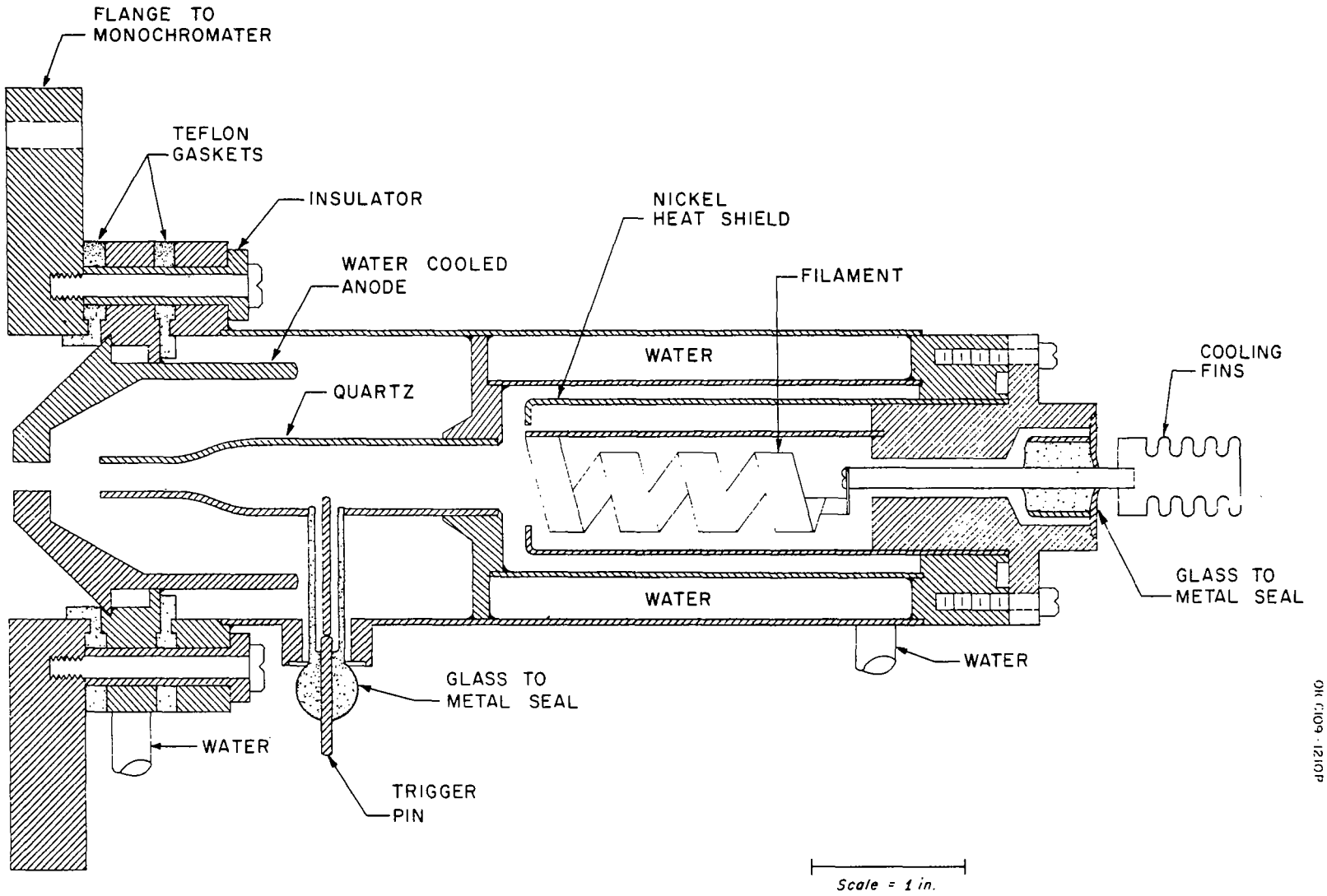

Figure 39. Hot filament discharge lamp.

approximately 12 A at 4 volts, the discharge voltage is about 90 V when an arc current of 3 A is passed in hydrogen.

Although the arc discharge produces a strong hydrogen molecular spectrum, the atomic resonance line is by far the most intense line. Furthermore, the higher members of the Lyman series of atomic hydrogen, β and γ appear clearly above the weaker molecular bands. The intensity of the atomic lines in the pure hydrogen discharge do not change appreciably when helium is added; however, the intensities of the molecular lines are greatly reduced. The hot filament arc discharge in hydrogen produces an overall more intense spectrum than the cold cathode discharge. The intensity ratio is only a factor of two or three; however, the ratio of atomic to molecular line intensities is much greater for the hot filament arc discharge.

Helium plasma light source. A simple but intense helium 30-watt light source has recently been developed which can emit more than 10^{16} photons/sec (10^{15} photons/sec/cm^2) at 584Å. The details of this source as developed by Jensen and Libby [112] are as follows:

A thoriated tungsten wire, the hot cathode and a tantalum wire, the anode are encaged in a large metal cannister. Typical operating conditions are a helium pressure of 300 microns and an applied potential of 30 V, with 1 A flowing. The exact source dimensions and geometry are not critical, however, the following arrangement has been suggested: a cathode of 0.010-inch diameter, thoriated tungsten wire, 3 cm long, parallel to and 1 cm from a 0.020-inch diameter tantalum wire, 3 cm long, serving as anode. The device has several current modes depending on cathode temperature, anode voltage and helium pressure. The low-current mode is equivalent to ordinary operation of a vacuum diode tube; the intermediate-current mode of hundreds of milliamperes to a few tens of amperes is the condition in which the device operates as presently described; the high-current mode is a typical low-pressure arc. If the pressure drops to less than 50 microns, if the cathode temperature is too low to cause significant thermionic emission, or if the anode voltage falls to less than 22 V, the device operates into the low-current mode. The transition is gradual in the case of varying cathode temperature but very abrupt when pressure or anode voltage are varied. A drop of less than 0.1 V, for example, will cause the current to fall from many amperes to a few milliamperes. With very pure helium and well-out-gassed electrodes the process is reversible; otherwise there is a hysterisis effect and a higher starting voltage is necessary, although again the current rises from milliamperes to amperes over a 0.1-V potential change. In the intermediate-current mode, anode current is determined primarily by cathode temperature. Anode voltage has little effect once it has been raised past the striking level. Separation between cathode and anode can be increased to 7 cm with no appreciable increase in required anode voltage. The factor which limits the current is the amount of heat which the anode and the lead-in conductors can dissipate. In the intermediate-current mode the source resistance is positive and therefore no ballast resistance is required for stable operation. With a very stable low-output-impedance power supply there is no evidence of oscillations up to frequencies of 100 Mc/sec. The high-current mode occurs when anode potentials

are increased to several hundred volts. This is a typical low-pressure arc and a resistor must be placed in series with the source to obtain stable operation.

The intensity of the 584Å line is greatest from the cathode region and reaches a maximum a millimeter or so from the cathode in the direction away from the anode. Light intensity is roughly proportional to current and inversely proportional to anode voltage. A maximum 584Å intensity is obtained at around 300 microns helium pressure. It is suggested that either a 2000Å aluminum foil or carbon film be used to filter out the Lyman-α line which is present as an impurity. In addition, cooling of the anode is expected to reduce the Lyman-α line dramatically.

Conclusions. The previous paragraphs have described in detail the simulation of important solar ultraviolet emission lines according to the most up-to-date methods. Reference is now made to Table 24, column (13), which shows that for a 1 meter in diameter chamber, Lyman β, C III, and Lyman ϵ cannot be simulated to an altitude higher than 130 km. The figures given in the table are minimum values which can be expected under normal circumstances in the laboratory. If the slits of the monochromators are increased to 300μ (30μ was used for the above figures), a resolution of about 10Å can be expected which can be easily tolerated with line emission light sources. Increasing the slit width will, under these circumstances, increase the above-quoted intensities by at least a factor of 10 which will enable all of the lines to be simulated up to 130 km, with the exception of Lyman ϵ which will be simulated to an altitude of 125 km. Under the prescribed circumstances, this is the best that can be done with a one-meter chamber, unless one resorts to a smaller diameter which, in turn, will cause various instrumentation problems.

The previously described helium plasma light source theoretically should emit at least two resonance lines, namely, He I and He II; however, no data are available concerning the He II line. It would, therefore, be advantageous to check this experimentally, since one might be in a position to at least partially simulate the 304Å line at no additional expense.

Soft X-Ray Source Characteristics and Design

The energy distribution of the simulated solar X-ray (continuous) spectrum from a thick target should start at approximately 40Å, the short wavelength limit, and extend toward long wavelengths with a maximum at about 50 to 60Å. The intensity will decrease beyond the maximum to a relatively low value at about 100Å. The short wavelength limit of the spectrum is inversely proportional to the potential applied between the cathode, or filament, and the target, and the wavelength characteristic of the continuous spectrum is independent of the target material. The intensity of the spectrum, however, for a given current is dependent both on the target material on the applied voltage, as well as on the thickness of the target. For a given short wavelength limit, the necessary source voltage potential is given by

$$V(\text{volts}) = \frac{hc}{e \cdot \lambda_\ell} = \frac{1.24 \times 10^{-4}}{\lambda_\ell} \tag{35}$$

where

h = Planck's constant = 6.625×10^{-27} erg.sec

c = velocity of light = 3.00×10^{10} cm/sec

e = (numerical electronic charge) = 1.6×10^{-12} ergs/volt

λ_ℓ = short wavelength limit, cm

For a short-wavelength limit of 40Å, V is 310. If the soft X-ray spectral range is extended to 10Å, the applied voltage will then be 1.24 kV. For hard X-rays (1 to 10Å), a potential of 12.4 kV is required.

The number of photons emitted from a target by a given incident electron beam increases with the atomic weight of the target material and with the voltage applied to the X-ray source. The efficiency of X-ray production ϵ is given by [113].

$$\epsilon = 1.1 \times 10^{-9} \; Z \cdot V \tag{36}$$

where Z is the atomic number of the target material and V is the applied potential in volts. Thus the atomic number is another parameter to be considered in optimum design. For a tungsten target (Z = 74) and a potential of 310 V, the efficiency is 2.5×10^{-5} or 0.0025 percent.

Although the efficiency formula implies that it is not limited to any particular range of electron energy, it was initially not clear that its validity could be assumed into the soft X-ray region of interest here. However, an order-of-magnitude calculation of the soft X-ray yield of a conventional Bayard-Alpert ionization gauge in terms of its well known X-ray limit indicated that extrapolation into the soft X-ray range was justified.

To obtain a simulated solar X-ray flux of 10^8 photons/cm^2 sec at the center of the chamber, approximately 45 cm from the X-ray source, it is necessary that the source produce 2.5×10^{12} photons/sec, assuming an intensity diminution factor based on the standard inverse square law. This diminution factor represents an extreme case, since the X-rays will not be produced isotropically at the target, but will be emitted within a more narrow envelope. Accordingly the intensity will fall off at a rate less than $1/R^2$.

The X-ray source must be operated at a current high enough to produce 2.5×10^{12} photons/sec. This plate or anode current is calculated from

$$I \text{ (amperes)} = e \cdot N \tag{37}$$

where

e = electronic charge = 1.60×10^{-19} coulombs

N = electron beam flux = Φ_o/ϵ

Φ_o = X-ray photon intensity at target

ϵ = efficiency of X-ray production (from Equation (36))

Thus the formula for plate current may be rewritten

$$I = \frac{e \cdot \Phi_o}{1.1 \times 10^{-9} ZV} = 1.45 \times 10^{-10} \frac{\Phi_o}{ZV} \tag{38}$$

or in terms of the short wavelength limit

$$I = 1.2 \times 10^{-6} \frac{\Phi_o \lambda_\ell}{Z} \tag{39}$$

For the present case ($Z = 74$, $V = 0.3$kV, $\Phi_o = 2.5 \times 10^{12}$ photons/sec) the plate current is 16 mA.

Since there are no adequate soft X-ray transmission windows, the design requires the soft X-ray source to be mounted inside the simulation chamber. The leads will be connected to a power supply outside the chamber.

A typical source is a simple diode with a heated tungsten or rhenium filament and an anode of tungsten or molybdenum (high atomic number). A more sophisticated multiple-element soft X-ray source has recently been described [114], which could be incorporated with advantage in the proposed installation.

In the arrangement shown in Figure 40 an experiment is located in the center of the simulation chamber and the soft X-ray source and Geiger counter are at the extremes of the chamber diameter.

The characteristics of the soft X-ray source are tabulated in Table 27.

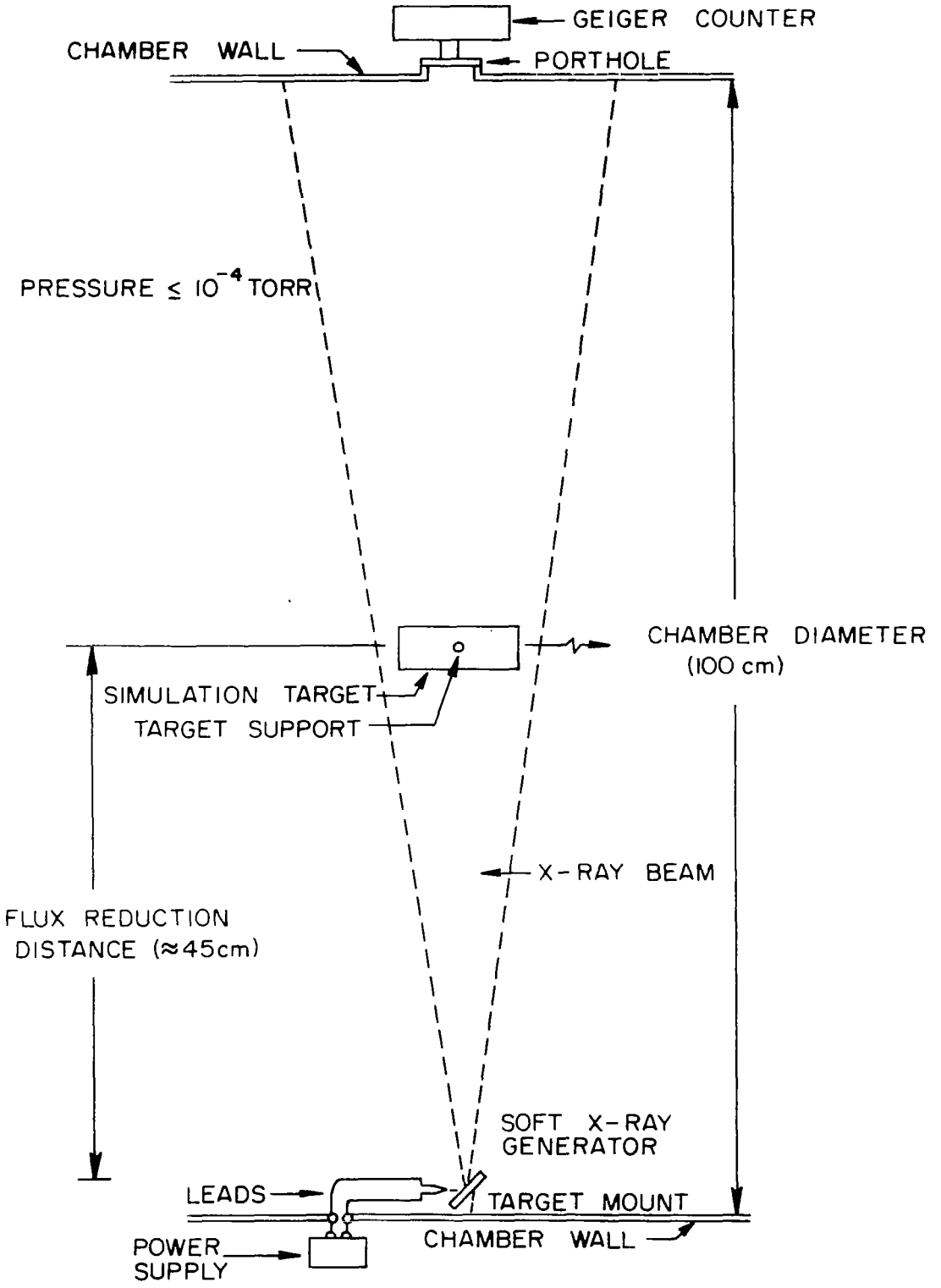

Figure 40. Dimensions and location of soft x-ray generator in simulation chamber.

TABLE 27

SOFT X-RAY SOURCE CHARACTERISTICS

Operating Voltage:	0.3 kV (40Å short wavelength limit)
Operating Current:	16 mA
Electron Beam Flux:	10^{17} electrons/sec
X-Ray Production Efficiency:	2.5×10^{-5}
X-Ray Target Intensity:	2.5×10^{12} photons/sec
Target:	Molybdenum or Tungsten
Filament:	Rhenium or Tungsten
Operating Pressure in Chamber:	$\leq 10^{-4}$ torr
Solar Flux to be Simulated:	$\approx 10^{8}$ photons/cm^2 - sec
X-Ray Photon Flux at Simulation Target:	$\approx 10^{8}$ photons/cm^2 - sec
X-Ray Photon Flux at Detector Window:	$\approx 2 \times 10^{7}$ photons/cm^2 - sec
Detector:	Geiger counter with 44 to 60Å Mylar window
Location:	Mounted inside chamber
Distance X-ray Target to Simulation Target:	$\approx$ 45 cm
Calibration:	Theoretical

Simulation of Atomic Oxygen

As shown in Section III, realistic simulation of the density of atomic oxygen can be accomplished over various portions of the D region by ultraviolet photodissociation. Apart from a simple gas flow inlet-system, no equipment additional to a xenon lamp producing radiation at 1471Å is required. However, as stated previously, a liner of low recombination rate, such as pyrex or teflon will have to be inserted into the simulation chamber for this experiment.

The measurement of the density of atomic oxygen can be performed by the well-known titration method first suggested by Spealman and Rodebush [115] and successfully used by Kaufman [116] and also by Herron and Schiff [117]. Herzog [118] has recently undertaken an investigation into the absolute measurement of atomic oxygen concentration by observing the heat of recombination in a recombination cell. He reported that the agreement between the titration method and the heat of recombination method was good. However, during experiments still in progress [119] where he compared the performance of the recombination cell with mass spectrometric partial pressure measurements [117] of O^+, O_2^+, NO^+ and NO_2^+, he noticed several discrepancies which have yet to be resolved.

The production of oxygen with an atomic beam system external to the simulation chamber has been discussed in Section III. The equipment has been described in great detail by Herzog [120] and can be added to the ionospheric simulation facility at a later date if required.

VI BIBLIOGRAPHY

Recent Reviews

Current papers and reports dealing with the general areas of (1) solar X-ray and ultraviolet radiation, and (2) solar interaction with the ionosphere and charged particles are so numerous that only specifically appropriate papers and recent reviews of these subjects are included.

Solar X-Ray and Ultraviolet Radiation.

(1) Detwiler, C.G., et al., "The Intensity Distribution in the Ultraviolet Solar Spectrum," Ann. Geophys. 17, 263 (1961).

(2) Elwert, G., Space Sci. Rev. 4, (in print, 1965).

(3) Friedman, H., "Lyman-alpha Radiation," Ann. Geophys. 17, 245 (1961).

(4) Friedman, H., "Rocket Spectroscopy," in Space Science, (D.P. LeGalley, ed.), p. 549, John Wiley and Sons, New York (1963).

(5) Friedman, H., "Ultraviolet and X-Rays from the Sun," in Annual Reviews of Astronomy and Astrophysics 1, (L. Goldberg, ed.), p. 59, Annual Reviews Inc., Palo Alto (1963).

(6) Hinteregger, H.E., "Monochromatic Measurements of Lyman Series Emission of Solar H and He+." Proceedings Tenth International Astrophysical Symposium, p. 111, Liege (1961).

(7) Hinteregger, H.E. et al., "Solar Extreme Ultraviolet Photon Flux Measurements in the Upper Atmosphere in August 1961," in Space Research III, p. 745 (1962).

(8) de Jager, C., "Solar Ultraviolet and X-Ray Radiation," in Research in Geophysics 1, (H. Odishaw, ed.), p. 1, MIT Press, Cambridge (1964).

(9) Johnson, F.S., "The Solar Constant," J. Meteorol. 11, 431 (1954).

(10) Kreplin, R.W., "Solar X-Rays," Ann. Geophys. 17, 151 (1961).

(11) Kreplin, R.W., Chubb, T.A. and Friedman, H., "X-Ray and Lyman Alpha Emission from the Sun as Measured by the NRL SR-1 Satellite," J. Geophys. Res. 67, 2231 (1962).

(12) Kundu, M.R., "Centimeter-Wave Radio and X-Ray Emission from the Sun," Space Sci. Rev. 2, 439 (1963).

(13) Lindsay, J.C., "The Solar Extreme Ultraviolet Radiation (1-400Å)," Planet. Space Sci. 12, 379 (1964).

(14) Pagel, B.E.J., "Ultraviolet Emission from the Sun," Planet. Space Sci. 11,333 (1963).

(15) Pottasch, S.R., "On the Interpretation of the Solar Ultraviolet Emission Line Spectrum," Space Sci. Rev. 3, 816 (1964).

(16) Schultz, E.D. and Holland, A.C., "The Solar Flux Incident at the Top of the Atmospheres of Earth and Neighboring Planets for the Spectral Region 50Å-3000Å, GCA Tech. Rpt. 62-14-N, Bedford (1962).

(17) Tousey, R., "The Extreme Ultraviolet Spectrum of the Sun," Space Sci. Rev. 2, 3 (1963).

(18) Watanabe, K., (See: Nawrocki, P.J. and Papa, R., "The Solar Spectrum and Cross Sections for Photoionization and Absorption," Chapter 2 in Atmospheric Processes, Pergamon Press, N.Y. 1962).

Solar Interaction with the Ionosphere and Charged Particles

(1) Adams, G.W. and Mosely, A.J., "Production Rates and Electron Densities in the Lower Ionsphere due to Solar Cosmic Rays," J. Atmos. Terr. Phys. 27, 289 (1965).

(2) Allen, C.W., "The Interpretation of the Extreme Ultraviolet Spectrum," Space Sci. Rev. 4, 91 (1965).

(3) Bates, D., "Formation of the Ionized Layers," J. Atmos. Terr. Phys. Special Suppl. 6, 184 (1956).

(4) Bauer, S.J., "Helium Ion Belt in the Upper Atmosphere," Nature 197, 36 (1963).

(5) Biggs, F., "The Distribution of Absorbed X-Ray Energy in the Atmosphere, "Sandia Corp. Res. Rpt. SC-4759/RR, Albuquerque (1963).

(6) Bourdeau, R.E., "Ionospheric Research from Space Vehicles," Space Sci. Rev. 1, 683 (1963).

(7) Dalgarno, A., "Charged Particles in the Upper Atmosphere," Ann. Geophys. 17, 16 (1961).

(8) Dalgarno, A. and Henry, R.J.W., "Electron Densities in the D-Region," GCA Tech. Rpt. 65-8-N, Bedford (1965).

(9) Dalgarno, A., McElroy, M.B. and Moffett, R.J., "Electron Temperatures in the Ionosphere," Planet. Space Sci. 11, 463 (1963).

(10) Friedman, H., "Ionospheric Constitution and Solar Control," Research in Geophysics 1, (H. Odishaw, ed.), p. 197, MIT Press, Cambridge (1964).

(11) Gerson, N.C., "Unsolved Problems in High Atmospheric Physics," Advances in Geophysics Vol. 1, 155 (1952).

(12) Istomin, V.G. and Pokhunov, A.A., "Mass Spectrometer Measurements of Atmospheric Composition in the USSR," in Space Research I, p. 117, No. Holland, Amsterdam (1961).

(13) Ivanov-Kholodny, G.S., "Investigation of Electron Concentration in the Lower Part of the Ionosphere (D-Region)," Geomagn. and Aeron. 4, 337 (1964).

(14) Johnson, C.Y., Meadows, E.B., and Holmes, J.C., "Ion Composition of the Arctic Ionosphere," J. Geophys. Res. 63, 443 (1958).

(15) Meadows, E.B. and Townsend, J.W. Jr., "Rocket Measurements of Arctic Atmospheric Composition above 100 km," in Space Research I, p. 175, No. Holland, Amsterdam (1961).

(16) Narcissi, R.S. and Bailey, A.D., "Mass Spectrometric Measurements of Positive Ions at Altitudes 64-112 km," in Space Research V, p. 735, No. Holland, Amsterdam (1965).

(17) Nicolet, M., "Dynamic Effects in the High Atmosphere," in The Earth as a Planet (G. Kuiper, ed.), p. 644, Univ. Chicago Press, Chicago (1954).

(18) Nicolet, M. and Aiken, A., "The Formation of the D-Region of the Ionosphere," J. Geophys. Res 65, 1469 (1960).

(19) Nicolet, M. and Swides, W.J., "Ionospheric Conditions," Planet. Space Sci. 11, 1459 (1963).

(20) Norton, R.B., Van Zant, T.E., and Denison, J.S., "A Model of the Ionosphere in the E and F Regions," in Proceedings of the International Conference of the Ionosphere, Inst. Physics and the Physical Society, p. 26, London (1962).

(21) Reid, G.C., "Physical Processes in the D-Region of the Ionosphere," Rev. Geophys. 2, 311 (1964).

(22) Smith, L.G., "Electron Densities in the Ionosphere," GCA Tech. Rpt. 63-23-N, Bedford (1963).

(23) Taylor, H.A. Jr. and Brinton, H.C., "Atmospheric Ion Composition Measured Above Wallops Island, Virginia," J. Geophys. Res. 66, 2587 (1961).

(24) Watanabe, K. and Hinteregger, H.E., "Photoionization Rates in the E and F Regions," part 1, J. Geophys. Res. 67, 999 (part 2, Hinteregger and Watanabe, p. 3373) (1962).

(25) Waynick, A.H., "The Lowest Ionosphere," in Physics of the Ionosphere, Conference Report by the Physical Society, p. 1 (1955).

Individual Papers

Solar X-Ray and Ultraviolet Simulation and Vehicle Interaction

(1) Frost, D.C. and McDowell, C.A., Final Report of Ionization Potentials of Molecules, AF 19(604)2275, Project No. 7635 (1960).

(2) Garton, W.R.S., Proceedings Fourth International Conference on Ionization Phenomea in Gases, p. 518 (1960).

(3) Gray, P.D., et al., "Rockets in Space Environment, Volume I - The Experimental Program," Aerojet-General Corp. Report No. 2484, Axuza (1963).

(4) Hartman, P.L., "Improvements in a Source for use in the Vacuum Ultraviolet," J. Opt. Soc. Am. 51, 113 (1961).

(5) Hartman, P.L. and Nelson, J.R., "Hydrogen Lamp of Good Intensity and Reliability for the Vacuum Ultraviolet," J Opt. Soc. Am. 47, 646 (1957).

(6) Hirt, R.C. and Schmitt, R.G., "Studies on the Protective Ultraviolet Absorbers in a Space Environment, " WADC TR 60-773 (1960).

(7) Horwitz. H. and McIntyre, D.V., "Solar Absorptive Measurements and Ultraviolet Irradiation in a Space Environment," (Hughes Aircraft Co., Aerospace Group), Proc. Inst. Environ. Sci., p. 189 (1964).

(8) Johnson, P., "Vacuum Ultraviolet Monochromator," J. Opt. Soc. Am. 42, 278 (1952).

(9) Mangold, V.L., "Solar Simulation in the Extreme Ultraviolet," in Proceedings of the Joint International Conference of the Institute of Environmental Science and ASTM, January 1965 (1965).

(10) Mason, J.E., "Solar X-Rays 3-12Å as Measured with a Proportional Counter Spectrometer," AFCRL Environ. Res. Paper No.68, AFCRL 64-932 Bedford (1964).

(11) Mauri, R.E., "Ultraviolet Radiation Effects on Spacecraft Materials," J. Environ. Sci. 7, (6), 18 (1964).

(12) Noonan, F.M., Alexander, A.L., and Cowling, J.E., "The Ultraviolet Degradation of Organic Coatings, Part III - Effect on Physical Properties," N.R.L. Project 7312, WADD TR 60-703 (1960).

(13) Parkinson, W.H. and Reeves, E.M., "Brightness Temperatures and Intensity Measurements in Flash Discharges," Proc. Roy. Soc. London 262, 409 (1961).

(14) Samson, J.A.R., "Vacuum Ultraviolet Light Sources," GCA Tech. Rpt. 62-9-N, Bedford (1962).

(15) Samson, J.A.R. and Cairns, R.B., "Absorption and Photoionization Cross Sections of Atmospheric Gases at Intense Solar Emission Lines: N_2, O_2, CO_2, A, and He," J. Geophys. Res. 69, 4583 (1964).

(16) Sullivan, J.D., "Investigations of Ultraviolet Solar Radiation and its Influence on the Aerospace Environment," (Comstock and Wescott, Final Rpt) AFCRL 64-773, Bedford (1964).

(17) Warneck, P., "A Microwave Powered Hydrogen Lamp for Vacuum Ultraviolet Photo-chemical Research," Appl. Optics 1, 721 (1962).

(18) Wilkinson, P.G., "New Krypton-Light Source for the Vacuum Ultraviolet," J. Opt. Soc. Am. 45, 1044 (1955).

(19) Wilkinson, P.G. and Tanaka, Y., "New Xenon-Light Source for the Vacuum Ultraviolet," J. Opt. Soc. Am. 45, 344 (1955).

(20) Yokely, C.R., "A Stable Arc Source of High Ultraviolet Radiance," in Proceedings of the Joint International Conference of the Institute of Environmental Science and ASTM, January 1965 (1965).

(21) Zerlaut, G.A., et al., "Ultraviolet Irradiation in Vacuum of White Spacecraft Coatings," in Symposium on Thermal Radiation of Solids, Session IV - Space Environmental Effects, NASA TM-X-54697 (1964).

Charged Particles Simulation and Vehicle Interaction

(1) Allen, J.E., Boyd, R.F.L., and Reynolds, P., "The Collection of Positive Ions by a Probe Immersed in a Plasma," Proc. Phys. Soc. (London), B70, 297 (1957).

(2) Bachinski, M., "Simulation of Geophysical Phenomena in the Laboratory," AIAA J. 2, 1873 (1964).

(3) Beard, D.B. and Johnson, F.S., "Charge and Magnetic Field Interactions with Satellites," J. Geophys. Res. 65, 1 (1960).

(4) Bernstein, I.B. and Robinowitz, I.N., "Theory of Electrostatic Probes in a Low-Density Plasma," Phys. Fluids 2, 112 (1959).

(5) Bourdeau, R.E., "On the Interaction between a Spacecraft and an Ionized Medium (Appendix), "Space Sci. Rev. 1, 719 (1963).

(6) Bourdeau, R.E., et al., "Measurements of Sheath Currents and Equilibrium Potential on the Explorer VIII Satellite (1960X)," NASA TND-1064 (1961).

(7) Brundin, C.L., "Effects of Charged Particles on the Motion of an Earth Satellite," AIAA J. 1, 2529(1963).

(8) Burton, B.S., Jr., "The Duoplasmatron," ARS Conference on Electrostatic Propulsion (Nov. 1960).

(9) Cairns, R.B., "Measurements of Resonance Rectification Using a Plasma Probe," Proc. Phys. Soc. 82, 243 (1963).

(10) Chopra, K., "Interactions of Rapidly Moving Bodies in Terrestrial Atmosphere," Rev. Mod. Phys. 33, 153 (1961).

(11) Davis, A.H. and Harris, I., "Interaction of a Charged Satellite with the Ionosphere," in Rarefied Gas Dynamics (L. Talbot, ed.) p. 641, Academic Press, New York (1961).

(12) Froehlich, H., Nukleonik 1, 183 (1959).

(13) Gabovich, M.D. and Ermolovich, Yu. B., "Radial Distribution of Charged Particle Concentrations in a Magnetic Ion Source," Foreign Tech. Div., AF Systems Command, WPAFB, Ohio, FTD-TT-64-442 (1964).

(14) GCA, "Plasma Beam Calibration Mass Spectrometer," GCA Tech. Note, Contract NAS5-9513, Bedford (1965).

(15) Hall, D.F., Kemp, R.F. and Sellen, J.M., "Plasma Vehicle Interaction in a Plasma Stream," AIAA J. 2, 1032 (1964).

(16) Hamman, D.J. and Wyler, E.M., "Effects on Materials and Components, Vol. II - Electronic and Mechanical Components," Batelle Memor. Inst. RSIC-151, Columbus, Ohio (1964).

(17) Hines, R.H., "Automatic Langmuir Probe Evaluation of Ion Beams," Arnold Eng. Devel. Ctr. Report TDR-64-128, Tenn. (1964).

(18) Hocks, B., "Space Charge Waves in an Accelerated Hydrogen Flow Electron Beam in a Constant Magnetic Field," Stanford Univ. Microwave Lab. Interim Rpt. ML-1205, Calif. (1964).

(19) Hoggard, W.D., "Environmental Testing of Ionosphere Explorer Spacecraft," NASA TM-X-55109 (1964).

(20) Hol, F. and Wood, G.P., "The Electrostatic and Electromagnetic Drag Forces on a Spherical Satellite in a Rarefied Partially Ionized Atmosphere," Third International Symposium on Rarefied Gas Dynamics, Paris, June 26-30 (1962).

(21) Jastrow, R. and Pearse, C.A., "Atmospheric Drag on the Satellite," J. Geophys. Res. 62, 413 (1957).

(22) Johnson, F.S., Satellite Environment Handbook, chapter 2, Stanford Univ., Press, Stanford (1961).

(23) Kornegay, W.M., "Decay of Electron Densities in the Wakes of Hypervelocity Spheres," Lincoln Lab. Tech. Rpt. TR-370 (1964).

(24) Knechtel, E. and Pitts, W., "Experimental Investigation of Electric Drag on Spherical Satellite Models," (Ames Res. Ctr.) NASA TND-2619 (1965).

(25) Kraus, L. and Watson, K.M., "Plasma Motion-Induced by Satellite in the Ionosphere," Phys. Fluids 1, 480 (1958).

(26) Meckel, B., "Experimental Study of the Interaction of a Moving Body with a Plasma," in Rarefied Gas Dynamics (L. Talbot, ed.) p. 701, Academic Press, New York (1961).

(27) Medicus, G., "Theory of Electron Collection of Spherical Probes," J. Appl. Phys. 32, 2512 (1961).

(28) Moak, C.D., et al., "Duo-Plasmatron Ion Source for Use in Accelerators," Rev. Sci. Instr. 30, 694 (1959).

(29) Pasternak, R.A., "The Study of Gases in Simulation Chambers and Outer Space," J. Environ. Sci. 7 (1), 11 (1964).

(30) Put'eva, M.B., et al., "High Vacuum Ion Source," Foreign Tech. Div., AF Systems Command, WPAFB, Ohio, FTD-TT-64-639 (1964).

(31) Samir, U. and Wilmore, A.P., "The Distribution of Charged Particles Near a Moving Spacecraft," Planet. Space Sci. 13, 285 (1965).

(32) Sellen, J.M., Jr., and Kemp, R.F., "Cesium Ion Beam Neutralization in Vehicular Simulation," LAS-ARS Reprint 61-84-1778 (1961).

(33) Shkarofsky I., "Laboratory Simulation of Disturbances Produced by Bodies Moving Through a Plasma and other Geophysical Phenomena," RCA Lab. Rpt. TM 7-901-011, Montreal (1964).

(34) Smullin, L.D. and Getty, W.D., "Generation of a Hot, Dense Plasma by a Collective Beam-Plasma Interaction," Phys. Rev. Ltr. 9, 3 (1962).

(35) Walker, E.H., "Interaction of Space Vehicles with an Ionized Atmosphere," (S.F. Singer, ed.), Pergm. Press, New York (1964).

(36) Wyatt, P.J., "Induction Drag on a Large Negatively Charged Satellite Moving in a Magnetic-Field Free Ionsphere," J. Geophys. Res. 65, 1673 (1960).

Atomic Oxygen Discussion and Simulation

(1) Bates, D.R. and Nicolet, M., "Ion-Atom Interchange," J. Atmos. Terr. Phys. 18, 65 (1960).

(2) Bates, D.R. and Seaton, M.J., "The Quantal Theory of Continuous Absorption of Radiation by Various Atoms in their Ground States," Mon. Not. Roy. Astron. Soc. 109, 698 (1949).

(3) Cairns, R.B. and Samson, J.A.R., "Total Absorption Cross Section of Atomic Oxygen below 910Å, "GCA Tech. Rpt. 65-6-N, Bedford (1965).

(4) Dalgarno, A. and Parkinson, J., "Photoionization of Atomic-Oxygen and Atomic Nitrogen," Planet. Space Sci. 12, 235 (1964).

(6) Deckers, J. and Fenn, J.B., "High Intensity Molecular Beam Apparatus," Rev. Sci. Instr. 34, 96 (1963).

(7) Herzog, R.F.K., "Development, Fabrication, Calibration and Testing of an Atomic Beam System," GCA Corp. Final Rpt. (Contract NAS5-3251), Bedford (1965).

(8) Hinteregger, H.E., "Absolute Spectrometric Analysis of the Upper Atmosphere in the EUV Region," J. Atmos. Sci. 19, 351 (1962).

(9) Hingeregger, H.E., Hall, L.A., and Schmidtke, G., "Solar XUV Radiation and Neutral Particle Distribution in July 1963 Thermosphere," in Space Research V, p. 1175, No. Holland, Amsterdam (1965).

(10) Kaufman, F. and Kelso, J.R., "Catalytic Effects in the Dissociation of Oxygen in Microwave Discharges," J. Chem. Phys. 32, 301 (1960).

(11) Nicolet, M., "The Properties and Constitution of the Upper Atmosphere," in Physics of the Upper Atmosphere (J.A. Ratcliffe, ed.), p. 17, Academic Press, New York (1960).

(12) Nier, A.O., "Neutral Composition of the Atmosphere in the 100-200 Kilometer Range." J. Geophys. Res. 69, 979 (1964).

(13) Schaeffer, E.J. and Nichols, M.H., "Upper Air Neutral Composition Measurements by a Mass Spectrometer," J. Geophys. Res. 69, 4649 (1964).

(14) Wright, J.W., "Diurnal and Seasonal Variations of the Atmosphere near the 100-km Level," J. Geophys. Res., 2851 (1964).

REFERENCES

1. GCA Technical Note, Contract No. NAS5-9513 (June 1965).

2. NASA Technical Note TND-2619 (February 1965).

3. Ghosh, S., Sharma, K. and Sharma, A., Indian J. Phys. 38, 106 (1964).

4. Nicolet, M. and Aiken, A. C., J. Geophys. Res. 65, 1469-83 (1960).

5. Kreplin, R. W., Chubb, T. A. and Friedman, H., J. Geophys. Res. 67, 2231-53 (1962).

6. Chilton, C. J., Steele, F. K. and Norton, R. B., J. Geophys. Res. 68, 5421-35 (1963).

7. Smith, L. G., "Rocket Measurements of Electron Density and Temperature in the Night-time Ionosphere," GCA Tech. Rpt. No. 62-1-N (1962).

8. Bowhill, S. A. and Smith, L. G., COSPAR, Buenos Aires, May 1965. NASA Contractor Report NASA CR-391.

9. Friedman, H., "Ultraviolet and X-rays from the Sun," Annual Review of Astronomy and Astrophysics 1 (1963).

10. Accardo, C. A., Smith, L. G. and Weeks, L. H., J. Geophys. Res. 69, 5112-15 (1964).

11. Bates, D. R. and Nicolet, M., J. Atmos. Terr. Phys. 18, 65-70 (1960).

12. Narcissi, R. S. and Bailey, A. D., COSPAR Meeting, Florence, Italy (1964).

13. Norton, R. B., VanZandt, T. E. and Denison, J. S., Proc. International Conference on the Ionosphere, Institute of Physics and the Physical Society, London, 26 (1963).

14. Watanabe, K. and Hinteregger, H. E., J. Geophys. Res. 67, 3373-92 (1962).

15. Smith, L. G., Accardo, C. A., Weeks, L. H. and McKinnon, P. J., "Rocket Measurements in the Ionosphere during the Eclipse of 20 July 1963," presented at COSPAR, Florence, Italy (1964).

16. Samson, J. A. R. and Cairns, R. B., J. Geophys. Res. 69, 4583-90 (1964).

17. Taylor, H. A., Jr. and Brinton, H. C., J. Geophys. Res. 66, 2587 (1961).

18. Manring, E. R., Bedinger, J. F. and Knaflich, H. B., "Some Measurements of Winds and of the Coefficient of Diffusion in the Upper Atmosphere," presented at COSPAR, Florence, Italy (1961); Space Research II, North-Holland Publishing Co., Amsterdam, 1107-24 (1961).

19. Dalgarno, A., McElroy, M. B. and Moffett, R. J., Planetary Space Sci. 11,463 (1963).

20. Friedman, H., "The Sun's Ionizing Radiation," Physics of the Upper Atmosphere," (J. A. Ratcliffe, ed.), p. 131, Academic Press, New York (1960).

21. Ghosh, S. and Shardanand, Proc. National Academy of Sci., India 32, 268 (1962).

22. Watanabe, K. and Hinteregger, H. E., J. Geophys. Res. 67, 999 (1962).

23. Chubb, T. A., "Solar Ultraviolet and X-ray Radiation as Observed from Rockets and Satellites," Proc. First Intern. Symp. on Rocket and Satellite Meteorology (H. Wexler and J. E. Caskey, Jr., ed.), p. 210, North-Holland Publishing Co., Amsterdam (1963).

24. Schultz, E. D. and Holland, A. C., "The Solar Flux Incident at the Top of the Atmospheres of Earth and Neighboring Planets for the Spectral Region 50Å to 3000Å," GCA Tech. Report 62-14-N, Bedford, Mass. (1962).

25. Watanabe, K. (see Nawrocki, P. J. and Papa, R., Atmospheric Processes, Chapter 2, Pergamon Press, 1962).

26. Hall, L. A., Damon, K. R. and Hinteregger, H. E., "Solar Extreme Ultraviolet Photon Flux Measurements in the Upper Atmosphere of August 1961," Space Research III (W. Priester, ed.), p. 745, North-Holland Publishing Co., Amsterdam (1962). Also private communication with H. E. Hinteregger (1962).

27. Detwiler, C. R., Garrett, D. L., Purcell, J. D. and Tousey, R., "The Intensity Distribution in the Ultraviolet Solar Spectrum," Ann. de Geophysique 17, 263 (1961).

28. Johnson, F. S., "The Solar Constant," J. Meteor. 11, 431 (1954).

29. Singer, S. and Chopra, K., Bull. Am. Phys. Soc. 4, 360 (1959).

30. Chopra, K., Zeits. für Physik, 161,445 (1961) and Rev. Mod. Phys. 33, 153 (1961).

31. Meckel, B., Rarefied Gas Dynamics (L. Talbot, ed.) Academic Press, New York, 701-714 (1961).

32. Hall, D., et al., AIAA J. 2, 1032 (1964).

33. Knechtel, E. and Pitts, W., AIAA J. 2, 1148 (1964).

34. Shkarofsky, I., Report No. TM 7-801-011, RCA Laboratories, Montreal, Quebec (1964).

35. Bachynski, M., AIAA J. 2, 1863 (1964).

36. Osborne, F., Shkarofsky, I. and Gore, J., Can. J. Phys. 41, 1747 (1964).

37. Bostick, W., et al., Phys. Fluids 5, 1305 (1962), ibid 6, 1361 (1963), and J. Geo. Res. 68, 5315 (1963).

38. Cladis, J., et al., J. Geo. Res. 69, 2257 (1964).

39. Kawashima, N. and Ishizuka, H., J. Phys. Soc. Japan 18, 736 (1963).

40. Morse, P. M. and Feshbach, H., Methods of Theoretical Physics, McGraw-Hill Book Company, Inc. (1953).

41. Ghosh, S. N. and Sharma, A., Proc. Nat. Acad. Sci. India 33, 635 (1963).

42. McDaniel, E. W., Collision Phenomena in Ionized Gases, John Wiley and Sons, Inc., London (1964).

43. Agdur, B., Ericsson Technics 1, 43 (1960).

44. Hedvall, P., J. Appl. Phys. 33, 2426 (1962).

45. Hasted, J. B., Physics of Atomic Collisions, Butterworth and Co., Washington (1966).

46. Cairns, R. B., Proc. Phys. Soc. 82, 243 (1963).

47. Friedman, H., Physics of the Upper Atmosphere, (J. A. Ratcliffe, ed.), Chapter 4, Academic Press, New York (1960).

48. Mandel'shtam, S. L., et al., Spectrsc. Lab., Lebedev Inst. Phys. AN SSSR, Moscow, A 108-110 (1961).

49. Yefremov, A. I., et al., Artificial Earth Satellites 10 (1961).

50. Pounds, K. A., et al., Proc. Roy. Soc. London (in prep. 1965).

51. Manson, J. E., "Solar X-Rays from 3 to 12 Angstroms as Measured with a Proportional Counter Spectrometer," AFCRL-64-932, Environ. Res. Pap. 68, Bedford (1964).

52. Lindner, J. W., Space Physics, (D. P. LeGalley and A. Rosen, eds.), Chapter 3, Wiley and Sons, New York, 1964).

53. Kreplin, R. W., Ann. Geophys. 17, 151 (1961).

54. Thomas, L., Venables, F. H., and Williams, K. M., Planet. Space Sci. 13, 807 (1965).

55. Nicolet, M., Electron Density Profiles in the Ionosphere and Exosphere, (B. Machlum ed.), p. 116, MacMillan Publishing Co. (1962).

56. Sullivan, J. D., McGrath, J. F., and Thorburn, W. J., AFCRL-64-773, Final Report (Comstock and Wescott, Inc.) Bedford (1964).

57. Kirkpatrick, H. A., J. Quant. Spectrsc. Radiat. Transfer 2, 715 (1962).

58. Rogers, T. H., Cathode Press, p. 8, Fall issue (1951).

59. Private communication with T. H. Rogers, Machlett Laboratories, Inc., Springdale, Conn., and M. Stabler, Westinghouse, Boston Division.

60. Brewster, J. L., Grundhauser, F. J., and Michelsen, A., "Development of Spectral Distribution Single Pulse Determination Techniques for Field Emission Flash X-Ray Systems," Johns Hopkins Univ., Appl. Phys. Lab. CM-1044, Silver Springs, Md. (1964).

61. Bates, D. R. and Seaton, M. J., Mon. Not. Roy. Astron. Soc. 109, 698 (1949).

62. Dalgarno, A. and Parkinson, D., J. Atmos. Terres. Phys. 18, 335 (1960).

63. Dalgarno, A., Henry, R. J. W., and Stewart, A. L., Planet. Space Sci. 12, 235 (1964).

64. Sullivan, J. O. and Holland, A. C., GCA Corp. Tech. Rpt. 64-20-N, Bedford, Mass.

65. Kenty, C., Phys. Rev. 44, 891 (1933).

66. Hinteregger, H. E. and K. Watanabe, J. Opt. Soc. Am. 43, 604 (1952).

67. Walker, W. C., N. Wainfan and G. L. Weissler, J. Appl. Phys. 26, 1366 (1955).

68. Brunet, M., M. Cantin, C. Julliot and J. Vasseur, J. Phys. (France) 24, 53A (1960).

69. Samson, J. A. R. and R. B. Cairns, Rev. Sci. Instr.36, 19 (1965).

70. Lenard, P., Ann d. Phys. 1, 486 (1900); 3, 298 (1900).

71. Hughes, A. L., Proc. Camb. Phil. Soc. 15, 483 (1910).

72. Hughes, A. L. and L. A. DuBridge, Photoelectric Phenomena, McGraw-Hill Book Company, New York (1932).

73. Mohler, F. L., C. Boeckner and W. W. Coblentz, Science 69, 479 (1929); Mohler, F. L., P. D. Foote and R. L. Chenault, Phys. Rev. 27, 37 (1926); Mohler, F. L. and C. Boeckner, J. Res. Nat. Bur. Stand. 3, 303 (1929).

74. Lawrence, E. O. and N. E. Edlefsen, Phys. Rev. 34, 233 (1929); 34, 1056 (1929).

75. Page, T. L., Monthly Notices Roy. Astron. Soc. (London) 99, 385 (1939).

76. Weissler, G. L., "Handbuch der Physik," Vol. XXI, Springer-Verlag, Berlin, p. 304 (1956).

77. Packer, D. M. and C. Lock, J. Opt. Soc. Am. 40, 264 (1950); 41, 699 (1951).

78. Watanabe, K., Phys. Rev. 83, 785 (1951).

79. Tousey, R., F. S. Johnson, J. Richardson and H. Torna, J. Opt. Soc. Am. 41, 696 (1951).

80. Watanabe, K., F. F. Marmo and E. C. Y. Inn, Phys. Rev. 91, 115 (1953).

81. Wainfan, N., W. C. Walker and G. L. Weissler, J. Appl. Phys. 26, 1335 (1957).

82. Sakai, H., J. W. Little and K. Watanabe, J. Chem. Phys. 26, 1335 (1957).

83. Johnson, F. S., K. Watanabe and R. Tousey, J. Opt. Soc. Am. 41, 702 (1951).

84. Watanabe, K. and E. C. Y. Inn, J. Opt. Soc. Am. 43, 32 (1953).

85. Samson, J. A. R., J. Opt. Soc. Am. 54, 6 (1964).

86. Samson, J. A. R., "Absolute Intensity Measurements in the Vacuum Ultraviolet," NASA CR-7 (Office of Technical Services, Washington, 1963).

87. Walker, W. C., J. A. R. Samson and O. P. Rustgi, J. Opt. Soc. Am. 48, 71 (1958).

88. Walker, W. C., O. P. Rustgi and G. L. Weissler, J. Opt. Soc. Am. 49, 471 (1959).

89. Rustgi, O. P., W. C. Walker and G. L. Weissler, J. Opt. Soc. Am. 51, 1357 (1961).

90. Walker, W. C., J. Phys. Chem. Solids 24, 1667 (1963).

91. Robin-Kandare, S., J. Robin and S. Kandare, Compt. rend. 257, 1605 (1963).

92. Axelrod, N. N. and M. P. Givens, Phys. Rev. 120, 1205 (1960).

93. Tomboulian, D. H., D. E. Bedo and W. M. Neupert, J. Phys. Chem. Solids 3, 282 (1957).

94. Tomboulian, D. H. and D. E. Bedo, Rev. Sci. Instr. 26, 747 (1955).

95. Kroger, H. and D. H. Tomboulian, Phys. Rev. 130, 152 (1963).

96. Bohm, D. and D. Pines, Phys. Rev. 82, 625 (1951). For a review of later work, see D. Pines, Rev. Modern Phys. 28, 184 (1956).

97. Samson, J. A. R., and R. B. Cairns, Appl. Opt. 4, 915 (1965).

98. Jacchia, L. G., Research in Space Science, Special Report No. 170, Smithsonian Astrophys. Observatory, Cambridge, Massachusetts (1964).

99. GCA Corporation, Quarterly Progress Report No. 1, Contract No. NAS12-11, August (1965).

100. Accardo, C. A., Gross, H. G., and Weeks, L. H., "A Rocket-Borne 44-60Å Geiger Counter," GCA Corp. Tech. Rpt. 63-14-N, Bedford (1963).

101. Willmore, A. P., Mem. Soc. Roy. Sci. Liege, 5th Ser. Vol 4, 103 (1961).

102. Chubb, T. A., et al., Mem. Soc. Roy. Sci. Liege, 5th Ser. Vol. 4, 228 (1961).

103. Compton, A. H. and Allison, S. K., X-Rays in Theory and Experiment, D. Van Nostrand Co., Princeton (1935).

104. Tomboulian, D., Tech. Rpt. 9, Contract No. Nonr-401(37)NR, No. NR017-625, Cornell Univ., Ithaca (1962).

105. Seya, M., and Namioka, Science of Light 2, 8 (1952).

106. Chubb, T. A. and N. Freedman, Rev. Sci. Instr. 26, 493 (1955) and A. K. Stober, NASA Tech. Note D-1180.

107. Warneck, P., Applied Optics 1, 721 (1962).

108. Johnson, P., J. Opt. Soc. Am. 42, 278 (1952).

109. Hartman, P. L. and Nelson, J. R., J. Opt. Soc. Am. 47, 646 (1957).

110. Moak, C. D., et al., Rev. Sci. Instr. 30, 694 (1959).

111. Hartman, P. L., Private communication with J. A. R. Samson, GCA Corporation (1962).

112. Jansen, C. A. and W. F. Libby, Phys. Rev. 135A, 2147 (1964).

113. Compton, A. H. and S. K. Allison, X-Rays in Theory and Experiment, D. Van Nostrand Co., Princeton, N.J. (1935).

114. Caruso, A. J. and W. M. Neupert, Rev. Sci. Instr. 36, 554 (1965).

115. Spealman, M. L. and W. H. Rodebush, J. Am. Chem. Soc. 57, 1474 (1935).

116. Kaufman, F., Proc. Royal Soc. A. 246, 123 (1958).

117. Herron, J. T. and H. I. Schiff, Can. J. Chem. 36, 1159 (1958).

118. Herzog, R. F. K., Contract NAS5-3251, Final Report, Appendix I and Appendix II (1965), GCA Corporation.

119. Herzog, R. F. K., Private communication.

120. Herzog, R. F. K., Contract NAS5-3251, Final Report (1964), GCA Corporation.